Cyprus University of Technology
Faculty of Engineering and Technology

Doctoral Dissertation

NANOSTRUCTURED AMORPHOUS CARBON-METAL FILMS FOR PROTECTIVE AND SOLID LUBRICANT APPLICATIONS

Marios Constantinou

Limassol, April 2018

CYPRUS UNIVERSITY OF TECHNOLOGY

FACULTY OF ENGINEERING AND TECHNOLOGY

DEPARTMENT OF MECHANICAL ENGINEERING AND MATERIALS SCIENCE AND ENGINEERING

Doctoral Dissertation

NANOSTRUCTURED AMORPHOUS CARBON-METAL FILMS FOR PROTECTIVE AND SOLID LUBRICANT APPLICATIONS

Marios Constantinou

Limassol, April 2018

Approval Form

Doctoral Dissertation

NANOSTRUCTURED AMORPHOUS CARBON-METAL FILMS FOR PROTECTIVE AND SOLID LUBRICANT APPLICATIONS

Presented by

Marios Constantinou

Supervisor: Georgios Constantinides, Assistant Professor

Signature _____

Member of the committee: Tasos Georgiades, Associate Professor

Signature _____

Member of the committee: Angeliki Lekatou, Professor

Signature _____

Cyprus University of Technology

Limassol, April 2018

Copyrights

Copyright © 2018 Marios Constantinou

All rights reserved.

The approval of the dissertation by the Department of Mechanical Engineering and Materials Science and Engineering does not imply necessarily the approval by the Department of the views of the writer.

To my wife Georgia and two children, Antonis and Kyriacos, who are the best things that have ever happened to me.

To my supportive parents whose hard work ethics, love, patience, and tenacity gave me power to continue working on my PhD thesis.

Acknowledgements

The present study was executed at the premises of the Research Unit for Nanostructured Materials Systems (RUNMS), under the Strategic Infrastructure Project NEW INFRASTRUCTURE/STRATE/0308/04 of DESMI 2008 and the PhD course of studies of the Department of Mechanical Engineering and Materials Science and Engineering at Cyprus University of Technology (CUT). The project was co-financed by the European Regional Development Fund, the European Social Fund, the Cohesion Fund and the Research Promotion Foundation of the Republic of Cyprus, all of which are greatly acknowledged.

First of all, I would like to express my sincere thanks and appreciation to my research supervisor Assistant Professor Georgios Constantinides who supported this study during this period; his guidance, inputs and contributions were precious, enlightening and encouraging. I would also like to thank my advisory committee, Professor Pantelis Kelires in the Department of Mechanical Engineering and Materials Science and Engineering at CUT and coordinator of the RUNMS, and Associate Professor Panos Patsalas in the Department of Physics at Aristotle University of Thessaloniki, for their continued support and advice throughout my PhD studies. In addition, I would like to thank the members of my thesis examination committee, Professor Angeliki Lekatou, Department of Materials Science and Engineering at University of Ioannina and Associate Professor Tasos Georgiades, Department of Mechanical Engineering and Materials Science and Engineering at CUT, for their advice and constructive feedback.

I am especially indebted to the Postdoctoral Researcher Dr. Maria Pervolaraki and Professor John Giapintzakis at University of Cyprus who provided the pulsed laser deposited DLC:Ag and DLC:Mo composite films studied within this thesis. The deposition of the films was undertaken at the laboratories of the Department of Mechanical and Manufacturing Engineering at University of Cyprus. I would also like to thank Professor Andreas Anayiotos and Postdoctoral Researcher Dr. Konstantinos Kapnisis, for their scientific inputs in the biomedical field. Those interactions were valuable and we hope to extend our research and potential applications of DLC films in the biomedical sector. Furthermore, my gratitude goes to Professor Constantinos Varotsis in the Department of Environmental Science and Technology at CUT, for Raman Measurements on a-C:H:Me films and Professor Apostolos Avgeropoulos and

Post-doctorate Dimitrios Moschovas from University of Ioannina for Transmission Electron Microscopy measurements on metallic nanoparticles and a-C:H:Me films. Also special thanks to our collaborator Costas Prouskas for measuring DLC:Me films using X-ray Photoelectron Spectroscopy.

Furthermore, the valuable contribution of all the personnel at RUNMS - core team, post-docs, and students - who have been involved in this research is sincerely appreciated.

I would also like to thank the Cyprus State Scholarship Foundation for the three year scholarship which provided me with financial support.

Last, but certainly not least, I deeply appreciate the continuous encouragement of my family and friends.

ABSTRACT

Amorphous carbon exhibits a great diversity in its properties originating from the tunable microstructure that can result in properties that range between the values of graphite and approaching those of diamond. Amorphous carbon with primarily sp^2 hybridization bonds is termed glassy carbon, commonly abbreviated as $a-C$. As the sp^3 content increases the material tends to approach the properties of diamond and consequently $a-C$ with dominant sp^3 microstructures are commonly referred to as diamond like carbon (DLC). Owing to their excellent mechanical, thermal, electrical, optical, chemical and physical properties, DLC films have been the subject of intense research with several existing applications. Their wide applicability ranges from optoelectronic devices like heterojunction devices, thin film transistors and field effect devices to protective coatings for tribological applications like MEMS, air bearing surfaces of read-write magnetic heads for data processing tapes, and hard disk drives.

Incorporating transition metals into $a-C$ or DLC matrices creates a nanocomposite with enhanced physical characteristics (i.e., reduced friction coefficient, enhanced toughness) and additional functionalities (i.e., solar harvesting, bactericidal). This thesis reports on the physical and chemical vapor deposition and systematic characterization of metal-containing hydrogenated and non-hydrogenated DLC thin films with various metal compositions and types: Ag, Ti, and Mo are tested in the atomic percent range of $0-17$ at.%. The deposited $a-C:Me$ and $a-C:H:Me$ films are characterized for their microstructure, crystallinity, surface roughness, residual internal stresses and nanomechanical response. Particular emphasis is placed on the evolution of the nanotribological response of the material with metal content. Transition metals appear to resolve the brittle nature of the highly sp^3 DLC matrix by creating a more ductile and tough nanocomposite while at the same time reduce the residual compressive stresses generated during growth that hinder the development of thicker and stable coatings. Furthermore, these materials exhibit enhanced nanotribological properties that could be exploited for protective coating and/or solid lubricant applications.

Keywords: amorphous carbon thin films; hybrid deposition; nanocomposites; nanoscratch; nanomechanics.

Περίληψη

Ο άμορφος άνθρακας ($a-C$) επιδεικνύει μεγάλο εύρος ιδιοτήτων που προέρχεται από την εκάστοτε συντεθειμένη μικροδομή και δύναται να κατέχει ιδιότητες που κυμαίνονται μεταξύ του γραφίτη και πλησιάζουν εκείνες του διαμαντιού. Ο άμορφος άνθρακας με κυρίως sp^2 υβριδικούς δεσμούς ονομάζεται υαλώδης άνθρακας. Καθώς η περιεκτικότητα των sp^3 υβριδισμών αυξάνει, το υλικό τείνει να πλησιάσει τις ιδιότητες του διαμαντιού και συνεπώς το $a-C$ με κυρίαρχες sp^3 μικροδομές αναφέρεται ως αδαμαντικός άμορφος άνθρακας (DLC). Λόγω των εξαιρετικών μηχανικών, θερμικών, ηλεκτρικών, οπτικών, και χημικών τους ιδιοτήτων, τα λεπτά υμένια DLC αποτελούν αντικείμενο έντονης έρευνας με αρκετές υπάρχουσες εφαρμογές που κυμαίνονται από οπτοηλεκτρονικές συσκευές (ετεροεπαφές υλικών, τρανζίστορ λεπτού υμενίου) και συσκευές επιφανειακών επιδράσεων, σε προστατευτικές επικαλύψεις για τριβολογικές εφαρμογές (μικρο-ηλεκτρο-μηχανικά συστήματα, MEMS, μηχανικά έδρανα κίνησης), και μαγνητικές κεφαλές ανάγνωσης-εγγραφής σε μονάδες σκληρών δίσκων.

Η ενσωμάτωση μεταβατικών μετάλλων σε μήτρες $a-C$ ή DLC δημιουργεί ένα νανοσύνθετο με ενισχυμένα χαρακτηριστικά (δηλ., μειωμένο συντελεστή τριβής, αυξημένη δυσθραυστότητα) και πρόσθετες λειτουργίες (δηλ., αυξημένη ικανότητα συλλογής ηλιακής ενέργειας, υλικό με βακτηριοκτόνο δράση). Η παρούσα διδακτορική εργασία παρουσιάζει τη σύνθεση (με φυσική και χημική εναπόθεση ατμών) και το συστηματικό χαρακτηρισμό λεπτών υμενίων DLC, υδρογονομένων και μη-υδρογονομένων, με διαφορετικές συγκεντρώσεις μετάλλων: άργυρος, τιτάνιο και μολυβδαίνιο σε αναλογίες που κυμάνθηκαν από 0% μέχρι 17%. Τα εναποτιθέμενα $a-C:Me$ και $a-C:H:Me$ υμένια χαρακτηρίστηκαν για τη μικροδομή, την κρυσταλλικότητα, την τραχύτητα, τις παραμένουσες τάσεις και τη νανομηχανική/νανοτριβολογική τους απόκριση. Τα μεταβατικά μέταλλα φαίνεται να μετατρέπουν τη ψαθυρή DLC μήτρα σε πιο όλκιμο και δύσθραυστο υλικό ενώ ταυτόχρονα μειώνουν τις παραμένουσες τάσεις που δημιουργούνται κατά την εναπόθεση και εμποδίζουν την ανάπτυξη παχύτερων και σταθερότερων επιφανειών. Επιπλέον, αυτά τα υλικά εμφανίζουν ενισχυμένες νανοτριβολογικές ιδιότητες που θα μπορούσαν να αξιοποιηθούν για προστατευτικές επιφάνειες ή/και ως στερεά λιπαντικά.

Λέξεις κλειδιά: λεπτά υμένια άμορφου άνθρακα, υβριδική εναπόθεση, νανοσύνθετα, νανοτριβολογία, νανομηχανική.

TABLE OF CONTENTS

LIST OF TABLES

LIST OF FIGURES

LIST OF ABBREVIATIONS

AFM	Atomic force microscopy or microscope
a-C	Amorphous carbon
a-C:Ag	Amorphous carbon silver
a-C:H	Hydrogenated amorphous carbon
a-C:H:Ag	Hydrogenated amorphous carbon silver
a-C:H:Me	Hydrogenated amorphous carbon metal
a-C:H:Ti	Hydrogenated amorphous carbon titanium
a-C:Me	Amorphous carbon metal
a-C:Mo	Amorphous carbon molybdenum
a-C:Ti	Amorphous carbon titanium
Ag	Silver element
AgCu	Silver copper alloy (sterling silver)
Al_2O_3	Aluminum oxide
ALD	Atomic layer deposition
AlMg	Aluminum magnesium alloy
Ar	Argon gas
at.%	Atomic percent
BCC	Body centered cubic crystal structure
CH_4	Methane
COF	Coefficient of friction
CUT	Cyprus university of technology
CVD	Chemical vapor deposition
DAF	Diamond area function
DLC	Diamond-like carbon

DLC:Ag	Diamond-like carbon silver
DLC:Me	Diamond-like carbon metal
DLC:Mo	Diamond-like carbon molybdenum
DLCH	Hydrogenated diamond-like carbon
EBSD	Electron backscattered diffraction
ECWR	Electron cyclotron wave resonance
EDS	Energy dispersive spectroscopy
FCC	Face centered cubic crystal structure
FCVA	Filtered cathodic vacuum arc
FWHM	Full width at half maximum
G	Graphite
GLCH	Hydrogenated graphite-like carbon
HCP	Hexagonal close-packed crystal structure
KrF	Krypton fluoride
MLD	Molecular layer deposition
Mo	Molybdenum element
MoC	Molybdenum carbide
MS	Magnetron sputtering
MSIB	Mass selected ion beam
N_2	Nitrogen gas
Nb	Neobium element
Nd:YAG	Niodymium-doped yttrium aluminum garnet
NPs	Nanoparticles
PBS	Plasma beam source
PECVD	Plasma enhanced vapor deposition

PELD	Pulsed excimer laser deposition
PLCH	Hydrogenated polymer-like carbon
PLD	Pulsed laser deposition
PVD	Physical vapor deposition
RF	Radio frequency
RMS	Root mean square
rpm	Revolution per minute
RUNMS	Research unit for nanostructured materials systems
SEM	Scanning electron microscopy or microscope
Si n+	n-doped silicon
Si_3N_4	Silicon nitride
SS	Stainless steel
t-aC	Tetrahedral amorphous carbon
t-aC:H	Hydrogenated tetrahedral amorphous carbon
Ti	Titanium element
Ti_6Al_4V	Titanium aluminum vanadium alloy
TiAlN	Titanium aluminum nitride alloy
TiC	Titanium carbide
XPS	X-ray photoelectron spectroscopy
XRD	X-ray diffraction
XRR	X-ray reflectivity
ZnO	Zinc oxide

Unit Abbreviations

°C	Degrees Celsius
A	Amber
Å	Angstrom
cm	Centimeter
eV	Electron volt
g	Gram
GPa	Gigapascal
Hz	Hertz
J	Joule
m	Meter
mbar	Millibar
mm	Millimeter
MPa	Megapascal
N	Newton
nm	Nanometer
Pa	Pascal
s	Second
sccm	Standard cubic centimeters per minute (flow unit)
V	Voltage
W	Watt
λ	Wavelength
μm	Micrometer or micron

CHAPTER 1 Introduction

1.1 Research background

Materials science and engineering are two fields of science that are commonly combined for material optimization purposes. Materials scientists investigate the structure-property relationships, while materials engineers utilize this knowledge to design and tailor materials to achieve the required properties. The cooperation of both disciplines offers a powerful tool to grow components/devices with optimum combination of properties and performance characteristics. Nanotechnology, as applied in materials, relates to the ability of materials scientists and engineers to build materials from scratch and then measure their structure-property traits; such artificial materials that have one or more structural entity with dimensions less than $100\ \mathrm{nm}$ in size are referred to as nanomaterials [1,2].

1.2 Research objectives

The theoretical and experimental parts of this PhD thesis deals with nanotechnology synthesis and characterization of amorphous carbon-metal thin films. Consequently, the theoretical part dips in and out to the nanotechnology processes that have been used in this study to design, produce and characterize thin film materials. In general terms, thin films are coatings that are used to change the surface functionalities of bulk materials or substrates without interfering to the bulk properties itself [3,4]. The experimental part explains in detail the design, processing and characterization steps of the synthesized carbon-metal thin films. The envisioned innovations are not limited to the characterization results but also to the use of low temperature deposition technologies, that is a) Pulsed Excimer Laser Deposition (PELD) technology and b) Plasma Enhanced Chemical Vapor Deposition/Physical Vapor Deposition ($\mathrm{PECVD/PVD}$) hybrid technology, for depositing carbon-metal composite films.

The overall aim of this study is to investigate and analyze amorphous carbon metal ($\mathrm{a-C:Me}$) films through a series of theoretical and experimental investigations and moreover explore the potential opportunities of the design concept for mechanical, tribological and other functional applications. The objective of these experiments is to

grow and investigate nanostructured $a-C:Me$ films where the metal is either silver (Ag), titanium (Ti), or molybdenum (Mo); such complex structures with improved mechanical, tribological and physical characteristics are needed to enable high technology applications such as those found niches in bioengineering, microelectronics, optics, robotics, transportation industries, manufacturing, energy production and saving. With a deep knowledge of silver amorphous carbon ($a-C:Ag$) film which could combine strength and ductility, low stress and low density, optical efficiency and low wear rates and low friction coefficient and its design is different from conventional materials [5–7], it may be possible to promote a new generation of multiphase $a-C:Ag$ films with two or more functional applications; among conventional materials, stiff and strong materials are relative dense with high friction coefficients and the increase of its strength drops its ductility. Titanium and/or molybdenum containing amorphous carbon ($a-C$) films are also candidates for advanced applications [8–10] and here are studied as well so to couple the chemical changes (i.e., transformation of sp^3 to sp^2 carbon structure and simultaneous formation of metal carbide compounds) with physical properties and finally film performance. Similar studies have been referred to in the literature [5,8,10], nevertheless an in depth understanding of the structure-property relations for $a-C:Me$ films, in particular their mechanical and tribological response under indentation and scratching is still lacking. The lack of specific structure-property relationships relates to the complex nature of the $a-C$ material systems [11] and the different reactivity of each metal with the surrounding matrix, but also from the large number of thin film growth technologies, that one can use to grow $a-C:Me$ films having different microstructural, geometrical and physical characteristics and the lack of a systematic synthesis and complete characterization of films.

1.3 Research motivation

$a-C$ thin films are materials with either sp^2 and sp^3 carbon - carbon hybrid bonds. The variable properties of such films depend on the bond content, with significant changes occurring as the percentage shifts from sp^2 to sp^3 dominance; high sp^2 percentages promote graphite-like properties whereas high sp^3 percentage favors diamond-like properties. The sp^2 structure is soft and lubricious, whereas the sp^3 structure is hard but brittle (i.e., susceptible to fracture). Hydrogenated or hydrogen-free $a-C$ thin films

with high content of sp^3 carbon - called "Diamond-Like Carbon Films, DLC" [12] - have attracted the interest of researchers chiefly because are low cost, easy to produce and can be tailored to show properties that resemble those of diamond, that is high melting point, high hardness, high stiffness, low friction coefficient, low wear rates, good thermal conductivity, poor electrical conductivity, corrosive and oxidation resistant, and many more [11,13,14]. Although the sp^2 to sp^3 ratio determines the applicability of such films, to build materials for protective and solid lubricant applications, there is a challenge to minimize the sp^2 carbon structure and increase the sp^3 carbon structure which alone provides mechanical rigidity [15]. From a mechanical perspective the problem arises from the brittle nature of the sp^3 structure that contributes to the failure of the film without significant deformation during loading. Several studies have attempted to alleviate this problem by incorporating soft metallic additives within the $a-C$ lattice [5,8,10]. In fact, the idea lies in the formation of a particle reinforced nanostructured nanocomposite film for which the $a-C$ matrix phase is continuous and surrounds the metallic dispersed phase. For such composites, the strengthening mechanism occurs either on an atomic scale or at a continuum level. The former denotes that most of the load is supported by the matrix and the dispersed phase just hinders plastic deformation. On the other hand by continuum mechanics we mean that the whole material mass supports the applied load; for example, consider a hard matrix with soft particulate phase, where, during an applied load the matrix transfers the overload to the dispersed phase and the whole composite deforms in an analogous manner; the dispersed phase may restrain the deformation of the matrix or leave the matrix to strain around it. Of course, the more ductile the dispersed phase is the tougher will be the composite material and more energy will be absorbed before complete fracture. The overall composite response is not only affected by the properties of the constituent phases but also by their relative fractions, the characteristic morphology of the dispersed phase (i.e., size, shape, dispersion and orientation), and the nature of the bond between the particle-matrix microconstituents. Note that for thin films on substrate material the interfacial contact as well as residual stresses are also of great importance. For promoting protective and solid lubricant a-C films, the formation of a dense material, by means of a dense packing of $C-C\ sp^3$ atoms and metal inclusion, must be achieved. For such effective reinforcement the particles must be small, equally dispersed within the amorphous matrix and be unreactive with it. The inertness of

impurity metals is very important so to maintain the properties of the matrix. The mechanical performance of a $-$ C film can be enhanced by means of Ag nanoparticles. Ag is highly soft and ductile. Moreover, is unreactive with carbon atoms and thus does not form adhesive bonds with it. For a $-$ C: Ag films toughness can be promoted by both the hard sp^3 structure and the ductile Ag phase. Another reinforcement technique for strengthening the a $-$ C film is the incorporation of metals that form carbide ceramics, that is, titanium carbide (TiC) and/or molybdenum carbide (MoC) compounds at the boundary areas of a $-$ C matrix and metallic inclusions. Such carbide phases are hard and form well-cemented and sound bonds within the composite structure. Although such carbide phases are not capable of withstanding stresses, it is anticipated that toughness is enhanced because of the ability of such phases to impede plastic deformation and of course of the ability of highly ductile metals to absorb energy during an imposed load upon the structure.

The lack of a concentrated study for the deep understanding of the chemical and mechanical relationship/performance of a $-$ C: Me, and moreover the formation of a dense packing material with enhanced mechanical, tribological and other functional applications is the motivation of this study. We aim to promote a new generation of a $-$ C: Me films with better combination of properties and performance. Two deposition technologies are employed for the growth of multiphase a $-$ C: Me films, (a) a hybrid deposition technology, PECVD/PVD - for Plasma Enhanced Chemical Vapor Deposition/Physical Vapor Deposition - and, (b) a single deposition technology, PELD for Pulse Excimer Laser Deposition. The motivation of using the above deposition systems is associated with the fashion of better property combinations within a single material not able to achieve using conventional deposition techniques [16–20]. Low temperature and high energetic plasma processes, insensitive to abruptly changes during deposition are needed to be comprehended so to produce more robust, with better quality and lower cost coatings. Such technologies have the ability to produce nanocomposite and multilayer film materials for modern material needs, for example, to exploit the present energy resources (i.e., by converting solar energy into thermal power), for reduction of weight and energy losses in transportation vehicles (i.e., new tough coatings with low friction coefficient and density), to reduce wear and friction on cutting tools (i.e., materials with low friction coefficient, high fracture resistance and

refractory under high temperature operations), to stretch the use of classic fluid lubricants (i.e., growth of solid lubricants which are also environmentally friendly). To conclude, according to the principle of the combined action, we aim to promote a new generation of materials with two or more applications. A research outline is followed.

1.4 Thesis outline

This thesis consists of 8 chapters. The aim, objective and key points of this study are addressed in Chapter 1. Chapter 2 reviews fundamentals about amorphous carbon films as well as the motivation to use and improve the mechanical and tribological properties of amorphous carbon through metal doping. Chapter 3 is all about nanomechanical characterization. Chapter 4 discusses experimental results on the synthesis and characterization of DLC: Ag films prepared by PELD technology of sectored target. Similar synthesis and characterization results are presented in Chapter 5 for PELD DLC: Mo films of sectored target. Moreover, the technical characteristics for the growth of hydrogenated Ag and Ti amorphous carbon films using a novel hybrid PECVD/PVD deposition technology as well as characterization results are shown in Chapters 6. The application of a − C: H film on various metallic substrates and metallic stents is explored in Chapter 7. A summary of the main outcomes as well as suggestions for future directions are included in the final chapter of this thesis, Chapter 8.

CHAPTER 2 Fundamentals of amorphous carbon films

2.1 Introductory remarks

This thesis deals with the development, understanding and optimization of amorphous carbon-metal nanocomposite films. Before proceeding with the synthesis and characterization of a-C:Me films, a short introduction on amorphous carbon, the host matrix in all nanocomposite films that will be discussed later on, is due. This is the focus of this Chapter.

2.2 Bonding characteristics

Amorphous carbon ($a-C$) or hydrogenated amorphous carbon ($a-C:H$) films are by their very nature non equilibrium amorphous structures [11]. What characterizes the amorphous structure of such materials is the combination of sp^2 and sp^3 hybridization states of carbon (see Fig. 2.1), with sp^3 percentage being the key property especially for diamond-like optical, electrical and mechanical properties when it is found in higher concentration compared to sp^2 hybridization state [21]. Very small amounts of sp^1 bonds are likely to be formed within amorphous carbon structures using some deposition processes but this is limited in the range of 1 to 2 $at.\%$ [11]. The Diamond-like carbon (DLC) designation is stated only for films with high sp^3 percentage [11].

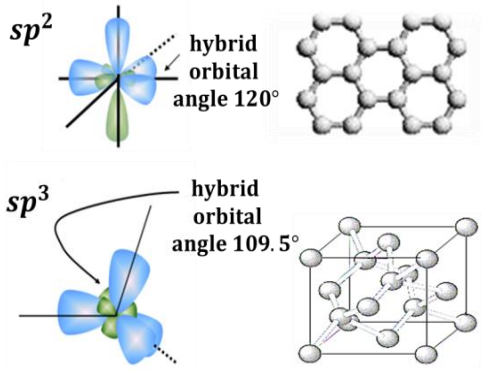

Figure 2.1 Two of the possible configurations of carbon atoms within amorphous carbon film that are sp^2 and sp^3. The crystalline sp^2 bonds may form a lamellar structure in the 2 dimensional view. The crystalline sp^3 bonds are placed in a cubic structure in the 3 dimensional view. Note that both sp^2 and sp^3 structures are found to be disordered in amorphous carbon network.

Amorphous carbon films are a family of materials their composition of which depends on the selection of the growth technique, the type of the precursor material used during their growth, and the presence (or not) of secondary phase elements. According to the phase diagram presented in Figure 2.2, amorphous carbon matrices can be classified in five groups relating to their sp^3, sp^2, and H percentages. Graphite-like $a-C:H$ (GLCH) with high sp^2 disordered content, either organized in rings or chains, have been prepared by pyrolysis of hydrocarbon polymers or evaporation methods or PECVD using bias voltages [22–27]. Such films have hydrogen content up to 20%, high $sp^2\%$ and are mechanically quite soft. Hydrogen free tetrahedral $a-C$ films ($t-aC$) with high $C-C\ sp^3\%$, (≥ 70 %), have been prepared by Pulsed Laser Deposition (PLD), Filtered Cathodic Vacuum Arc (FCVA) and Mass Selected Ion Beam (MSIB) processes [14,28–30]. $t-aC$ films are also called diamond like carbon (DLC) and they are dense ($\geq 2.2\ g/cm^3$), mechanically hard (≥ 10 GPa), with friction coefficients similar to diamond, the value of which varies from 0.4 to 0.7 depending on the environment tested [31]. Another one class are the $a-C:H$ with hydrogen content between $40-60\%$. Although such films contain high $sp^3\%$ most of this percentage is hydrogen ended resulting to films with low hardness, low density, low residual stress and low friction coefficient values reaching that of graphite at dry atmosphere to ≈ 0.001 and increases as humidity increases to $\approx\ 0.2$. The aforementioned films are also known as polymer-like $a-C:H$ (PLCH) and can be grown by PECVD [26,27]. Decreasing the hydrogen content for $a-C:H$ among $20-40\%$, their $C-C\ sp^3\%$ increases against $C-H$ bonds, giving more mechanical rigidity and higher friction coefficients to this category of films also called diamond-like (DLCH) films. Such films can also be grown using the PECVD technique [32]. The final category of amorphous carbon films is that of $t-aC:H$ films. The characteristic of such films is its ability to grow having high $C-C\ sp3\ \%$ maintaining their hydrogen content low to $20-25\%$. Such films are called DLCH and its growth is preferred against other types of $a-C:H$ because they can reach similar properties like $t-aC$ films [33]. Among the techniques that allow their production are Electron Cyclotron Wave Resonance (ECWR) source or Plasma Beam Source (PBS) with radio frequency (RF) power [34,35].

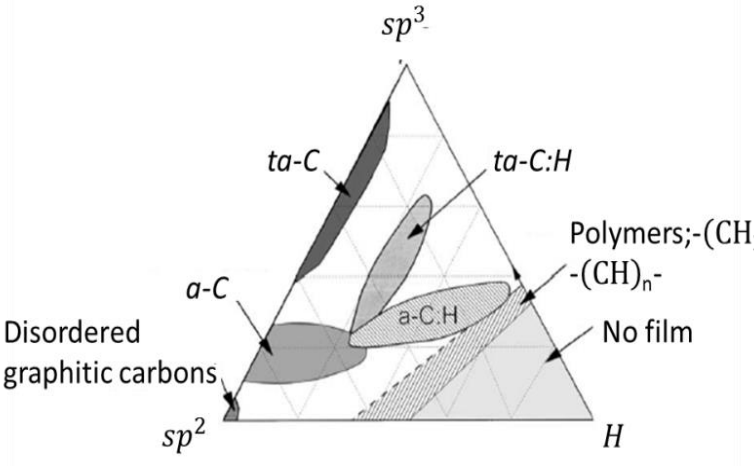

Figure 2.2 Ternary phase diagram of possible a-C compositions as proposed in the review paper of Robertson in 2002 [11].

2.3 Applications of amorphous carbon films

In general a – C films have been designed to be used in optics, micro-electro-mechanical systems, consumer goods, manufacturing and automotive industries, textile industry, computer engineering and biomedical field. In fact, a – C films have already been used on razor blades to increase their lubricity and performance. Moreover, they have been used as protective coatings on micro devices to reduce wear and friction forces. More recently, they have found niche applications in the manufacturing industry for decreasing scratching of material during drawing, molding and rolling operations and hence to reduce the possibility of getting worn and scrap materials. Many engine components have been coated with a – C film to increase lubricity on sliding contacts through the drop of friction coefficient that is offered by a – C material. Even within the textile industry, a – C can decrease the temperature of needles during sewing and the breaking cohesion of thread. More information of above discussed and more applications can be consulted from References [36–43]. Some of the applications of a – C films are schematically shown in Figure 2.3.

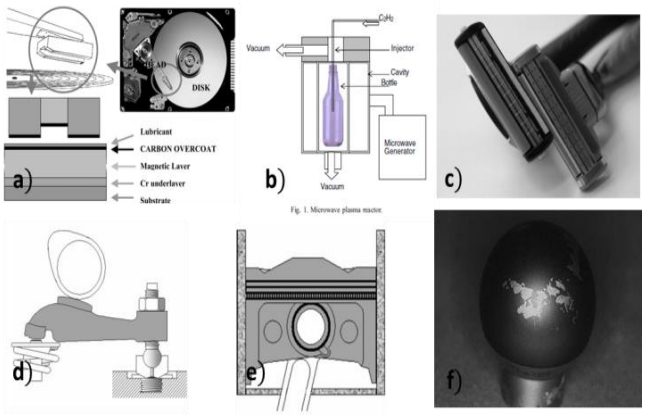

Figure 2.3 Industrial applications of a-C films on a) magnetic disc, b) PET bottle, c) razor blade, d) rocket arm, e) piston, and, f) polyethylene arthroplasty head.

2.4 Properties and characteristics

All of the applications mentioned above obviously have a common direction towards economic efficiency and sustainability development including material efficiency issues. These demands can be achieved because $a-C$ is a material that is low cost, can be easily produced and exhibit both low friction coefficient (i.e., in the range of $0.001-0.7$), high hardness (i.e., higher than $10\,GPa$), resilience, good thermal conductivity, low thermal expansion, low wear rates, optical transparency and chemical inertness, actually an impressive amalgam of properties within a single material [11]. The success of $a-C$ material as solid lubricant in tribological applications is strongly inherent not only to their good mechanical properties, low friction coefficient and smooth surface roughness but also to the well-adherence on substrate materials [31] - example of such substrates are carbide forming substrates such as silicon and titanium. However, as is not very tough, appropriate design (here we mainly focus to design particle reinforced composite for which the matrix is either $a-C$ or $a-C:H$ material and the dispersion phase is one of the following metals, $Me = Ag, Ti, Mo$) can significantly improve fracture toughness of this material and at the same time reduces residual stresses that limit the fabrication of thicker films [44–48]. The increase of fracture toughness could not only drive to the increase of ductile nature of the material, but also would be beneficial for lowering the friction forces developed between two surfaces for long lasting sliding. To extend more on this reference, generally, friction force is affected by three main parameters [31]. These are a) abrasion, b) adhesion and,

c) shearing coefficients. Abrasion coefficient increases with the convenience a material is scratched and eventually fractures and forms debris. The adhesion coefficient is mainly controlled by chemical interactions/forces occurred between the two sliding surfaces and results to the formation of material that may obstruct shearing between the two sliding surfaces increasing friction force; adhesion coefficient and the formation of adhesive material is affected from the mechanical properties and the roughness of the surface as well. Last, the shearing coefficient results when debris, or contamination layer, or tribofilm produced by tribochemistry, adhere on the sliding asperity and thus influence friction force. All of the above-mentioned parameters are indirectly influenced by the mechanical properties of the material, the degrading of which increase abrasion, adhesion and shearing coefficients that lead to an increase in friction force. Other parameters beyond material's properties that are crucial for the control of friction force in tribology are environmental effects including the rise of both temperature and humidity.

The contribution of these parameters to the frictional properties of $a-C$ films is discussed. Generally as $a-C$ films (hydrogenated or not) are hard and well adhered on substrate materials can provide both abrasion and adhesion resistant under sliding asperities; thus the formation of adhesive material is somewhat moderated. Moreover, as chemical interactions (i.e., covalent, metallic, ionic or weak bonding) are inevitable between the two sliding surfaces, this gives rise to the increase of adhesion forces and the creation of adhesive materials that increase friction force. Such adhesive materials include debris, or contamination layers. Nevertheless the primary mechanism that control the low friction coefficient ranges for the family of $a-C$ films is based on the formation of a transfer/carbonaceous layer on both $a-C$ top layers and asperity surfaces, which increases the shearing coefficient and thus decreases friction force and sliding energy [49–51]. The formation of a transfer layer is driven by the increase of localize temperature during dynamic sliding regime that tends $a-C$ to a graphitic stable state [52]. Indeed the friction coefficient of $a-C$ films were found to exhibit low values, ranging from 0.001 for highly hydrogen content $a-C:H$ to 0.7 for $ta-C$ films, a variation that depends on the percent of humidity for each testing environment [31].

Various previous works dealt with the growth and characterization of composite/engineered hybrid $a-C:Me$ films. The ability to overcome the limitation of

existing $a-C$ films by combining the best properties of two or more individual constituents on one material is now being possible; recently, new deposition technologies and hybrid processes have been used for depositing nanocomposite and multilayer films with optimum property characteristics and in only one deposition process. For example deposition technologies combining, PVD-magnetron sputtering with PECVD [53,54] or ALD (Atomic Layer Deposition) with MLD (Molecular Layer Deposition) techniques [55] have already been reported in the literature. During these processes, films which can be used in more than one application may be prepared. Examples include $a-C:Ag$ films with good scratch resistance and low compressive stress [47,54] that may be used on optical devices for increasing light absorption and thermal efficiency of solar cells [56], $a-C:Ti$ films which is a corrosion-resistant material with application on bioimplants [57] and self-cleaning coatings [58], $ta-C/Si_3N_4$ which is a hard, optical film material with piezoelectric response [59], and many more. Of course an in-depth materials optimization study that originates from the atomic level and ends at the level of engineering applications is a challenging task that requires materials science and engineering knowledge and interdisciplinary research for understanding and optimizing the synthesis-structure-property relationship of materials.

2.5 Chapter summary

This chapter introduced the fundamental aspects relevant to the synthesis, bonding characteristics, properties and existing industrial applications of amorphous carbon films. The high residual stresses trapped during the deposition within the amorphous carbon matrices, that could result in residual compressive stresses on the order of GPa, hinders the development of thicker films and subsequently further practical exploitation as it results in a material with reduced adhesive strength under contact loading or scratch. This could be resolved by introducing metal elements within the brittle amorphous carbon matrix thus empowering the more efficient material use in applications that demand durability and ductile behavior while in service. A major challenge of this study is the development of a novel hybrid PECVD/PVD system that was recently installed within the premises of the Research Unit For Nanostructured Materials Systems to produce $a-C:H:Me$ composite materials with controlled structural bonding and metal composition. The potential of PECVD/PVD system to

produce $a-C:H:Me$ films that have very low friction coefficient under dry atmosphere; due to the presence of hydrogen [31], was used. Of course, the final aim was to explore the potential opportunities of composite materials for new application.

Various other methods were used for the full characterization of the produced materials, such as X-ray reflectivity, X-ray photoelectron spectroscopy, X-ray diffraction, transmission electron microscopy, energy dispersive spectroscopy and Raman spectroscopy, for measuring density, thickness, chemical characteristics, concentration specifications, and crystallinity. Moreover scanning electron microscopy was used for observing the failure modes of materials after scratching. The experimental details of all the above-mentioned techniques will be detailed within each chapter of their use; the underlying principles of operation of each techniques can be consulted through bibliographical records [32,60–67]. In the following section we will explain in more detail the nanomechanical characterization of films and how can be achieved through an instrumented nanoindenter. The principles of atomic force microscopy and its use towards quantification of nanoparticles that were used in a-C:H:Me films (Chapter 6), is presented in Appendix A.

CHAPTER 3 Nanomechanical characterization

3.1 Introductory remarks

Mechanical properties are magnitudes that reflect the response of materials under imposed load. In general, materials scientists and engineers are increasingly interested on the mechanical properties of materials or regulating the mechanical response especially when materials are intended to be used in structures as integral parts of their load-bearing capacity. The knowledge of mechanical properties of materials is of great importance as may prevent undesirable failure of materials that may lead to economic losses or even worse to human losses. For an engineer to be able to alter the mechanical properties of materials must be familiar with processing-structural characteristics and have a deep understanding of the mechanisms which affect mechanical properties. This Chapter starts by discussing key mechanical properties and then all about nanoindentation technique and how the latter can be used to characterize the mechanical properties/performance of thin film materials. With regard to nanoindentation technique, we focus on nanoindentation instrumentation design, types of experiments, calibration, execution and analysis of nanoindentation data. We also note error in nanoindentation tests the wrong evaluation of which may give wrong mechanical results.

3.2 Key mechanical properties

Five of the key mechanical properties are: stiffness, strength, ductility, hardness and toughness. All of these properties would be a formidable combination if existed enhanced on a single material; nevertheless this is not common. In fact, high strength and ductility rarely coexist. Usually materials with high strength show limited ductility and thereby low displacement deformation till fracture under applied load. Here we will describe what each mechanical property represents. Starting by stiffness is a property that shows the resistance of a material to elastic deformation, measured in $\mathrm{N/m}$. The value of stiffness is tightly associated with modulus of elasticity or Young's modulus, as Young's modulus is proportional to the slope of the force-separation curve of a material at equilibrium state. On an atomic scale, stiffness is the force needed for separating two

bonded atoms within a material structure. Consequently, the stiffer the material the higher is the magnitude of modulus of elasticity. Young's modulus is measured in MPa. The stress which is needed to plastically deform a material, it is noted as yield strength. Yield strength value - also measured in MPa - shows how strong is a material and the stress level needed to initiate plastic deformations within a material. Ductility is another mechanical property that displays the degree a material is plastically deformed till fracture. In a uniaxial stress-strain test, the ductility of a material may be expressed quantitative as the percent elongation to fracture, percent reduction of area to fracture or by defining the strain value at the maximum load for fracture, see for example Figure 3.1. A material that gives no large amounts of plastic deformation is termed brittle, an example of which demonstrated in Figure 3.1. Ductility and brittleness are relative terms in the sense that the manner which a material fails - either ductile or brittle - is strongly affected on the temperature, stress state, strain rate and material's microstructure. Moreover toughness (or fracture toughness) is a property that shows the resistance of a material to brittle fracture. It is a property indicative of the material's ability to absorb energy when it is plastically deformed without fracture, even when defects such as foreign inclusion, cracks, pores, or other micro-concentrated defects are present within a material. Usually a tough material exhibits both strength and ductility - hence is strong and capable to carry out large amounts of deformation. Here, it is worth noting that both fracture toughness, strength and ductility are properties sensitive to the microstructure of the material as well as to the temperature, any prior deformation and the strain rate and stress state that a material is subjected. On the other hand although elastic modulus remains unaffected to any change of the above practice, it is strongly decreased by increasing temperature. Fracture toughness can be calculated using the fundamentals of fracture mechanics. Such an approach is quantitative in nature, the specific value of fracture toughness is defined as $K_c = Y\sigma_c\sqrt{\pi\alpha}$ with $MPa\sqrt{m}$ units nevertheless is not an easy task as it implies the experimental estimation of the critical stress for crack propagation, σ_c, crack half-length of the internal crack, a, and definition of Y parameter. For low strain rate uniaxial stress-strain experiments toughness is calculated by integrating the area under the stress-strain curve. Such a test gives also specific fracture toughness values measured in J/m^3. For high strain rate conditions this can be done by performing an impact test and calculating the impact energy, in joule (J), absorbed by the material; this type of testing is qualitative in nature as the extracted

impact energy is strongly influenced by the specimen configuration (i.e., how is supported during testing), as well as by its geometries (i.e., size, shape and preexisting crack size and orientation). Nevertheless, the results from impact tests are often used for making comparisons. Hardness shows the resistance of a material to localized plastic deformation (e.g., a dent or a scratch). It can be calculated by the Johannes Brinell's relationship which is defined as the ratio of the applied load over the area of the resultant imprint on the surface of a material. Hard materials usually exhibit high yield strength values and are limited in ductility by means that are susceptible to fracture and cannot sustain large amounts of deformation.

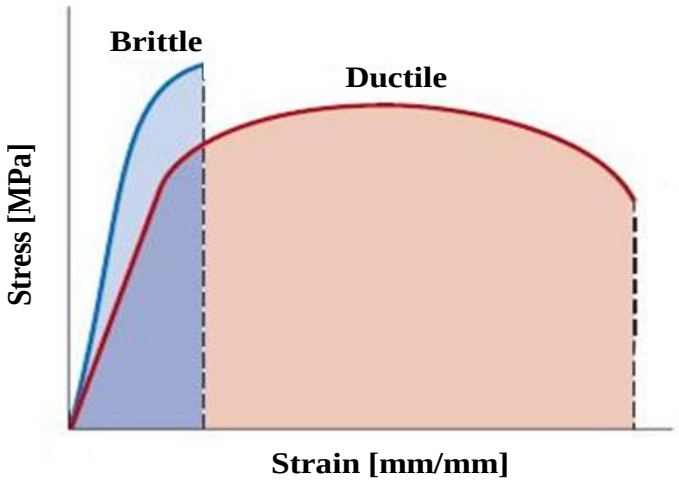

Figure 3.1 Stress-strain behavior of a brittle and a ductile material imposed under uniaxial load to fracture. The colored areas show both elastic and plastic deformations of materials with the larger colored area to display the more ductile material. Image adopted from, http://2.bp.blogspot.com/-XZLSJar7hqA/Tj_ELm_Nb_I/AAAAAAAAABk/S0iIEAw-S1c/s1600/Graph.jpg.

Furthermore, to better understand what each property represents, it is easy to have in mind the mechanical properties of the three main types of material, which are metals, ceramics and polymers. Metals are stiff (with high Young's modulus), strong (with high Yield strengths), ductile (capable to sustain large amounts of deformation before fracture) and tough (show both strength and ductility). Ceramics exhibit also large stiffness and strength values as metals do but are hard (not ductile, susceptible to fracture and brittle). Consequently, ceramics are not tough materials. On the other hand, polymers are very ductile materials and easily pliable and therefore not stiff and strong.

Composite is another category of materials composed by the combination of two or more concentrations of materials. The final properties of such materials are a

combination of the properties of the individual components, phase amounts, the geometries of the phases and interfacial bonding. The designed scope of these materials is to get materials with properties that cannot exist by individual components. Here, in this study, we mainly concerted our effort to improve the ductility - and hence fracture toughness - of hard a − C film by incorporating soft metallic impurities within its structure. In the following sections the nanoindentation technique is presented and the methodology for mechanical property extraction of thin film through nanoindentation experiments is described.

3.3 Nanoindentation

Nanoindentation is an ideal tool to assess the mechanical properties of materials at small scales [68]. In nanoindentation a hard probe penetrates the investigating material at a specified loading rate. During a single load-unload penetration test both load and displacement of the indenter within the material are measured and provided the indenter geometry is known, one can readily calculate its hardness and modulus of elasticity [69].

An instrumented nanoindenter can be used to measure the mechanical properties/performance of any kind of material, whether hard or soft, at any environment (in vacuum, gas, or liquid) and at any temperature (low or high). Indicative examples of the capabilities of the technique include the measurement of hardness, Young's modulus and impact resistance of hard titanium aluminum nitride (TiAlN) films at temperatures up to 400℃ [70]. Soft biological tissues can be measured as well to extract their viscoelastoplastic properties being fully emerged in liquids using liquid cell nanoindentation device [71]. Moreover, hard ceramic nitrides and a − C films with high hardness can be scratched to evaluate scratch strength, friction coefficient, cracking and other failure characteristics [72,73]. More applications of nanoindentation are also summarized in a recent review of Oliver and Pharr [74].

The quality and accuracy of nanoindentation data depend on various factors that may lead to errors and must be considered during experiment so to get as accurate and precise results as possible. Nanoindentation data is strongly influenced from the properties of the instrument. This has demonstrated the need for regular instrument calibrations the most common of which are load calibration, depth calibration, thermal

drift correction and instrument compliance correction. These essential calibrations are described in detail within the following section. Another source of error in nanoindentation arises from the properties of material itself; it is always recommended to know more about the investigated material's microstructure, for example its homogeneity, inelastic response, brittleness, internal features, porosity, surface roughness, etc. Such information could be useful for better scheduling an experiment prior to the test. For example think of nanoindentation measurements on soft polymeric materials. If the user does not consider its viscoelastoplastic flow (commonly referred to as creep), the unloading curve will move to the right and errors in the calculation of contact stiffness might lead to wrong or even erroneous values for hardness and elastic modulus [75]. Soft materials also tend to pile up around the indenter during indentation and this effect should be accounted for so to get correct mechanical measures [76,77]. For thin films on substrates it is also important to consider possible cracks on the film or the substrate or delamination of the film during testing. Such failure characteristics can give wrong values as contact compliance of the sample will increase significantly and discontinuities in loading portion would be observed [78] . Moreover, inhomogeneity of sample composition and/ or film thickness give rise to scattering of nanoindentation data and large deviation from the actual value may be measured. The effect of scattering in nanoindentation data - for inhomogeneous material compositions - can be significantly decreased if the user arrange for an increase number of nanoindentation measurements (i.e., grid nanoindentation technique). The use of nanoindentation grid technique in heterogeneous samples (composites) has been tested by Constantinides et al, leaded to the conclusion that the corresponding measured value is a mixture/average of each component phase [79] and reliable results can be derived if the user perform large penetrations on a grid pattern indentation experiment [80].

The use of unknown tip geometries to measure the sample's properties can also add uncertainty into the extraction of mechanical values. Two types of indenters are usually used in nanoprobing. These are spherical or sharp indenters (i.e., conical or Berkovich indenters) [68]. In reality, neither spherical nor sharp indenters have an ideal initial apical shape something that can significantly affect nanoindentation data. The most commonly used method to calibrate the area function of any type of indenter is the method proposed by Oliver and Pharr in 1992 [69]. The procedure ensues progressive

penetrations into a material with known Young's modulus and calculation of the material contact stiffnesses for each penetration cycle, values that are later used for calculating the contact depths using Eq. (3.3). The contact area for each contact depth is calculated through Eq. (3.2). The result is a plot of contact area as function of contact depth where the relationship of both variables is given by a fitting polynomial to the measured values. An example from the calibration of the Berkovich indenter used for evaluating the mechanical properties of thin film materials in this study is shown in Figure 3.2.

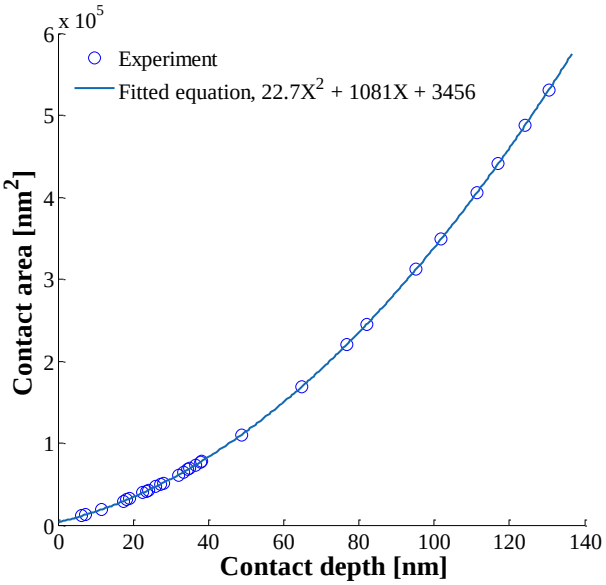

Figure 3.2 Relationship between diamond contact area and contact depth. The fitting polynomial (here a second order polynomial is used) estimates the area of the indenter for depth up to 130.4 nm.

Errors in nanoindentation may also arise from the selection of the several model functions and constant parameters that are used for assessing nanoindentation hardness and elastic modulus values. Generally hardness and elastic modulus values are calculated from the following relations:

$$H = \frac{F_{max}}{A} \tag{3.1}$$

$$E_r = \frac{S \times \sqrt{\Pi}}{2 \times \sqrt{A}} \tag{3.2}$$

where F_{max} is the maximum load at maximum penetration depth, E_r the reduced elastic modulus (depended on both specimen and indenter properties), S is the contact stiffness,

and A is the contact area, a function of the contact depth (see also Figure 3.2) that can be calculated from:

$$h_c = \beta h_{max} - \varepsilon \frac{F_{max}}{S} \tag{3.3}$$

where ε and β are constants that take different values when soft or hard materials are tested. For hard materials ε equals 0.75 for either spherical or sharp indenter, while β is 1.0 for spherical indenter and β is 1.05 for Berkovich indenter. For soft materials that tend to pile up around the indenter during penetration ε and β are 1.0 and 1.2 respectively [77]. The contact stiffness is usually calculated by the slope of the unloading portion of the load-displacement curve by differentiating a fitting equation on the unloading portion; commonly a power law relationship (Eq. (3.4)) is used as recommended by Oliver and Pharr [81], instead of a linear function that was initially suggested.

$$F = a(h - h_f)^m \tag{3.4}$$

Therefore, the correct selection of the constants and model functions play a significant rule.

For nanoindentation on thin film systems, which is actually a thin film on a substrate material things are rather different; measured properties are found to be influenced from the substrate material. Such characterization therefore requires continuous measurement of the requested property at various depths and then fitting the relative data by a suitable model, the interception of which with the vertical axis gives the relative property unaffected from substrate contribution. An accurate determination of hardness and elastic modulus values depend on the selection of the model function. Various theoretical and experimental models were proposed in the literature for evaluating hardness and elastic modulus of thin film components [82–85], the selection of which depends not only on the type of the measured thin film system (i.e. soft film on hard substrate, soft film on soft substrate, hard film on hard substrate and hard film on soft substrate) but also on the conditions for which the model is valid (i.e., applied load, film thickness, type of indenter, etc.).

Nanoindentation can be used for much more than simply measuring the hardness and elastic modulus of materials. Therefore, other property values are tractable using a nanoindenter, for example, the dissipated elastic or absorbed plastic energy during nanoindentation test, the stress for the beginning of yielding in a stress-strain nanoindentation curve, the load for full fracture and other adhesion properties during scratching thin film system [86,87]. Various publications are also quoted to the determination of fracture toughness though simple nanoindentation, scratch or impact technique [88–92].

The NanoTest platform III system located at the Mechanics and Materials Testing laboratory at CUT offers a range of nanomechanical experiments and the ability to the users to get a comprehensive view concerning the mechanical properties of materials. Materials that can be tested include all types of materials either hard or soft and even bulk or thin films. The specifications of the NanoTest platform III are illustrated in Table 3.1. In the following paragraphs, the nanoindentation NanoTest platform III of Micro Materials ltd is presented. The various techniques available with the nanoindentation platform are also given. The last section contains information for calibrating the nanoindentation platform, for executing nanoindentation experiments and for analyzing nanoindentation data.

Table 3.1 Specification of the NanoTest nanoindenter platform III located at the Mechanics and Materials Testing laboratory at Cyprus University of Technology.

NanoTest specifications	Resolution
Maximum load	500 mN
Maximum displacement	10 μm
Displacement noise	≈2 nm
Load resolution	0.1 mN
Displacement resolution	0.1 nm
Instrument compliance	0.361 nm/mN
Stepper motor resolution in X,Y,Z directions	1 μm

3.4 Nanoindentation instrumentation

Figure 3.3 shows the nanoindentation unit available at Mechanics and Testing of Materials laboratory at CUT. The instrument consists of the main nanoindentation platform, electronic controllers and the computer with two screens. The basic parts of

the nanoindentation platform are two, the stepper motors and the electromagnetic driver with the pendulum and displacement sensor. The stepper motors allow coarse movements of the sample in the three dimensional coordinate system and thus positioning of the sample at a specific place in the case one desires to perform test on a specific area on the sample surface. The controlled movement of the stepper motors also allows for performing grid nanoindentation measurements with sizes ranging to micron dimensions. The experimental setup requires the placement of the indenter on the indenter holder and glue of the sample on the sample holder (see Fig. 3.3(b). Further, after the sample is placed in a suitable position using the stepper motors the precise loading and unloading of the intender is performed using the electromagnetic driver found at the upper part of the pendulum. The displacement sensor is measuring the precise movement of the indenter and both load and displacement magnitudes can be recorded (e.g., see the example load-displacement graph on fused silica as shown in Fig. 3.4).

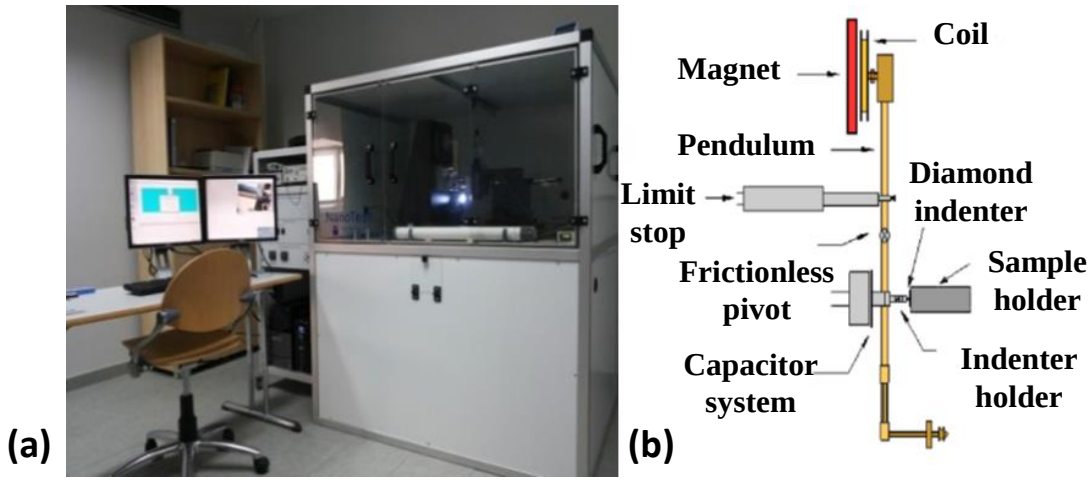

Figure 3.3 (a) Photograph of the nanoindentation instrumentation of Micro Materials limited, UK. (b) detailed scheme of the nanoindentation pendulum.

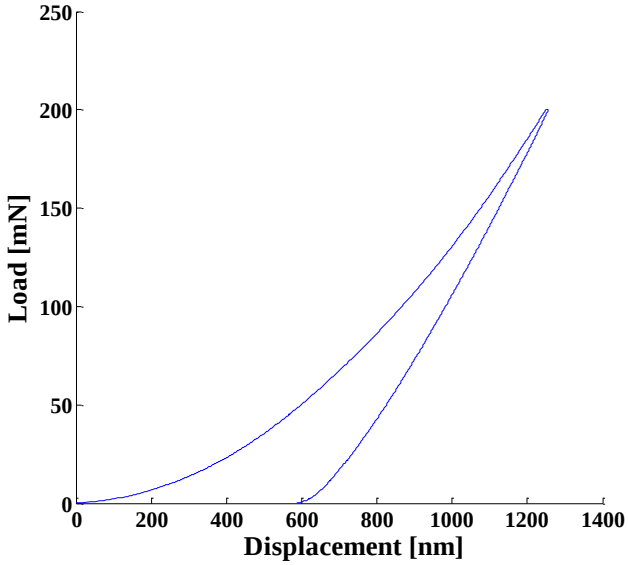

Figure 3.4 Load-displacement curve of fused silica sample.

3.5 Nanoindentation techniques

Different types of nanoindentation experiments can be performed using the nanoindentation platform. Additional to the well-known nanoindentation experiment (simple load-unload test), nanoindentation instrument is equipped with components for performing scratch, impact, fatigue and fretting on materials [93]. In the following paragraphs only nanoindentation and scratch techniques are presented as are two of the techniques that have been extensively used to complete the studies presented in Chapters 4 to 7.

3.5.1 Nanoindentation mode

Measuring the load-displacement curve (see Fig. 3.4) during a single loading-unloading penetration within a material is the simplest and quickest way to get basic information about a material, that is to say, for calculating mechanical properties of materials (i.e., hardness and Young's modulus), for comparing a series of materials (with respect to its penetration depth for a given load), and, moreover, to get irreversible phenomena if they exist (i.e., cracking during loading, phase transformation during unloading or delamination of the coating component during loading). The increase of the number of tests (creation of a grid pattern) gives statistically better results.

Load partial unload test is also another one mode of nanoindentation technique. This mode is well applicable on coated components as allows the user during a single test to measure relevant material properties as a function of the penetration depth. The need for such experiment lies in the nature of coated components; substrate material influences thin film material properties. For soft coating on hard substrate the substrate effect can be neglected by keeping the penetration depth at the 10% of the material thickness [94,95]. Nevertheless, for hard coatings on soft substrates things are rather different as material properties observe to be underestimated, especially for elastic modulus which observes to rapidly decrease even at very low loads. An example of load-partial unloads experiment on hard DLC film on silicon substrate can be seen in Figure 3.5. The way of analysis of nanoindentation tests is presented in the following section.

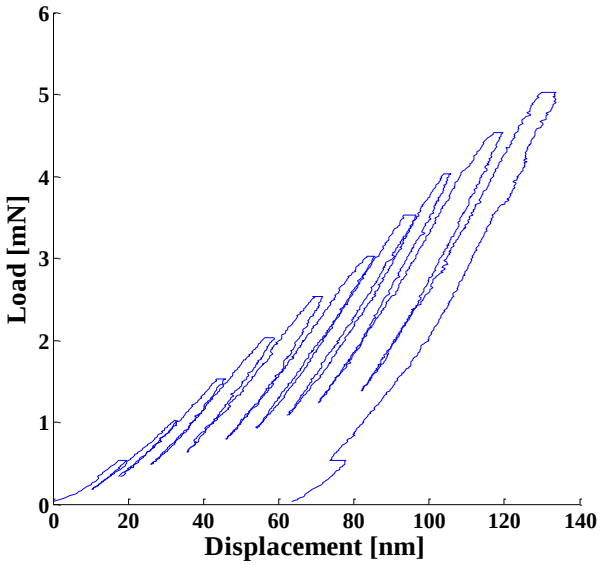

Figure 3.5 Course of ten load-partial unload penetrations on hard diamond-like carbon film grown on silicon substrate.

3.5.2 Nanoscratch mode

Scratching a material is easy to perform using a nanoindentation platform. An external component needs to be screwed on the nanoindentation platform for measuring friction forces during the propagation of scratch test. A sketch of the friction probe is illustrated in Figure 3.6. As can be seen, the indenter is placed on the friction probe holder which is located ahead of the two metallic wires which act as friction force sensors. The bending of the wires can translate into the frictional force which is recorded for all applied normal loads. Some key properties that could be measured by scratching thin

film components are a) the load showing departure from elastic to plastic deformation, b) the limit load for initiating cracking, and, c) the load for complete film failure and debonding from the substrate material. Furthermore, friction coefficient can be calculated by simply dividing frictional force over normal force for the whole scan duration. Examples of scratch tests and accumulated results are presented in Chapters 4 to 7.

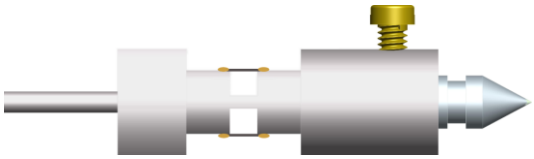

Figure 3.6 Sketch of friction probe.

3.6 Calibration, execution and analysis of nanoindentation data

As mention above the quality of nanoindentation data is strongly dependent on the accuracy of the load-displacement measurements. This introduces the need for nanoindentation device calibration. The essential calibrations are four: a) load, b) depth, c) thermal drift, and d) instrument contact compliance. Having a calibrated nanoindentation instrument the way a single nanoindentation experiment can be set and analyzed is given in details.

3.6.1 Load calibration

Load calibration is carried out by hanging a series of accurately known masses by a hanger located at the bottom of the pendulum shaft. Starting this procedure, weight and voltage magnitudes are recorded in a graph; voltage represents the current that is applied through the coil/magnet system to balance the hanging weights and brings the pendulum at a vertical position. The applied voltage has a linear correlation with the weight, and, knowing the relationship between the weight and voltage in mN/V, for every experiment is easy to control the magnitude of the applied load through the voltage passes through the electromagnetic system. The synchronization of the voltage with the applied load is performed automatically from the software-controller after the user set the load calibration factor in mN/V. Figure 3.7 depicts a schematic representation of the pendulum system, with emphasis on coil/magnet assembly that is used for load application during nanoindentation experiments.

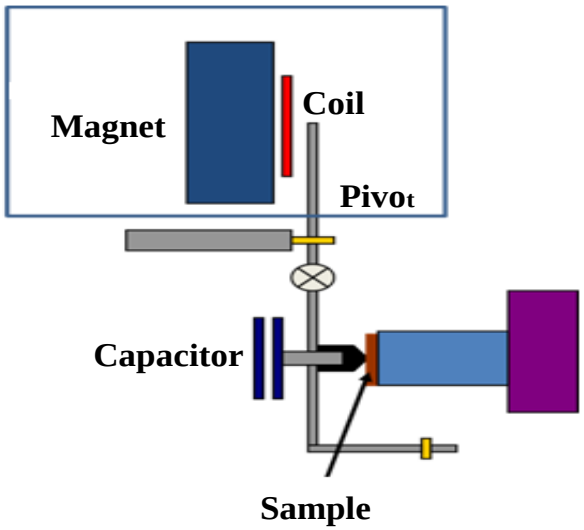

Figure 3.7 An assemblage of the pendulum system together with the electromagnetic driver used for load application. As the application of voltage increases, the current passes through the coil and hence the attractive interaction onto the magnetic material rises bringing the coil-magnet materials more closely. This process introduces motion to the pendulum shaft and the indenter material moves towards the tested material with controlled load.

3.6.2 Depth calibration

The relative displacement of the indenter with respect to the material is recorded by a two plate capacitance system (E − 852 PISeca sensors) that is located at the bottom of the pendulum (see Figure 3.7). Here, one plate is fixed while the other is movable attached on the pendulum. For depth calibration the indenter is maintained fix while the material (usually fused silica) is driven within the indenter by the stepper motors. The known displacement of the material on the indenter is correlated with the measured voltage (i.e., change of charge) between the capacitive system. This routine is performed for various displacement of the material on the indenter. A two parallel plate capacitance system is shown in Figure 3.8. As can be seen the voltage value can be easily correlated with the increase or decrease of capacitors distance.

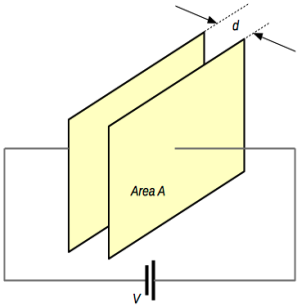

$$C = Q/V = A\varepsilon_0\varepsilon_r/d$$

Figure 3.8 Representation of parallel plate capacitors assembly. Where C = capacitance, Q= magnitude of charge on capacitors, V= magnitude of voltage, A= surface area of one of the plates (SI units: m ^{2}), ε_0= permittivity of empty space 8.854 x 10^{-12} C^2/Nm^2, ε_r= permittivity of material between plates, and d= distance between the plate capacitors (SI units: m). Sketch adopted from http://www.engineeringtoolbox.com.

To summarize, load calibration relates the load with voltage: one therefore defines the voltage required for the application of a specific load (measured in mN/V). Depth calibration relates displacement with voltage so any change of the voltage between the two plate capacitors converts to the linear displacement of the indenter (measured in nm/V). Generally, as voltage in the coil rises, current increases, then the applied load increases, and displacement of two plates increases as well.

In verifying the stability and accuracy of the nanoindentation platform, one can perform various load-unload cycles on fused silica and then compare the load portion of the load-unload tests. Such an experiment is shown in Figure 3.9.

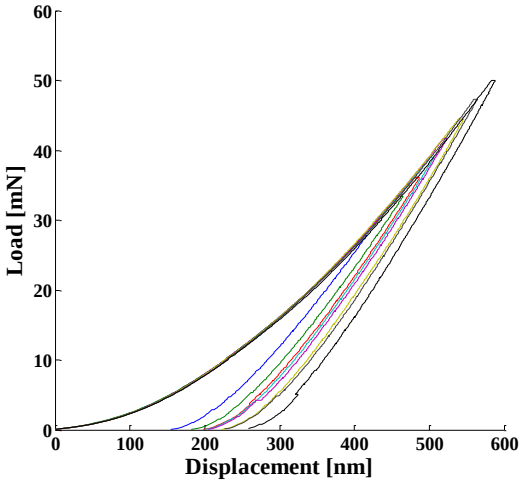

Figure 3.9 Ten load-displacement experiments on fused quartz material using minimum load of 30mN and maximum load of 50mN under control temperature (cabinet temperature 26.5 ^{0}C) and isolation of vibrational and acoustic motions.

As can be seen from Figure 3.9 the loading portions of all curves coincide well while the slopes of the unloading segments deviate because of the different applied maximum loads and subsequently contact stiffnesses. Such results are suggesting a proper stability of the instrument.

Despite the excellent repeatability demonstrated by nanoindentation experiments, any analysis of the accumulated load-displacement data could not yet lead to accurate mechanical results. This is because the load measured in the load-displacement curve is the actual penetration load applied from the load sensor, while, the displacement measured from the displacement sensor is not the actual as part of it could be affected from thermal drift and instrument compliance. These two influencers which lead to displacement inaccuracy demonstrate the need for more calibration so to correct the output load-displacement results before any analysis of the experiments.

3.6.3 Thermal drift calibration

Drift is a phenomenon which causes the indenter to drift to larger or smaller displacements than the actual ones. The drift may be caused by viscoelastic or viscoplastic properties of the material (i.e, creep within the material), and/or, thermal fluctuations because of thermal expansion or contraction of the whole nanoindentation device or thermal effects on the electronics of the system.

Creep is usually associated with polymeric materials and always causes the measured displacement to seem larger than the real. Thermal drift comes entirely from the instrument's thermal effects, making the indenter to draw or withdraw from a material during a measurement and hence yielding to larger or smaller displacement measurements than the actual ones. The thermal drift influence in displacement is always measured and subtracted for every load-unloading experiment.

Suppose that the thermal drift effect is constant during the whole indentation process, often this is measured just before the end of the unloading process by applying a constant low load (usually at 10% of the maximum load) for a set period determined by the user (usually 60 seconds). The load is kept constant at the end of the unloading portion so to avoid possible creep displacement of the material something which is less pronounced at low loads. Figure 3.10 shows an example of indentation load course scheduled on fused silica for collecting thermal drift effect. The contribution of thermal

drift (measured in nm/s) can be readily measured by plotting the displacement as function of the time and then fitting the data using a linear function.

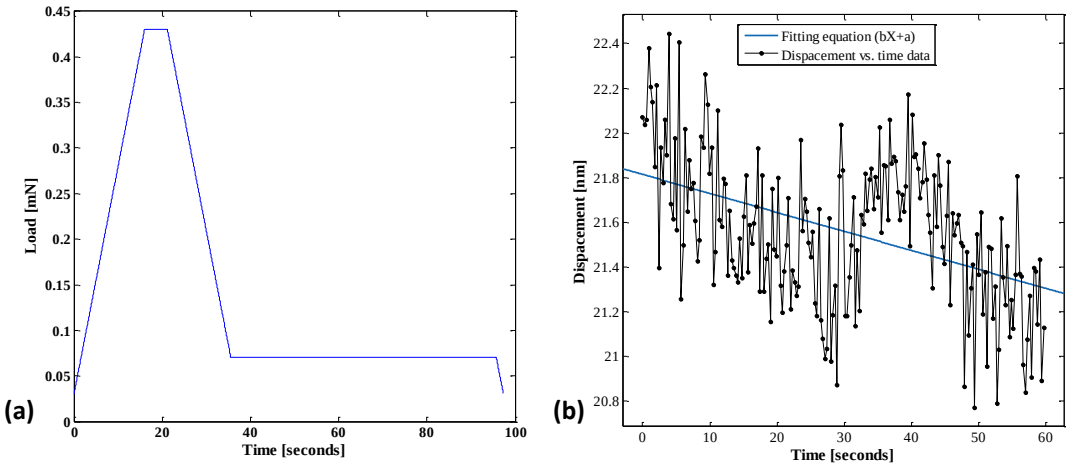

Figure 3.10 (a) An example of a load-time schedule for measuring thermal drift rate. The indenter set to apply a constant load for 60 seconds at the 90% of the unloading portion. (b) Displacement of the indenter for the hold period as function of time for calculating thermal drift rate.

For the indentation test presented in Fig. 3.10 the thermal drift value was calculated at -0.0085 nm/s and shows that the accumulated load-displacement data are recorded to have a smaller displacement compared to the actual. Setting the thermal drift rate to the available software, the correction of the displacement is performed automatically. Figure 3.11 shows an example of this correction where the measured and actual data are presented with blue and green line respectively.

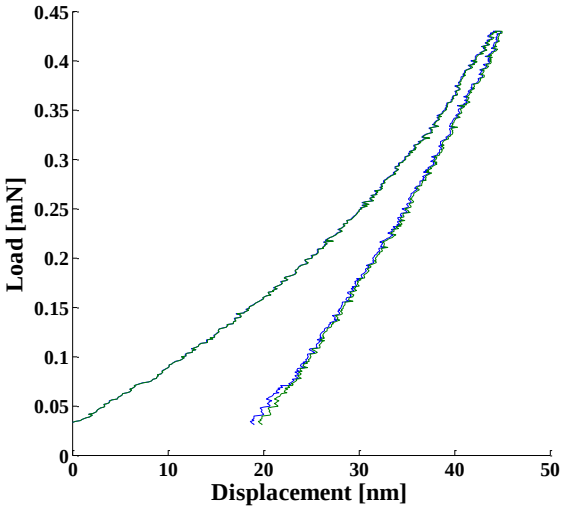

Figure 3.11 Measured (blue line) and corrected (green line) load-displacement data after subtracting the thermal drift rate.

It is worthwhile to discuss that such thermal drift phenomena can be minimized by controlling and stabilizing the operating temperature and humidity. For this reason the whole nanoindentation instrument is enclosed within a cabinet where the temperature is stabilized using a heater. This temperature should be about 2 to 3℃ degrees higher than the outside room temperature so thermodynamically the warm air from cabinet travels always outside the cabinet where the temperature is lower and prevents the opposite phenomenon to happen. The temperature and humidity inside and outside the cabinet should be always monitoring before executing nanoindentation.

3.6.4 Frame compliance calibration

Frame compliance is another factor that must be considered during indentation measurement as it incorporates additional compliance to the system due to external deformation that comes from the instrument itself that needs to be accounted for [68]. Conversely with thermal drift, frame compliance deformation causes the measured displacement to be larger than the actual. The frame compliance contribution is more pronounced when nanoindentation loads are large. In small nanoindentation measurements the effect of frame compliance deformation in data is negligible.

Once the contact compliance is calibrated it can be accounted for in experimental data using the analysis proposed by Oliver and Pharr in 1992 [81]:

$$h_a = h_m - C_f F \tag{3.6}$$

where h_a is the actual penetration depth, h_m is the measured penetration depth, C_f is the frame compliance factor measured in nm/mN, and F is the applied load. The subtraction of this parameter from the accumulated results is usually completed automatically from the software.

There are not a lot of published works that deal with the calculation of frame compliance value, two of which are Refs. [96,97]. Nevertheless the method that is usually used to perform frame compliance calibration is based on the method proposed by Oliver and Pharr: an indenter with known area must is loaded on a material with known elastic modulus and exercising high load on it, the frame compliance can be calculated using Eq. 3.7:

$$C_m = C_s + C_f \tag{3.7}$$

where C_m is measured frame compliance (i.e., the reciprocal of contact stiffness), and C_s the material compliance (i.e., the reciprocal of the material stiffness) which can be calculated by solving Eq. (3.2) for S.

3.6.5 Execution of nanoindentation experiment

A nanoindentation test can be easily set by using the nanoindentation software. In this paragraph we describe the general procedure to obtain nanoindentation data. The basic steps for measuring nanoindentation data are as follows:

1. Sample preparation: It is necessary for any sample to be cleaned with compressed air before testing so any dust particle or other form of contamination that may affect the test to be removed.
2. Sample mounting: The sample must be well glued on specific aluminum stub. The size and weight of the tested sample should be small so to avoid influence on frame compliance and any distortion of the instrument in case the sample fallen from the sample stub during testing.
3. Placement of sample stub on nanoindentation platform: This is done by a screw component supplied by the manufacturing company.
4. Sample-tip approach: The approach step needs from the user to observe the motion of the stepper motors until the sample is brought very close to the tip. The approach is completed automatically with the nanoindentation software by setting a safety velocity for the stepper motors until contact is detected.
5. Retraction distance: When contact is established the user must retract the sample so does not touch the tip anymore (usually the retraction distance is set to 25 μm).

6. Setting testing parameters: setting parameters include indenter load, indenter loading rate, dwell time and unloading rate. A grid pattern can be set according to the material under investigation.
7. Start nanoindentation experiment: the experiment can be adjusted to start whenever the user wishes.
8. Tip withdraw: When the test is completed the sample is removed and data can be collected, analyzed and interpreted.

3.6.6 Example of nanoindentation test on fused silica

To verify the calibration results we conducted a simple nanoindentation test on a reference material. Figure 3.12 shows a simple indentation test on fused silica using a maximum load of 200 mN and a three faced pyramid Berkovich type indenter, at a controlled temperature and vibration/acoustic isolation environment.

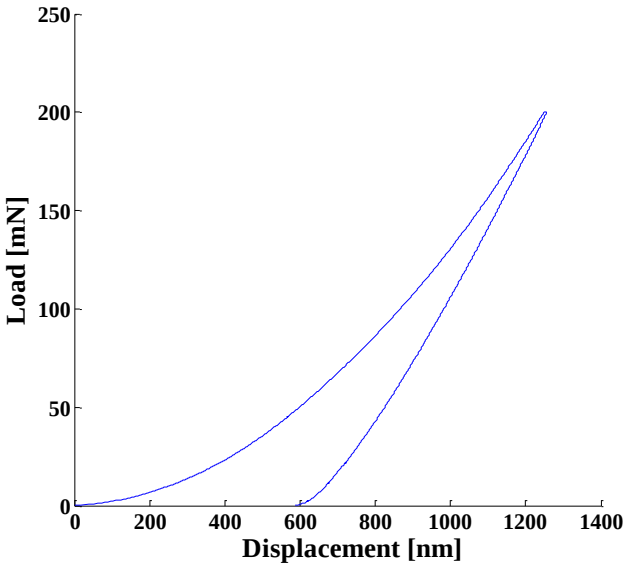

(a)

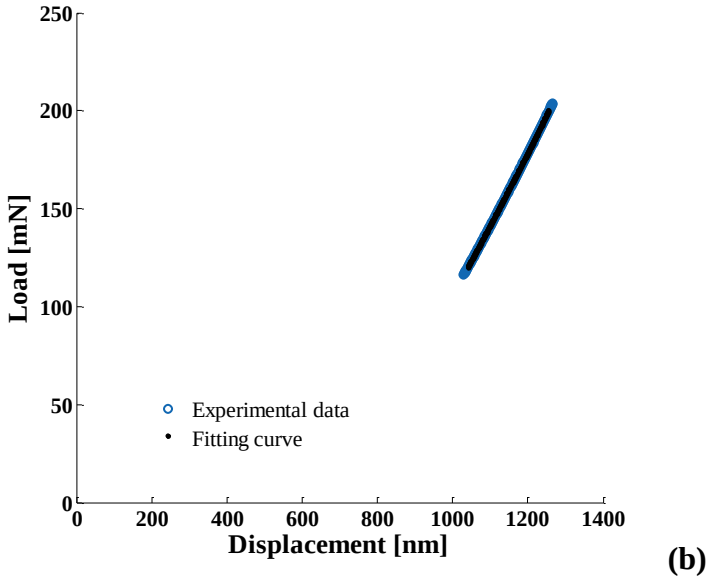

Figure 3.12 (a) Indentation test on fused silica reference sample using a Berkovich type indenter and a maximum load of 200mN. (b) Fitting process for calculating the contact stiffness.

Basic mechanical properties that can be derived from the curve of Figure 3.12 are hardness and elastic modulus. Both properties are defined from Eqs. (3.1) and (3.2), where again, F_{max} is the maximum indenter load, E_r is the reduced modulus (depended on specimen and indenter properties), and, S is the contact stiffness which is calculated from the slope of the unloading curve at maximum load. The process for calculating the contact stiffness is presented in Figure 3.12 as well. Here the 20% of the unloading data were plotted and then fitted by the power law relationship as proposed by Oliver and Pharr [81]. The general power law relationship has the following form, $F = a(h - h_f)^m$ (see also Eq. (3.4)) where a and m are fitting parameters and h_f is the experimental final depth of residual imprint. Here the calculated fitting equation has the form of $F = 0.03954(h - 587.15)^{1.311}$ and a differentiation with respect to h evaluated ta maximum depth, gives a gradient of $dF/dh = 0.39$ (corresponding to a material contact compliance value of $2.57\ mN/nm$).

The contact area, A, is a function of the contact depth. The contact area, A, is an indenter property that is needed to be defined prior to any experiment. Various methods have been reported for estimating the contact area using for example atomic force microscopy, scanning electron microscopy or the Hertzian equation for elastic contact [98–101], nevertheless the most common used method was the method proposed by Oliver and Pharr [81] by using a polynomial equation that predicts the contact area through an area function (see Figure 3.2).

The experimental procedure to calculate the contact area involves penetrating within a material many times by changing for each load - unload cycle the maximum load and from calculation of the contact depth for each cycle a plot is formed that correlates the contact area with contact depth, assuming that the elastic modulus of the tested material is constant and not change with penetration depth. Usually this procedure is performed for calibrating the very apex tip of the indenter. For deep indentation, higher than 1000 nm, where the indenter is not blunt, the polynomial that predict the ideal shape of the Berkovich indenter can be well used to predict the contact area:

$$A = 24.56h_c^{\,2} \tag{3.8}$$

Using the above values for frame compliance and contact area, the calculated hardness and reduced elastic modulus for the fused silica sample was found to 8.77 ± 0.06 and 70.25 ± 0.32 respectively and are in excellent agreement with literature values [81].

3.7 Chapter summary

This Chapter dealt with nanomechanical testing of materials using an instrumented indentation platform. Particular emphasis has been placed on nanoindentation and nanoscratch tests that are the two types that have been particularly exploited for the nanomechanical and nanotribological characterization of amorphous carbon metal films deposited within this thesis. It becomes apparent that provided the instrument is calibrated properly, load and depth measurements can be performed with nN and angstrom scale accuracy, which provide powerful means of quantifying the mechanical response of thin films. This is exploited within the investigations presented in Chapters 4 to 7.

CHAPTER 4 Microstructure and nanomechanical properties of pulsed laser deposited DLC:Ag films[1]

4.1 Introductory remarks

While DLC: Ag nanocomposites have been deposited via several routes [102–104], a systematic study on the synthesis, microstructural characterization and nanomechanical/nanotribological response is still lacking. We here report on the pulsed excimer laser deposition and systematic characterization of silver-doped DLC materials with silver compositions ranging from 0 to 16.8 at. %, in contrast to pulsed laser deposited DLC: Ag films using a Nd: YAG laser source, whose major drawback was the severe graphitization of the DLC matrix resulting in the elimination of the sp^3 states for Ag contents less than 10 at. % [102,105]. The produced DLC: Ag films are characterized for their microstructure, crystallinity, surface roughness, residual internal stresses and nanomechanical response. Particular emphasis is placed on the evolution of the nanotribological response of the material with the silver content.

4.2 Materials and methods

4.2.1 Synthesis of DLC:Ag films

Non-hydrogenated DLC and DLC: Ag films were deposited on Si n + (100) substrates using room temperature pulsed laser deposition with a base pressure of 2×10^{-5} mbar. The Si substrates were ultrasonically cleaned in a sequence of de-ionized water, acetone, methanol, isopropanol and de-ionized water, followed by high purity N_2 gas drying. A KrF coherent laser source (COMPex Pro) at 248 nm with pulse width of 25 ns at full width at half maximum and pulse repetition rate of 10 Hz was used for the ablation of the target (Figure 4.1(a)). Graphite (G) and Graphite/Silver (G/Ag) sector targets (Figure 4.1(b)), where the Ag piece covering the graphite varied in size in order to achieve

[1] Results presented in this chapter have been published in the following paper: M. Constantinou, M. Pervolaraki, P. Nikolaou, C. Prouskas, P. Patsalas, P. C. Kelires, J. Giapintzakis, G. Constantinides 'Microstructure and nanomechanical properties of pulsed excimer laser deposited DLC:Ag films: enhanced nanotribological response' Surface and Coatings Technology, 309, 320-330, 2017.

between 0 and 16.8 at. % Ag content, were rotating and rastering continuously during the ablation process and placed at a distance of 3.5 cm from the substrate. The target was rotated at 10 rpm and toggled at 10 steps per second forward and 10 steps per second backwards for all depositions. Optimization of the laser pulse repetition rate and continuous rotation/toggling of the target ensured irradiation of fresh area resulting to the desired Ag contents and smooth surface of the films. It is apparent that an increase in the Ag coverage (by varying the surface area of the silver strip with respect to the pristine graphite target) of the G/Ag sector target resulted in an increased silver content in the deposited composite material, reaching a maximum of 16.8 at. % for the growth conditions used in this study. It should be noted that the carbon to silver ratio is not identical to the atomic composition ratio used on the G/Ag sector target and this could be related to the higher laser ablation tendency of silver in comparison to carbon [106,107]. The laser fluence was set at 9 J/cm^2 for all depositions and under these conditions the working pressure of the ablation plume did not exceed 5×10^{-5} mbar. Three hundred pulses were used to pre-ablate the surface of the target and four thousand pulses were used for the deposition process, which resulted in film thicknesses of approximately 125 ± 5 nm, as measured through optical profilometry on film-substrate steps. Residual compressive stresses generated during deposition have been quantified through the Stoney formula by measuring the substrate curvature after deposition using optical profilometry.

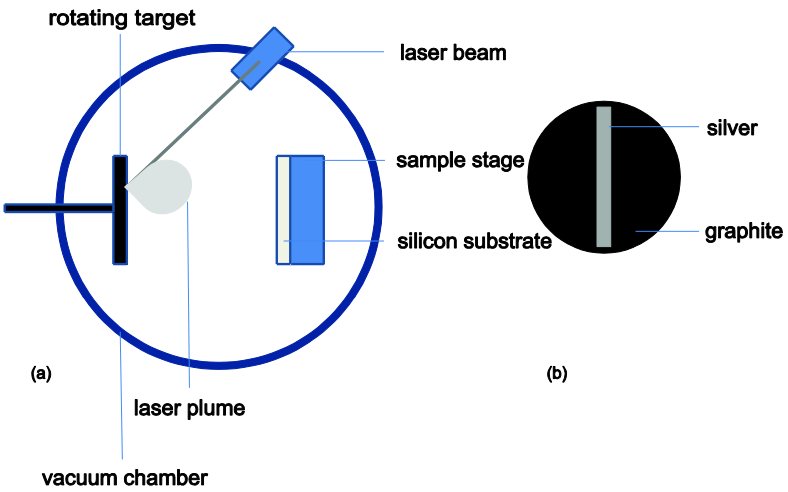

Figure 4.1(a) Schematic of the pulsed excimer deposition system used in this study. (b) Geometric details of the rotating sector target used for depositing DLC:Ag nanocomposites.

4.2.2 Microstructural characterization

Ex-situ X-ray photoelectron spectra were acquired in a surface analysis ultrahigh vacuum system (SPECS GmbH) equipped with a twin $Al - Mg$ anode X-ray source, a hemispherical sector electron analyzer (HSA-Phoibos 100), and a multichannel electron detector. The pass energy was $20\,eV$, providing a full width at half maximum of $1.18\,eV$ for the Ag $3d_{5/2}$ line of a continuous Ag film. Elemental concentrations were determined by analyzing the wide scan spectra taking into account the relevant sensitivity factors [108], while the sp^2 and sp^3 contents were determined by deconvoluting the $C1s$ core level spectra; all the quantification analyses were carried out using the CasaXPS software. In addition to XPS measurements, X-ray diffraction patterns were collected in a Rigaku Ultima IV system equipped with copper (Cu Kα) radiation ($\lambda \sim 1.54$ Å) using voltage and current values of 40 kV and 40 mA, respectively. The measurements were performed in a grazing incidence mode with an angle of incidence of $a = 0.6°$ and diffraction angles (2θ) of 30 to $50°$ using a $0.01°$ step width and a $0.5\,°/min$ scan speed.

The surface topography of the deposited films has been studied using atomic force microscopy (AFM) images obtained in contact mode at room temperature and controlled humidity ($\approx 30\%$) using a Scanning Probe Microscope (Ntegra Prima, NT-MDT). An NT-MDT probe (CSG10) having a mean force constant of $0.11\,N/m$ and a nominal tip radius of 6 nm was used. Images of $3\,\mu m \times 3\,\mu m$ collected with a tip scan rate of 1Hz and resolution 256×256 points were subsequently software-analyzed for extracting the root mean square (RMS) roughness of the surfaces.

4.2.3 Nanomechanical characterization: nanoindentation

The nanomechanical characterization of the DLC and DLC: Ag films was performed using an instrumented indentation platform (NanoTest, Micromaterials Ltd, UK) [71,109,110]. The samples were tested in a load-unload (single depth) and a load-partial-unload (multi-depth) mode using a diamond tip of the Berkovich type. During the indentation process the applied load (P) and corresponding depth of penetration (h) were continuously monitored with nanoscale accuracy – 100 nN for load and 0.1 nm for displacement. In the single depth nanoindentation investigation the specimens were probed using a maximum load of 2mN. A 60s dwell time was introduced at 90% of

unloading force in order to collect data for thermal drift corrections. Twenty indents ($P-h$ curves) at various locations on the film surfaces were used for calculating the average Elastic Modulus (E), Hardness (H), maximum penetration depth (h_{max}), plastic depth (h_p), elastic work (W_{el}) and plastic work (W_{pl}) of indentation. In a typical load-partial-unload experiment the indenter penetrates into the material in 20 load cycles in the 0.3 to 5 mN prescribed load range. In this type of experiment the extracted mechanical metrics (like E and H) are monitored as a function of indentation depth ($E(h)$ and $H(h)$) and provide the possibility of excluding any substrate influence on the film's mechanical response. Forty load-partial-unload indentation experiments were performed on each sample at different locations and average quantities are calculated. All experiments were executed in a controlled environment with $\sim 30\%$ humidity and 25 oC temperature.

The hardness (H) and reduced elastic modulus (E_r) of the film/substrate system were calculated at each cycle (specific depth) using:

$$H = \frac{P_{max}}{A_c} \tag{4.1}$$

$$E_r = \frac{\sqrt{\pi}}{2}\frac{S}{\sqrt{A_c}} \tag{4.2}$$

where P_{max} is the maximum applied load, S is the unloading slope at maximum depth $S = \left.\frac{dP}{dh}\right|_{h=h_{max}}$, and A_c is the projected area of contact generated between the indenter and the specimen at maximum load. The elastic modulus of the material can be calculated through Eq. (4.2) which derives from the analytical solution of a rigid axisymmetric probe being pushed on the surface of linear elastic half space [111] and provides a link between the unloading contact stiffness S with the reduced elastic modulus of the material E_r [69]. E_r is associated with the combined deformation actions of the material and the indenter through:

$$\frac{1}{E_r} = \frac{(1-{v_i}^2)}{E_i} + \frac{(1-{v_s}^2)}{E_s} \tag{4.3}$$

where E_s and v_s, and E_i and v_i, correspond to the elastic moduli and Poisson's ratios of the material and indenter, respectively. In our experiments a diamond Berkovich indenter is used with $E_i = 1140$ GPa and $v_i = 0.07$. With the exemption of A_c all other

quantities are experimentally obtained from the $P-h$ response. The area of contact is estimated using the Oliver and Pharr methodology in which A_c is calculated as a function of experimentally obtained parameters [69]. The imperfect indenter geometry is taken into consideration through a calibration process that preceded all measurements. During the calibration process a multi-depth experiment is performed on a material (fused quartz) with known mechanical properties ($E = 69.9$ GPa and $H = 9.0$GPa) and through an inverse analysis of Eq. 4.2 the actual indenter geometry is calculated as a function of the indentation depth ($A_c = f(h)$), Diamond Area Function or DAF in short) [100]. In this study the DAF was calibrated in the indentation depth range of $5-130$ nm.

4.2.4 Nanomechanical characterization: nanoscratch

The nanotribological characteristics of the deposited films have been studied using nanoscratch testing [72,112,113]. During a nanoscratch test, the investigated sample is moved perpendicular to the scratch probe while at the same time the contact normal load (P^N) is ramped at a pre-defined rate. Throughout the test the probe penetration depth (h) and tangential (frictional) load (P^T) are continuously monitored. Figure 4.2(a) shows the loading profile during a scratch test with a 5 μm (nominal value) end radius conospherical probe scanning over a 450 μm track at a scan speed of 2 μm/s. A pre-scratch scan was carried out using an ultra-low contact force (0.1 mN) in order to assess baseline sample topography. The blue line in Figure 4.2(b) shows the on-load probe depth, which represents elastic and plastic deformations. After 50 μm the load is ramped at 1.75 mN/s until a maximum force of 350 mN is reached. The green line in Figure 4.2(b) shows the residual (plastic) depth once the scratch load has been removed; both on-load depth and residual depth have been corrected for initial sample topography. Friction force measurements are carried out throughout the test giving access to the evolution of friction coefficient, $\mu = P^T/P^N$ (Figure 4.2(c)). Five scratch tests have been performed on each film. The nanoscratched films were subsequently imaged in a Quanta 200 (FEI, Hillsboro, Oregon, USA) Scanning Electron Microscope at various magnifications. All images were obtained using a voltage of 10 to 20 kV and a working distance of 10 to 11 mm. The SEM images (an example is shown in Figure 4.2(d)) were used to correlate morphological features with nanotribological characteristics.

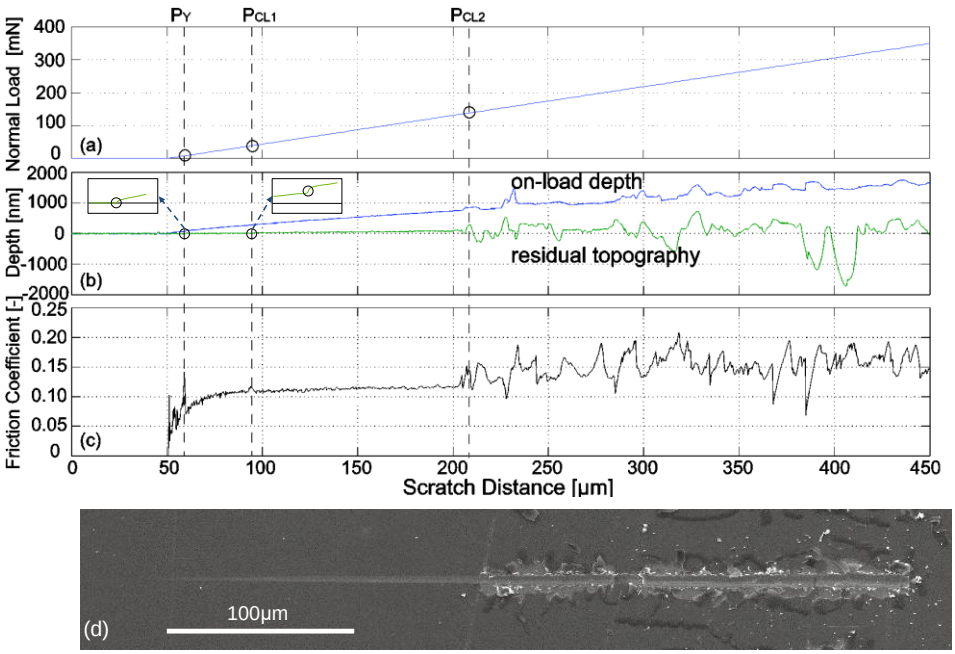

Figure 4.2 Typical results collected from a ramped load nanoscratch test. (a) Pre-defined load profile, (b) resulting on-load depth and residual topography, (c) evolution of friction coefficient and (d) SEM image of residual scratched surface.

4.3 Results and discussion

4.3.1 Microstructural and morphological characteristics

Figure 4.3 shows 3µm × 3µm AFM images of the deposited films. The pure DLC films exhibit a very smooth profile with sub-nanometer roughness (0.15 ± 0.04 nm) consistent with values reported in the literature [114,115]. The incorporation of silver has only a minor influence on the surface roughness of the DLC: Ag films with a notable exemption the case of DLC: $Ag_{16.8at.\%}$ that shifts the roughness into the nanometer regime (5.81 ± 1.56 nm), due to agglomeration of Ag on the surface. In general the roughness of amorphous carbon systems is affected by temperature, surface mobility and graphitic recrystallization. In our experiments the temperature was kept constant among all depositions while surface mobility and graphitic recrystallization varied as the Ag doping content was increasing. The calculated RMS roughness for all grown specimens are reported in Table 4.1. Table 4.1 also reports the chemical compositions of the grown films and the hybridization states of the amorphous carbon matrix as have been quantified through the XPS data. The C1s core level spectra (Figure 4.4) are very

sensitive to sp^2 and sp^3 contents in amorphous carbon [116] and amorphous carbon-metal nanocomposites [117]. On the other hand, the Ag concentration of the films was determined by the relevant wide-scan spectra (inset of Figure 4.4) and the Ag $3d_{5/2}$ and Ag $3d_{3/2}$ XPS peaks located at 368.4 eV and 374.4 eV, respectively. The sp^3 and sp^2 contents in the amorphous carbon matrix of the films were determined by deconvoluting the core level C1s spectra to three individual contributions: $C-C$ bonds in sp^2 configuration at 284.6 eV, $C-C$ bonds in sp^3 configuration at 285.5 eV, and $C-O$ due to surface contamination at 286.4 eV according to Ref. [116,117] as shown in Figure 4.5 for the two extreme cases of amorphous Carbon films of this work.

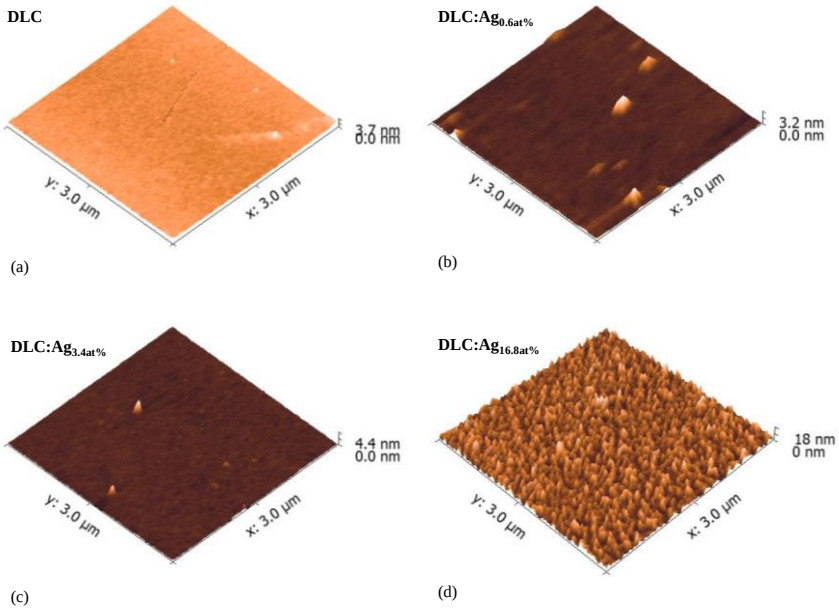

Figure 4.3 AFM images of (a) DLC, (b) DLC:$Ag_{0.6at.\%}$, (c) DLC:$Ag_{3.4at.\%}$, (d) DLC:$Ag_{16.8at.\%}$.

Table 4.1: Microstructural characteristics of DLC:Ag films.

Material	Roughness [nm]	Ag [at.%]	sp^3 [%]
DLC	0.15 ± 0.04	0	77.1
DLC:$Ag_{0.6at\%}$	0.18 ± 0.04	0.6	72.6
DLC:$Ag_{3.4at\%}$	0.32 ± 0.05	3.4	48.2
DLC:$Ag_{7.8at\%}$	0.30 ± 0.02	7.8	40.4
DLC:$Ag_{16.8at\%}$	5.81 ± 1.56	16.8	36.0

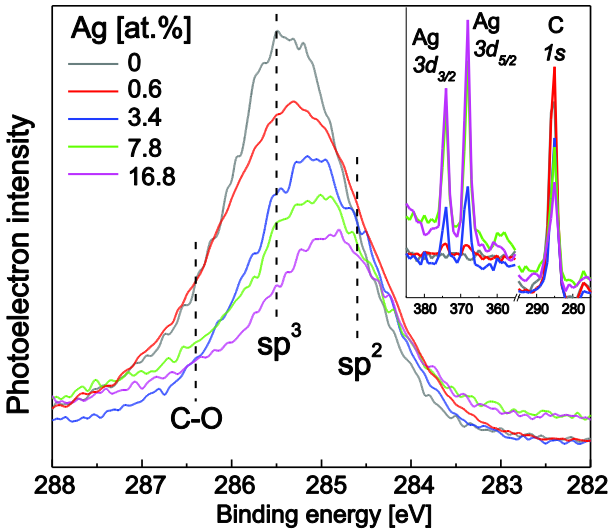

Figure 4.4 C1s core level photoelectron spectra for the five synthesized DLC:Ag films. Inset: Wide scan spectra showing both silver and carbon peaks.

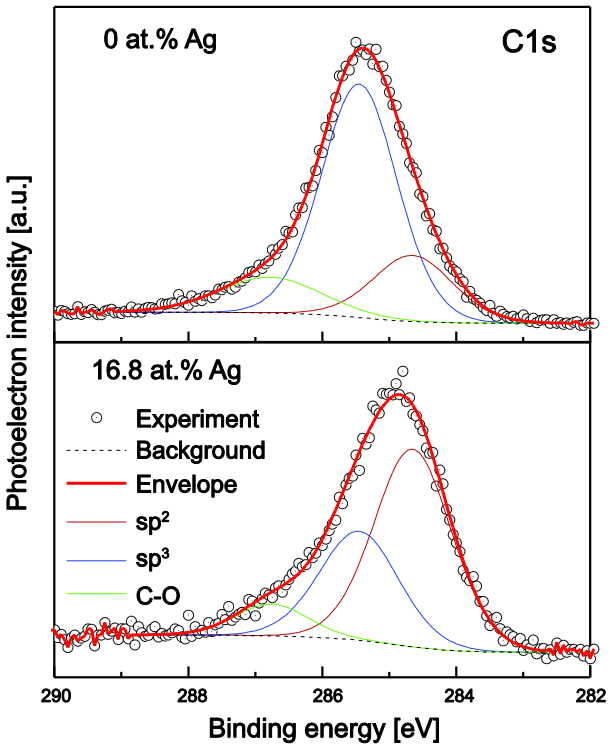

Figure 4.5 Deconvoluted XPS C1s core level spectra for the two extreme compositional cases; pure DLC and DLC:$Ag_{16.8at.\%}$.

Consistent with previous reports, the incorporation of silver into the DLC graphitizes the matrix through a process of $C-C$ bond breaking at the DLC-metal interface that favors the three-fold coordinated C arrangement (sp^2 hybridization) [48,102]. The graphitization of amorphous carbon matrix due to the incorporation of Ag in the films is quantified in Figure 54 in comparison with other cases of PLD-grown DLC: Ag nanocomposites produced with different laser, fluences and wavelengths. Note that the composition data from Ref. [102,105] were acquired by Auger Electron Spectroscopy, which is more surface sensitive than XPS [108,116,118] possibly resulting in underestimation of both sp^3 content due to their graphitic surface [119,120], and the Ag concentration due to adventitious Carbon on the surface (as testified by the existence of $C-O$ bonds); nevertheless the complete graphitization of the matrices of the films from Ref. [102] and [105] is supported by their optical spectra [105], which take into account the whole volume of the films. It is evident from Figure 4.6 that while the tendency of graphitization with silver incorporation is clear in all cases, the excimer PLD-grown DLC: Ag films sustain a substantial sp^3 content (36 %) in their matrices even for the highest Ag content (16.8 at. %) in contrast to the films grown by PLD using a Nd: YAG

laser source and reported in Ref. [102,105], which can be attributed to the different laser wavelength (and consequently photon energy) and fluence, as well as the more uniform distribution of energy across the beam in the excimer source compared to the Nd:YAG source. In PLD the ionization of the deposited species is taking place via multi-photon ionization of the evaporated Carbon atoms by the laser beam. As explained and demonstrated in [121], the laser fluence and wavelength (and consequently its energy as well) are critical parameters for the ionization degree and energy. In general reducing the laser wavelength or decreasing the fluence results in materials with higher sp^3 contents and subsequently with higher density and improved mechanical characteristics.

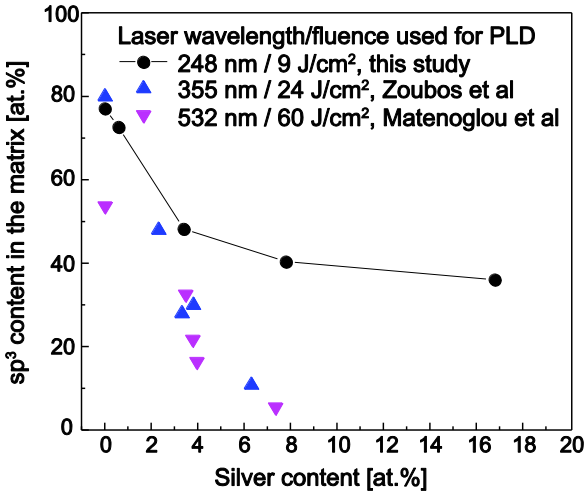

Figure 4.6 sp^3 content evolution, as quantified through XPS data, with silver content. Literature data: Zoubos et al. [105]**, Matenoglou et al.** [102]**.**

Figure 4.7 shows the XRD data collected for all specimens. Peaks located at ~38° and ~44° respectively, which have been present in all deposited films (except for pure DLC) and correspond to the (111) and (200) Silver diffraction planes indicate the crystalline nature of Ag clusters within the amorphous carbon matrix. This is consistent with the low miscibility between Silver and Carbon and the tendency of the material to self-assemble into nanocrystalline domains consistent with other experimental XRD and TEM data reported in the literature [102,106,122]. Crystallite size estimates obtained through the application of Scherrer equation on the (111) peak suggest crystalline domains on the order of 2.5 to 4 nm; the narrowing of the full width at half maximum in X-ray peaks as the Silver content increases corresponds to an increase in the crystallite size, consistent with what has been reported in Matenoglou et al. [102]. The

nanometric crystalline domains calculated above are in close agreement with the height measurements of individual particles detected through AFM images on the surface of the deposited films (see Figure 4.3). The lateral characteristics of the surface morphological features of Figure 4.3 appear to be higher than the size of crystallites and while this can be attributed in part to tip-sample convolution phenomena, one cannot exclude the possibility of particles agglomerating is small groups.

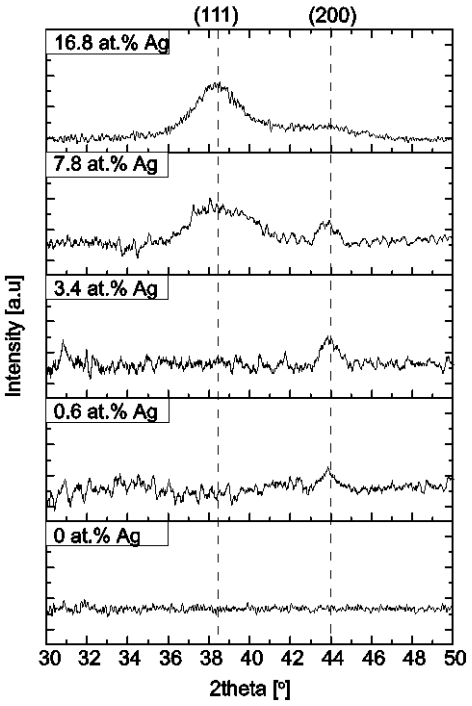

Figure 4.7 GI-XRD diffractograms for all the DLC:Ag films deposited in this study. The vertical lines indicate the angular position of the diffraction peaks of the low index fcc silver planes.

4.3.2 Nanomechanical response: single depth indentations

Figure 4.8(a) shows typical $P-h$ curves collected during single depth nanoindentation experiments to a maximum load of $2\,mN$. In general the repeatability of the nanoindentation tests at various locations was very good, testifying towards the spatial homogeneity (both in terms of thickness and composition) of the synthesized materials. All of the extracted and calculated nanomechanical metrics are summarized in Table 4.2. The introduction of silver into the DLC matrix results in a reduction of the resistance to penetration as shown in Figure 4.8(a): for the same applied maximum load ($2\,mN$) the maximum penetration depth gradually increases from $49.5\,nm$ (pure DLC) to $74.3\,nm$ (DLC: $Ag_{16.8at.\%}$). This softening response which can also be observed in the Elastic Modulus and Hardness of the films (Figure 4.8(b)) can be attributed in part to

the introduction of the softer/compliant silver material and in part to the graphitization of the amorphous carbon matrix caused by the introduction of silver nanoparticles. Finally, it is interesting to note that while the elastic energy component of the work of indentation remains invariant to the doping process, the plastic component gradually increases (see data in Table 4.2), signifying the increased ductility of the nanocomposite material. The ductility of the indented material can be quantified through the plastic work ratio, $W_{pl}/(W_{el}+W_{pl})$ which appears to increase from 12% for the pure DLC case to a maximum of 35% for DLC: $Ag_{7.8at.\%}$ and signifies the ability of the material to absorb energy in the form of plastic deformations.

While the single depth nanoindentation experiments provide a snapshot of the mechanical response of the various synthesized DLC: Ag nanocomposites the results are subject to a certain degree of influence by the silicon substrate, which grows in importance as the depth of penetration becomes comparable with the film thickness [79,123,124]. To exclude any substrate phenomena and calculate film-only mechanical properties we have performed multi-depth nanoindentation experiments and extrapolated the mechanical response to zero-depth; these are discussed next.

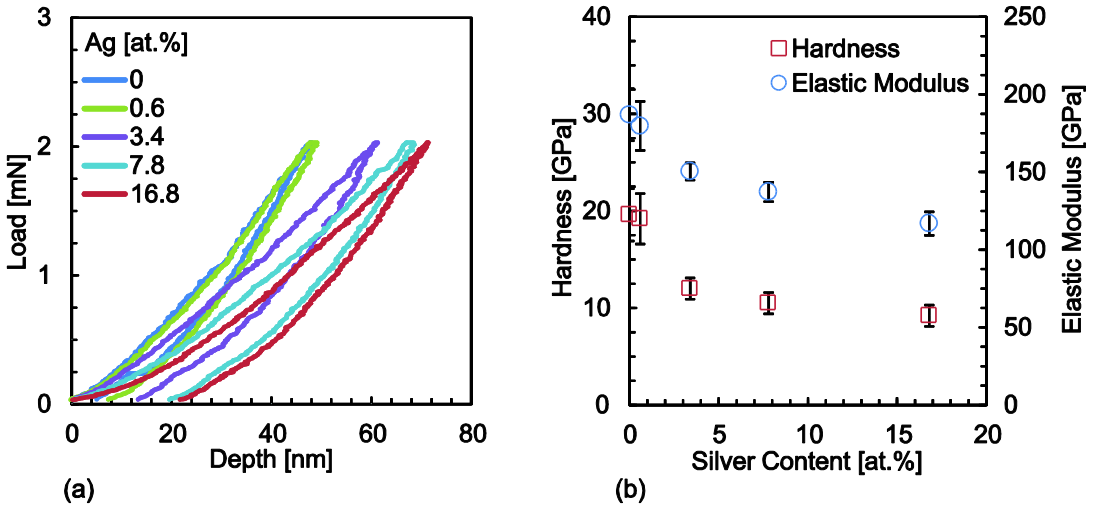

Figure 4.8 (a) Effect of silver doping on (a) the P-h response and (b) on the calculated elastic modulus and hardness of the synthesized films.

Table 4.2 Average mechanical values from 20 different indentation tests on DLC and DLC:Ag films probed using single load of 2mN.

Material	Max. depth	Plastic depth	Hardness	Elastic modulus	Plastic work	Elastic work
	[nm]	[nm]	[GPa]	[GPa]	[nJ]	[nJ]
DLC	49.5±2.2	27.6±3.0	19.6±2.7	186.9±16.8	0.007±0.003	0.039±0.002
DLC:$Ag_{0.6at\%}$	50.6±2.0	28.2±3.1	19.2±2.6	179.7±15.8	0.007±0.003	0.038±0.002
DLC:$Ag_{3.4at\%}$	62.2±1.9	41.1±2.8	12.0±1.1	150.4±5.5	0.018±0.004	0.039±0.002
DLC:$Ag_{7.8at\%}$	67.3±3.0	45.6±3.5	10.5±1.1	137.1±6.2	0.020±0.005	0.040±0.002
DLC:$Ag_{16.8at\%}$	74.3±4.6	50.5±5.0	9.2±1.1	116.9±7.6	0.020±0.003	0.042±0.002

4.3.3 Nanomechanical response: multi-depth indentations

The average hardness values of 20 indentation experiments at different depths for the case of pure DLC are presented in Figure 4.9(a). It is evident that the hardness values of the tested film is influenced from the existence of the substrate (in our case silicon wafer) which is manifested on the hardness vs. depth plot as a continuously decreasing mechanical response with increasing indentation depths, gradually approaching the substrate response. This is consistent with the reported response of hard films on soft substrates, in which film hardness is underestimated when the indentation depth becomes comparable with the film thickness [79,125]. Moreover, the decrease of hardness for very small indentation depths can be attributed to the tip blunting, which causes a gradual transition between elastic and elastic-plastic film response. The maximum hardness is commonly taken as the film's hardness but a more detailed analysis entails the application of a mechanical model and the extrapolation of the curve to zero penetration depth where hardness film values unaffected by the substrate can be extracted (intercept with the y-axis) [126]. In our study the Bhattacharya and Nix model [82] was fitted to our experimental data in order to extract the actual film hardness values:

$$H_f = H_s + (H_f - H_s)e^{\left(-\frac{h_c}{t}\times\frac{H_f}{a}\times\frac{\sqrt{E_s}}{H_s}\right)} \quad (4.4)$$

where H_f, the film hardness, and a, a material-dependent parameter, were calculated through a least square minimization process. The hardness and elastic modulus of the substrate were predefined based on nanoindentation experiments on silicon ($H_s = 10.6 \pm 0.1$ GPa and $E_s = 169.4 \pm 3.7$ GPa) whereas the contact depth to thickness ratio (h_c/t) was experimentally obtained; h_c represents the contact depth at each penetration

and t the film thickness which was measured to be $\sim 125\,\mathrm{nm}$ for all films. The Bhattacharya and Nix model has been generated through extensive elastic-plastic finite element simulations, which have been shown to display very good resemblance to experimental data of hard films on soft substrates [82].

Figure 4.9(b) summarizes the hardness values of all tested films as a function of the $sp^3\%$. As expected, the undoped DLC film exhibits the highest hardness with value of $24.4 \pm 2.2\,\mathrm{GPa}$, within close agreement with what is reported in the literature for specimens with similar $sp^3\%$ content. The inset of Figure 4.9(b) contrasts the measured hardness of pure DLC with the data presented in Xu et al. [15], confirming the validity of the adopted methodology. The introduction of Ag into the DLC system leads to a significant reduction of hardness (Figure 4.9(b)), which in the case of DLC: $Ag_{16.8at.\%}$ is on the order of -50%. As stated earlier, this mechanical capacity drop is attributed to silver which on one hand creates a softer nanocomposite (hardness of silver has been calculated/measured around $\sim 1\,\mathrm{GPa}$ [127–129]) and on the other hand graphitizes the DLC matrix by reducing the $sp^3\%$ into the 40 % range (a matrix with more sp^2 bonds is softer than an equivalent with more sp^3 bonds), as demonstrated by the XPS data (see Table 4.1 and Figure 4.6). Since the introduction of silver activates two softening mechanisms the slope of the H vs. $sp^3\%$ experiences a deviation from the scaling presented on pure DLC systems. From a material engineering point of view, it is interesting to note here that the $sp^3\%$, and subsequently the DLC: Ag properties, can be tailored by controlling the various deposition parameters (laser fluence/wavelength, metal content, etc.).

A comparison of mechanical properties obtained from single depth indentations (Table 4.2) with the results extracted from multi-depth indentation (Figure 4.9) suggest discrepancies on the order of $20 - 25\%$. This result quantifies the effect of film thickness and substrate on the composite mechanical response and presents the underestimation of film hardness that one would have obtained should he/she neglected to perform a more detailed multi-depth experimental investigation.

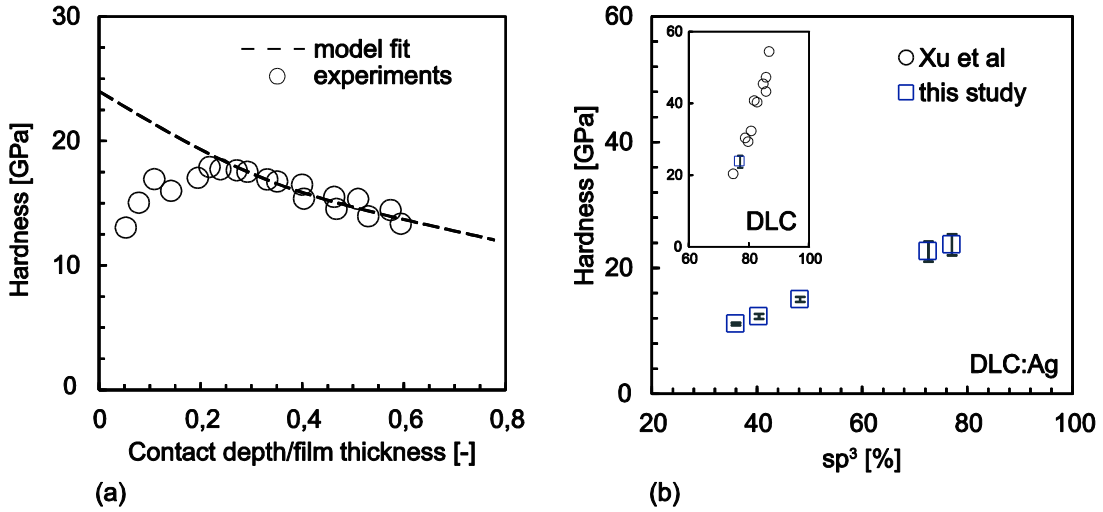

Figure 4.9 (a) Multi-depth hardness measurements for DLC. (b) Hardness vs. sp^3 % for all DLC:Ag films deposited in this study. Data in inset compares pure DLC hardness measurement obtained in this study to literature data from Ref. [15].

4.3.4 Nanotribological response

The high load- and depth-resolution provided by the nanoscratch platform was exploited for tribological characterization of the deposited thin films. The main advantage of the nanoscratch test, compared to conventional micro scale scratch tests relates to the ability of the platform to record the surface profiles before, during and after the test, with nanoscale resolution. Subsequently, much lower loads can be employed and thin films can be studied, although probes with smaller radii are required in order to induce sufficiently large contact pressures for plastic deformation, cracking and eventually film failure to occur [112]. The nanoscratch test, while not yet standardized, has been recently studied in more depth and several test-related conclusions have been drawn: the scratch speed, loading rate, and the increase in load per unit length (provided that this is smaller than $1\ \mathrm{N/mm}$) have no significant impact on the measured critical loads for yield and failure [113,130]. The two major parameters that affect scratch response are the probe radius and film thickness [113,131,132]. When either of the two are increased, the critical load required for film failure increases. These two parameters have been kept constant in our study such as the experiments conducted on various DLC: Ag compositions can be directly contrasted. The probe radius has been calibrated by performing elastic indentations on quartz and fitting the $P-h$ data with Hertz's solution; the resulting radius was found to be $3.2 \pm 0.1\ \mu\mathrm{m}$ [100].

The ramped load multi-pass scratch method utilized in this study has been presented and utilized in several publications [112,130,133,134]. From the scratch data, three critical loads can be identified that relate to the three transition points (Figure 4.2) that the film/substrate system undergoes during a scratch test [112,135]:

1. P_y is the critical load that signifies the onset of plastic deformations and is identified through the initiation of plastic (permanent) deformations on the residual surface profile scan (inset in Figure 4.2(b))
2. P_{CL1} relates to the critical load required to initiate edge cracking and can be identified through a kink on the post-scratch topography (inset in Figure 4.2(b))
3. P_{CL2} is the critical load that correlates with complete film failure and can be identified through the discontinuity in either the post scratch topography or friction coefficient.

These transitions and related microstructural features have been confirmed through SEM investigation of scratch tracks. The extracted nanotribological metrics for all tested films are listed in Table 4.3. At first observation P_y appears to scale inversely with the silver content. Beake et al. [72] have tested $\mathrm{ta-C}$ films of $5-150\mathrm{nm}$ thicknesses on silicon substrates with similar responses. Using a Hertzian contact mechanics analysis they concluded that the yielding recorded early on the scratch tests and associated with P_y related to yielding of the substrate rather than of the film itself. In doing so they converted the critical load required to initiate plastic deformations P_y to an estimate of the mean pressure beneath the indenter (p_m) by utilizing the Hertzian analysis of spherical contact:

$$p_m = P/\pi\alpha^2 \tag{4.5}$$

where α is the contact radius that relates geometrically to the contact depth (h_c) and indenter radius (R) through $\alpha = \sqrt{(2Rh_c - h_c^2)}$. Within elasticity the contact depth equals to half of the on-load indentation depth ($h_c = h/2$). The yield pressures calculated from the above analysis range within $9.5-10.5\,\mathrm{GPa}$, close to the yield pressure of silicon suggesting that this phenomenon relates to the yielding of the substrate rather than the film itself; this is consistent with what has been reported in Beake et al. [72]. This phenomenon is further enforced if one calculates the depth where the maximum shear stress occurs (and therefore where plasticity will initiate) which for

the experiments presented above is on the order of $200-300\text{nm}$; this is deeper than the film thickness ($\sim 125\text{nm}$) and therefore within the silicon substrate domain.

After the substrate yields, the film starts bending locally until surface cracks appear, giving rise to a kink in the residual surface profile. The critical load, P_{CL1}, required for this phenomenon to occur appears to slightly reduce when silver is present, with a more notable drop for the case of $\text{DLC:Ag}_{16.8\text{at.\%}}$, probably due to the more compliant behavior of the film by increasing silver accordingly. Nevertheless, as the mode of fracture is highly dependent on the mechanism of crack propagation and not on crack formation , the P_{CL2}, the load required for complete film failure, increases respectively, showing the ability of film to resist further extension of applied load, as the Ag content increases; An exemption observed for $\text{DLC:Ag}_{16.8\text{at.\%}}$ (Figure 4.11(a)). In fact, significant benefits can be gained from a nanotribological perspective as the critical load for fracturing (P_{CL2}) can increase up to $+74\%$ in the case of $\text{DLC:Ag}_{7.8\text{at.\%}}$. Figure 4.10 shows SEM images of the residual traces left on the surface of scratched specimens. As the contact load increases one starts observing plastic deformations on the films followed by cracking and eventually coating failure which includes fracture, debris and delamination. Severe damage can be observed for pure DLC and $\text{DLC:Ag}_{16.8\text{at.\%}}$ initiating early on the scratch distance which correlate with lower critical loads for film failure (P_{CL2}).

Table 4.3 Nanotribological characteristics of DLC and DLC:Ag films.

Material	P_y	P_{CL1}	Deviation from DLC	P_{CL2}	Deviation from DLC	Friction Coefficient
	[mN]	[mN]	[%]	[mN]	[%]	[-]
DLC	10.8±0.7	51.5±7.8	0	145.4±11.3	0	0.119±0.001
DLC:Ag$_{0.6at\%}$	9.2±1.1	44.8±10.4	-13	149.1±14.6	+3	0.118±0.001
DLC:Ag$_{3.4at\%}$	6.3±0.4	44.0±6.4	-15	198.2±22.3	+36	0.118±0.001
DLC:Ag$_{7.8at\%}$	6.2±0.4	45.7±7.1	-11	253.4±30.4	+74	0.122±0.001
DLC:Ag$_{16.8at\%}$	4.4±1.9	28.8±8.7	-44	127.9±18.9	-12	0.143±0.003

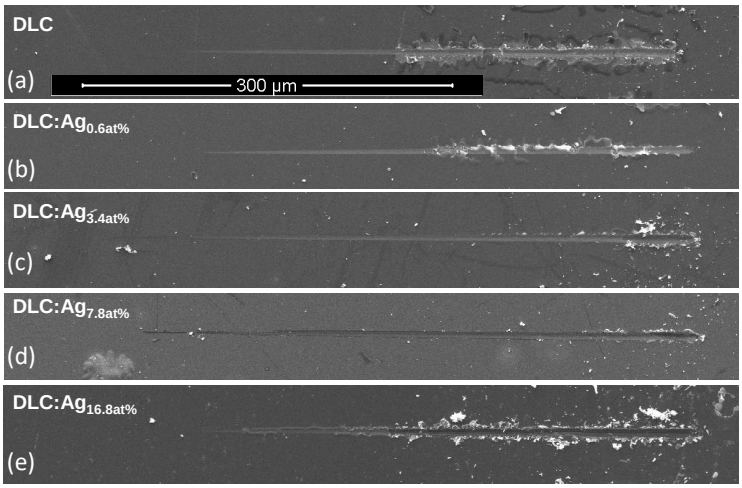

Figure 4.10 SEM images of residual scratched surfaces for the (a) DLC, (b) DLC:$Ag_{0.6at.\%}$, (c) DLC:$Ag_{3.4at.\%}$, (d) DLC:$Ag_{7.8at.\%}$, and (e) DLC:$Ag_{16.8at.\%}$.

From a qualitative point of view film failure/delamination during scratch occurs when the combined action of external and internal stresses surpasses the intrinsic adhesive strength generated between the film and the substrate. External stresses refer to the mechanical stresses generated during the probing with the indenter, whereas internal stresses relate to the cumulative effect of residual compressive stresses trapped within the material during deposition (i.e. through ion subplantation) and the interface stresses generated through substrate/coating lattice misfits. For a more detailed exposition of adhesion and stresses in hard carbon films one is referred to Ref. [136]. In general, the chemical bonding (adhesion) generated between carbon and silicon is very good ($C-Si$ bond energy is about 3.2 eV) producing a strong chemical interface, while the interface stress generated due to atomic mismatch is minimal [136]. The residual compressive stresses that contribute towards film delamination have been calculated through the Stoney formula and are presented in Figure 4.12. It is evident that the incorporation of silver is associated with a reduction in the internal stresses, consistent with previous reports on DLC: Ag systems [5,18]. For DLC: $Ag_{0.6at.\%}$ the stress reduction is on the order of -5% reaching values of -55% as the silver content increases to 3.4 at. % stabilizing thereafter. The graphitization of the matrix in conjunction with the incorporation of the softer Ag phase domains allow for stress relaxation within the DLC: Ag composite. It is interesting to note, however, that the drop in internal stress (Figure 4.12) follows the same trend as the graphitization of the matrix (Figure 4.6) suggesting that the effect of Ag on internal stress reduction is primarily indirect through

the matrix graphitization and the incorporation of the softer phase plays only a secondary role. In any case, internal stress reduction makes DLC: Ag films less susceptible to scratch failure, buckling and delamination.

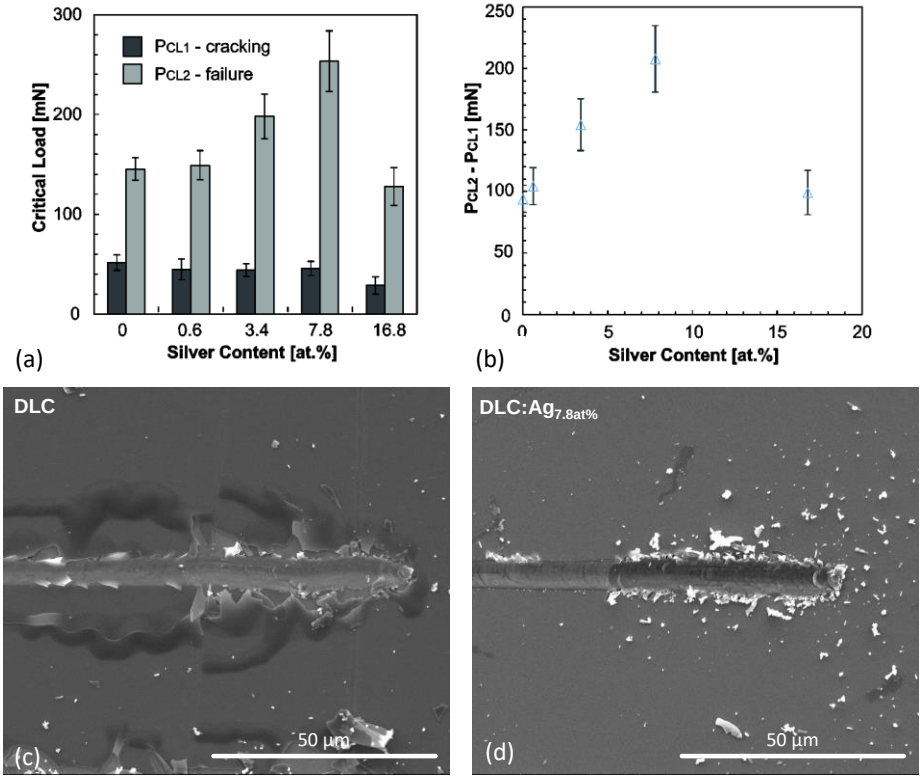

Figure 4.11 (a) Critical scratch loads for cracking (P_{CL1})and fracture (P_{CL2})as a function of silver content. (b) Ductility index for the various silver concentrations. SEM images of the fractured surfaces for (c) DLC and (d) DLC:$Ag_{7.8at.\%}$.

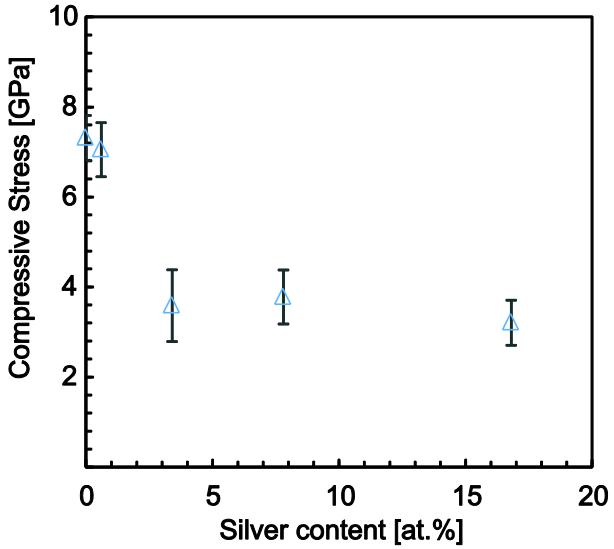

Figure 4.12 Residual compressive stress as a function of silver content.

Beyond residual stress reductions, the enhanced tribomechanical response can be related in part to the increased ductility and amplified fracture toughness of the material generated by the graphitization of the amorphous carbon matrix and the enhancements caused by its composite nature. For high silver doping levels, it seems that these positive effects are eliminated and in fact can even be detrimental for the overall tribomechanical response. These enhancements can be visually observed when looking at the residual imprints left on the scratched surfaces (Figure 4.10). Several metrics have been proposed to quantify the ductility and toughness of the material, one being the plastic work ratio discussed in Section 4.2.2, which quantifies the ability of the material to dissipate energy during indentation. The ability of the material to withstand additional loads beyond cracking, commonly referred to as toughness, can be quantified through the load difference $P_{CL2} - P_{CL1}$ [72,137]. The evolution of this ductility/toughness measure is shown schematically in Figure 4.11(b). The enhancement of the films durability with silver content is evident and in line with our previous observations; nevertheless, a reversed response is observed when the doping levels exceeds a critical quantity returning the toughness to levels equal to those exhibited by the undoped DLC. In fact, DLC:Ag films change their mode of failure from brittle compressive spallation occurring ahead of the tip with severe delamination and micron scale debris into more ductile Hertzian-type of fractures around the circular contact area of the probe with sub-micron debris, as evidenced by the SEM images shown in Figures 4.11(c) and 4.12(d). The negative effects observed at high doping levels could be

attributed to the fact that the $sp^2\%$ becomes dominant at high $Ag\,at.\%$ ($sp^2 > 50\ \%$) which tends to graphitize the carbon matrix converting it into a layered structure. Furthermore, as the silver content increases the $sp^2\%$ content approaches the critical volume fraction for a percolated network to occur that will result in a continuous and weaker path for premature failure.

Finally, a comment is due on the friction coefficient of the deposited films. The values reported in Table 4.3 correspond to the friction coefficients that have been calculated in the steady state zone, i.e. the region between P_{CL1} and P_{CL2} (see Figure 4.2(c)). It is an average value among the coefficients of friction calculated for all the loads in between P_{CL1} and P_{CL2} and for all five scratch repetitions that have been performed for each specimen. The steady state friction coefficient (μ) of the pure DLC is low, $\mu = 0.119$, in line with the atomic scale roughness (Figure 4.2) and literature friction values [15,138]. The $DLC:Ag$ nanocomposite films retain their high smoothness and low friction coefficient with the exception of $DLC:Ag_{16.8at.\%}$ which shows both an increased roughness and friction coefficient. The very origin of DLC lubricity can be traced to the transfer layer that is generated between the DLC films and the sharp counterface material, created during dynamic sliding by the alteration of the very top layers of the DLC films (assuming an ordered layer something similar to graphene sheets in crystalline graphite). Subsequently, all films provide low friction coefficients down to the 0.1 range, with minor discrepancies that can be attributed to the increase of the roughness property which acts as an additional component for the increase of the friction force [49,50].

4.4 Chapter summary

Nanocomposite $DLC:Ag$ films have been synthesized using pulsed excimer laser deposition and studied microstructurally and nanomechanically. It is concluded that:

- Excimer pulsed laser deposition from sector targets can yield $DLC:Ag$ nanocomposites with sub-nanometer scale roughness. Silver atoms self-assemble into nanoparticles due to the poor wetting interaction with the amorphous carbon matrix.
- Silver graphitizes the amorphous carbon matrix with subsequent implications on the elastic modulus and hardness of the material; both scale inversely with

Ag at. %. Nevertheless, this softening response is associated with an increase in the ductility of the material and its scratch resistance as quantified through the scratch load required to fracture the film.

- Introduction of silver at moderate contents (~ 8 at. %) can significantly enhance the tribological characteristics of the film (on the order of $+70\%$ for the critical load to film failure) while retaining the atomic scale roughness and very low friction coefficient characteristics ($\mu = 0.12$). Film delamination through buckling is suppressed which can be attributed to the reduced elastic modulus of the material and the reduction in the residual stresses.
- High silver doping levels on the order of ~ 17 at. % can cause counter effects on the roughness, friction coefficient and overall nanomechanical and nanotribological response of the DLC: Ag films.

While this material system exhibits promising results its use for protective, anti-corrosion, anti-scratch or other coating applications requires further optimization which should consider issues like chemical stability, diffusion barrier characteristics, etc. [136].

CHAPTER 5 Microstructure and nanomechanical properties of pulsed laser deposited DLC:Mo films[2]

5.1 Introductory remarks

In Chapter 4 [139] silver has been used as a DLC-doping agent, developing in the process a nanocomposite film with an enhanced nanotribological response. Within this chapter we use the same deposition method, pulsed excimer laser deposition, for developing DLC: Mo films with various molybdenum contents. Molybdenum has been chosen due to its ability to form carbides, that could potentially enhance the toughness of the material, and also due to its biocompatible and antibacterial nature [140] that can potentially enable applications of DLC: Mo films in biomedical implants or medical tools. Synthesis of DLC: Mo has been reported in the literature in several publications using reactive magnetron sputtering [10,141,142], electron cyclotron resonance chemical vapor deposition [143–145], ion source assisted cathodic arc ion-plating [146], and RF plasma-enhanced CVD [147,148]. Pulsed laser deposited DLC: Mo films, which have the ability of retaining the target stoichiometry and therefore developing hydrogen-free DLC films when high-purity graphite targets are used, have not been investigated to the same extent and will be the focus of this study. While the presence of hydrogen can reduce the coefficient of friction (COF) of the films (< 0.1) their mechanical characteristics, in particular the hardness and elastic modulus are also reduced [11,149]. Even more significant is the reduction in the wear resistance with rates reaching values several orders of magnitude lower than their non-hydrogenated DLC counterparts [150].

The objective of this study is twofold: (a) to synthesize and microstructurally characterize pulsed laser deposited DLC: Mo films with various molybdenum contents, and (b) quantify the effect of molybdenum on the nanotribological response of DLC: Mo

[2] Results presented in this chapter have been published in the following paper: M. Constantinou, M. Pervolaraki, L. Koutsokeras, C. Prouskas, P. Patsalas, P. C. Kelires, J. Giapintzakis, G. Constantinides 'Enhancing the nanoscratch resistance of pulsed laser deposited DLC films through molybdenum-doping' Surface and Coatings Technology, 330, 185-195, 2017.

films, in particular the critical load to film failure. Structure-property relations will be generated through the investigation of both microstructure and nanomechanics/nanotribology.

5.2 Materials and methods

5.2.1 Deposition and characterization of DLC:Mo films

In depositing DLC and DLC: Mo films, high purity sectorial targets of Graphite (G) with Molybdenum (Mo) were ablated with a KrF laser (COHERENT COMPex Pro 201) operating at 248 nm, with pulse-width of 25 ns at FWHM. Films with molybdenum compositions up to 3.2 at. % have been synthesized; their elemental concentration and carbon hybridization states were probed using X-ray photoelectron spectra (SPECS GmbH equipped with HSA-Phoibos 100 analyzer). Film thicknesses of 125 ± 5 nm were measured by a surface profiler and scanning electron microscopy (SEM); these values were confirmed through X-ray reflectivity (XRR) measurements performed in an Ultima IV Rigaku diffractometer with Cu anode in line focus geometry and operated at 40kV and 40mA, the optical setup of which consists of a multilayer mirror, an eulerean cradle rotation sample stage, incident and receiving slits and a scintillator detector. No knife edge was used to block incident direct beam. Surface roughness was calculated from $3\ \mu m \times 3\ \mu m$ atomic force microscopy images collected with a commercial scanning probe microscope system (Ntegra Prima, NT-MDT). Residual compressive stresses generated within the films during deposition were quantified through curvature measurements (κ) of the film/substrate system using optical profilometry and the use of Stoney formula:

$$\sigma_f = \frac{E_s t_s^2 \kappa}{6 t_f (1 - \nu_s)} \tag{5.1}$$

where $\mathbf{E_s}$ and $\boldsymbol{\nu_s}$ are the elastic modulus and Poisson's ratio of the substrate and $\mathbf{t_s}$, $\mathbf{t_f}$ are the substrate and film thickness respectively. Nanoindentation (multi-depth indentations) and nanoscratch tests were performed with a Micro Materials NanoTest, while the topographical and fracture characteristics of the tested films were investigated using **SEM** (Quanta 200, FEI) imaging. The methodology for producing and

characterizing these films has been described in detail in the materials and methods section of Chapter 4 (Sections 4.2.1 – 4.2.4).

5.3 Results and discussion

5.3.1 Effect of Mo-doping on microstructure

Fig. 5.1(a) shows a cross-sectional SEM micrograph of the deposited molybdenum-doped amorphous carbon film where the nanometer thickness film and the silicon substrate can be visualized. Energy dispersive X-ray spectra (EDS) at two different locations confirm the presence of the deposited molybdenum-doped amorphous carbon film. A delaminated/fracture area can be observed at the right hand side of the image from which the thickness can be estimated at approximately $\sim 120 nm$. More accurate measurements of the film thickness were obtained through atomic force microscopy images. Fig. 5.1(b) shows a 3-dimensional image of an artificial step where the film/substrate geometrical arrangement is evident by the sudden drop in depth, separating the region where film is present and where is absent. A two-dimensional cross-section (Fig. 5.1(c)) provides easy and accurate measurement of the film thickness which for this particular case of DLC: $\mathrm{Mo}_{3.2\mathrm{at.\%}}$ is measured at 120 nm.

The density and thickness of DLC, the host matrix for all DLC: Mo films deposited for the purposes of this study, were measured using XRR. During such an experiment the critical angle for which the X-rays are totally reflected can be related to the density of the material whereas the interference of the waves reflected from the film-substrate interface causes oscillations, the period of which provides access to the film thickness. Fig. 5.2 shows the experimental and best fitted model data on pure DLC in which the film characteristics (density, thickness, roughness) were varied until the discrepancy between experimental data and simulation results is minimized. A two layer model was used for this fitting and the resulting values were a film thickness of 122 nm and a film density of $2.9\ \mathrm{g/cm^3}$. The density value obtained herein suggests a high $\mathrm{sp^3}$ content ($70 - 80\ \mathrm{at.\%}$) amorphous carbon matrix [105]; this is confirmed below using XPS measurements. The film thickness obtained with this technique was consistent with optical profilometry and atomic force microscopy measurements on artificial steps (e.g., Fig. 5.1(c)); film thickness was found to be insensitive to the chemical composition, with values for all DLC: Mo films in the 125 ± 5 nm range.

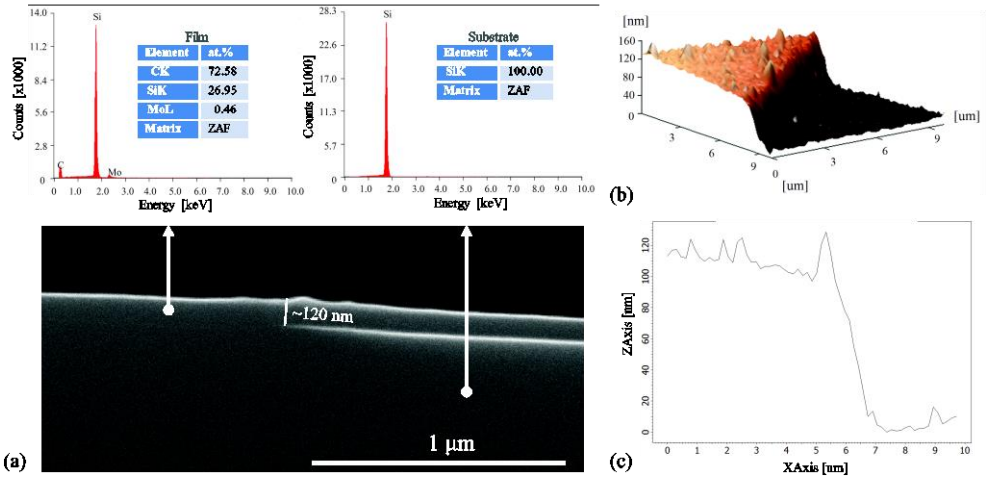

Figure 5.1 (a) Cross-sectional SEM micrograph with EDS measurements on two spots. (b) Three-dimensional view of an AFM image collected on an artificial step showing film-substrate transition. (c) Line section on the artificial step.

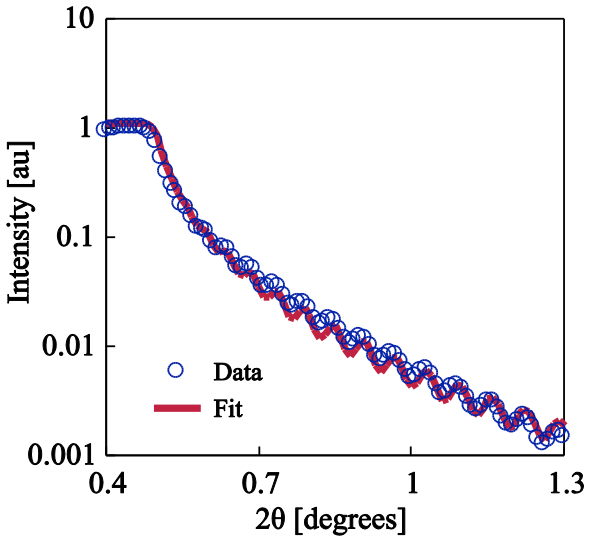

Figure 5.2 X-ray reflectivity curves on DLC film; circles indicate experimental data whereas the red line shows the two-layer simulations results for the optimized parameters.

Fig. 5.3 shows SEM and AFM images of the pulsed laser deposited DLC and DLC: $Mo_{1.9at.\%}$ films providing topographical details at two different length scales: the micrometer and nanometer length scale. The SEM images (Fig. 5.3 (a)) deliver a micrometer scale view of the deposited material testifying towards the smooth and uniform surface finish of the PLD films. Several isolated particles can be sporadically identified on the DLC: Mo film surfaces, nevertheless they constitute only a minor fraction of the total surface area. A magnified view of a particle is shown in the inset of Fig. 5.3(a) and relates to a fragment of graphite or molybdenum targets ejected due to

melting of the surface; particles with near spherical shape are cooled during their flight towards the substrate and the shape is retained with collision. The topographical characteristics of the resulting DLC and DLC: $Mo_{1.9at.\%}$ films are shown through atomic force microscopy images covering an area of $3\mu m \times 3\mu m$ in Fig. 5.3(b) and Fig. 5.3(c), respectively. It is apparent that the pulsed laser deposition process results in films with atomic scale roughness; pure DLC has a roughness of 0.11 ± 0.03 nm in accord with literature data [114,115,139]. Table 5.1 summarizes the surface roughness of all deposited films: it is evident that molybdenum doping does not significantly affect the film's surface characteristics, at least for the range of contents examined herein, gradually shifting their RMS roughness values into the $0.20 - 0.25$ nm, retaining however their atomic scale smoothness.

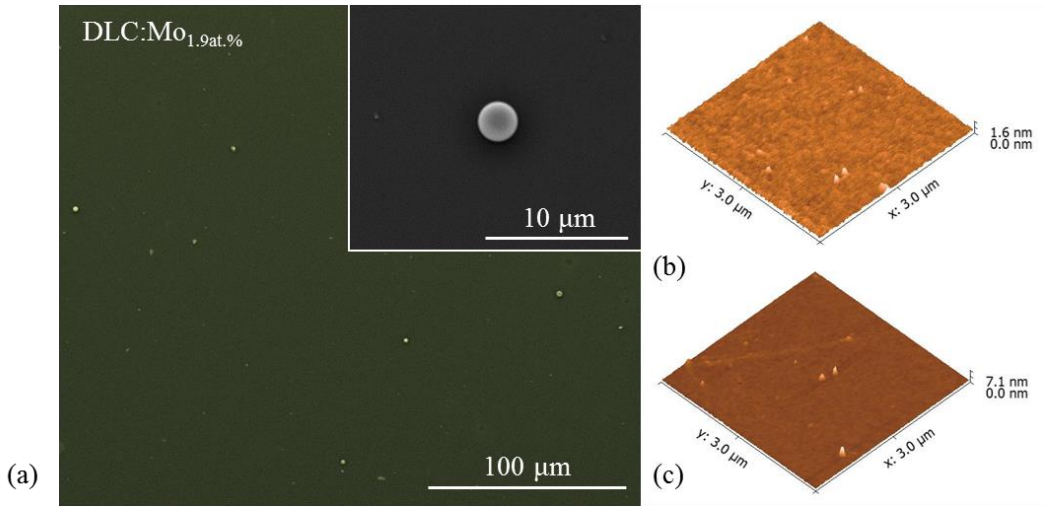

Figure 5.3 (a) SEM images of DLC:$Mo_{1.9at.\%}$ film; inset shows a magnification of a droplet occasionally found on the surface. Corresponding 3μm x 3μm AFM images of (b) DLC and (c) DLC:$Mo_{1.9at.\%}$.

The atomic bonding structure of the films was probed using XPS. The C1s spectrums for all DLC and DLC: Mo films are plotted in Fig. 5.4. In general, the C1s peak is very sensitive to the sp^2 and sp^3 contents in $a-C$ [116] and $a-C$: Me nanocomposites [117]. In fact, precise atomic percentages can be obtained by decomposing the spectra to several contributions: $C-C$ bonds in sp^2 configuration at 284.6 eV, $C-C$ bonds in sp^3 configuration at 285.5 eV, and $C-O$ due to adventitious carbon at 286.4 eV [116,117]. In the case of DLC: Mo films it was necessary to add a $Mo-C$ contribution at 282.8 eV in order to capture the rise in the right tail of the C1s peak, which was growing in importance as the Mo-content was increasing. In fact the systematic rise in

the low eV tail testifies towards the existence of $Mo-C$ bonds, the percentage of which increases as the molybdenum content increases (Table 5.1). Examples of C1s deconvolutions for the two extreme doping cases are shown in Fig. 5.5. Molybdenum concentration was quantified using the intensities of $Mo3d_{5/2}$ / $Mo3d_{3/2}$ XPS peaks located at 228.0 eV / 231.1 eV, respectively. The sp^3, Mo and $Mo-C$ atomic percentages are summarized in Table 5.1.

Table 5.1 RMS roughness, molybdenum content, sp^3 percentage, and Mo-C percentage of the pulsed laser deposited DLC:Mo films.

Material	Roughness [nm]	Mo [at.%]	sp^3 [at.%]	Mo-C [at.%]
DLC	0.11 ± 0.03	0	77.1	0.0
DLC:$Mo_{0.3at\%}$	0.12 ± 0.07	0.3	61.3	0.9
DLC:$Mo_{0.5at\%}$	0.15 ± 0.08	0.5	61.7	1.6
DLC:$Mo_{1.9at\%}$	0.21 ± 0.10	1.9	50.0	2.6
DLC:$Mo_{3.2at\%}$	0.24 ± 0.08	3.2	34.9	5.3

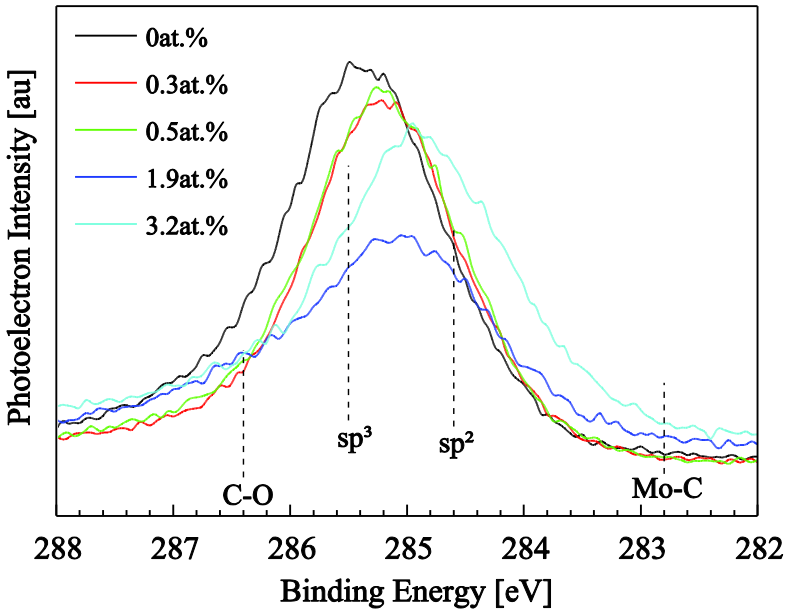

Figure 5.4 C1s peaks from the XPS spectra of the pure and molybdenum-doped deposited films.

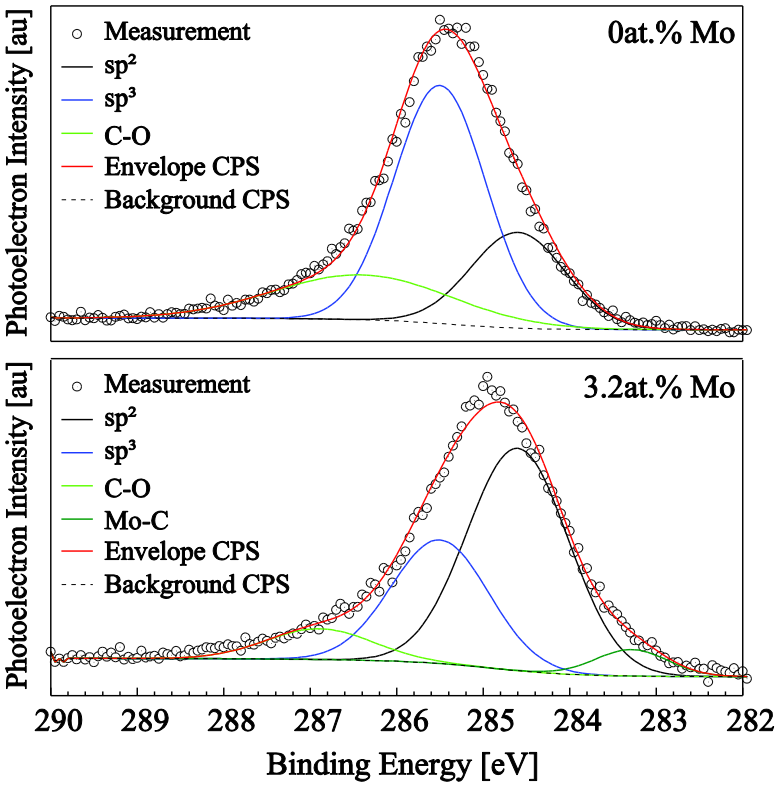

Figure 5.5 Individual contributions of atomic type of bonding on the C1s spectra for DLC and DLC:Mo$_{3.2at.\%}$.

It can be clearly identified from the data presented in Table 5.1 that the addition of molybdenum into the amorphous carbon system induces a gradual graphitization of the matrix. This observation is in line with theoretical atomistic simulations and experimental data [102,151]. The metallic surface leads to carbon-carbon bond destruction and promotes the sp^2 hybridization state. This graphitization process is graphically depicted in Fig. 5.6(a) where the relative difference in the sp^3 atomic percentage (compared to pure DLC) with metal content is plotted for various amorphous carbon metallic nanocomposites systems reported in the literature that were either simulated or experimentally measured. It can be generally concluded that the incorporation of transition metal nanoparticles into amorphous carbon rapidly graphitizes the matrix at a rate of $\sim$10 at. % of sp^3-reduction for every 1 at. % of metal. The scattered observed in Fig. 5.6(a) can be attributed to the size and dispersion of metallic atoms/clusters/particles, parameters that are expected to affect the available surface interaction with neighboring atoms and thus the extent of graphitization. Nevertheless, as evidenced by Fig. 5.6(a), the effect of the particular metal type and size/shape is of secondary importance and it is the atomic percentage that primarily

dominates the response. In the case of doping with the carbide-forming metal of molybdenum, however, this graphitization process is also accompanied by the formation of Mo – C bonds, their atomic percentage of which appears to scale with the Mo-content (Fig. 5.6(b)).

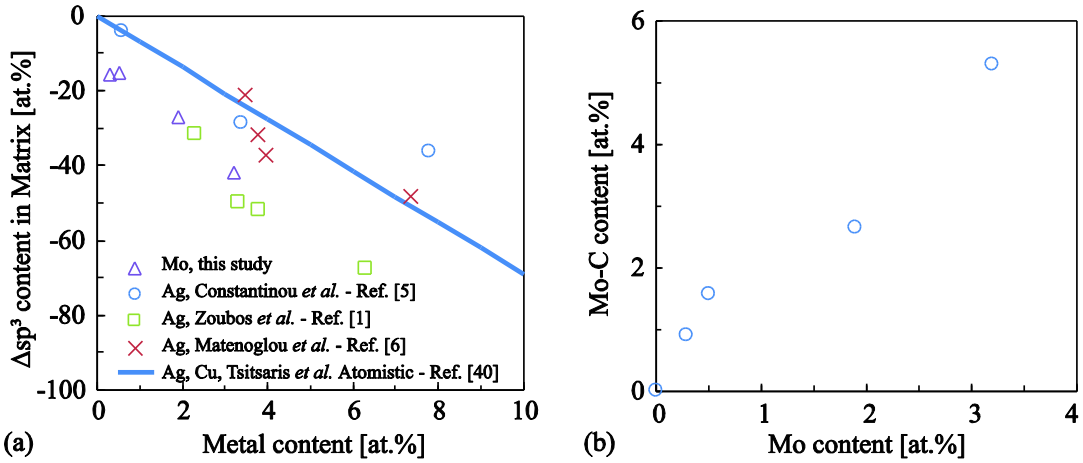

Figure 5.6 (a) Amorphous carbon matrix sp^3 content drop for different metal contents. Literature experimental data: Constantinou et al. [139]**, Zoubos et al.** [105]**, Matenoglou et al.** [102]**. Literature atomistic simulations: Tritsaris et al.** [151]**. (b) Atomic percentage of molybdenum-carbon bonds for various molybdenum contents.**

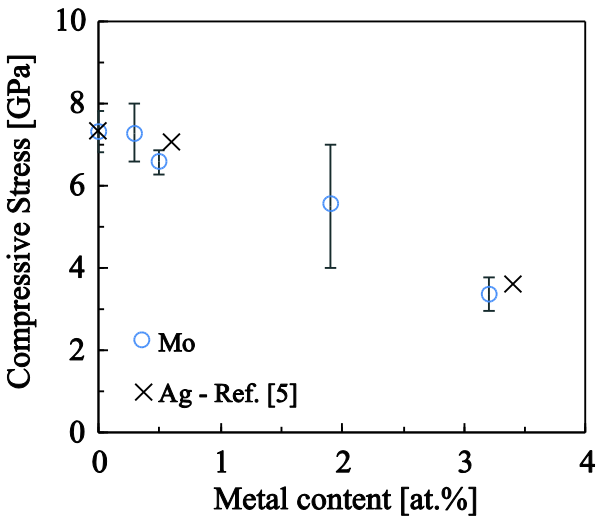

Figure 5.7 Compressive stress state for the various molybdenum contents considered in this study. Results for DLC:Ag from Ref. [139] **are also included for comparison.**

We also note that grazing incidence X-ray diffraction measurements were performed on all specimens but did not show any peaks, and were therefore not included herein. The absence of X-ray peaks is not necessarily linked to the absence of a crystalline

molybdenum or molybdenum carbide phase but could be related to the small size and percentage content of the molybdenum-related domains that make them non-detectable in such small sizes/proportions with XRD.

Residual compressive stresses calculated through curvature measurements and the use of Eq. 5.1 are presented in Fig. 5.7. The high initial compressive stress ($\sim$8GPa) that existed in the case of pure DLC related to the high energy carbon species that were generated during the ablation process, accelerated towards the substrate material and "subplanted" into sp^3 configurations; this resulted in an increased atom density, bond distortion and subsequent residual compressive stress build-up. It is evident from Fig. 5.7 that the introduction of molybdenum into the system reduced the compressive stress reaching values close to 3GPa for 3.2at.% of Mo. While the relief of this residual compressive stress has been experimentally observed for a series of metal-dopants the actual theoretical explanation for this mechanism was recently presented in a series of first-principle studies [152–154] in which the chemical bond structure of the metal-doped carbon systems has been investigated. Choi et al [152] studied the atomic bond characteristics between carbon and metal atoms (Mo, Ag, Al) using first-principle calculations and the tetrahedron bond model. They classified the bond characteristics between Mo and C as nonbonding, which reduces bond directionality and strength. Li et al [153] has expanded the investigation into a larger number of elements using first principle calculations (the tetrahedral cluster model). They concluded that when transition metals are used as dopants in amorphous carbon the highest occupied molecular orbital (HOMO) changed from bonding (i.e., Ti, Zr, Hf) to nonbonding (i.e., V, Nb, Ta, Cr, Mo, W) to antibonding (i.e., Co, Ni, Pd, Pt, Cu, Ag, Au) as d electrons increased. The bond characteristics coupled with the electronegative difference between Me and C reduced bond strength and directionality, which in terms explains the smaller energy changes induced by distortion of bond structure. This subsequently explains the reduction in residual compressive stresses achieved when transition metals are used as dopants within $a-C$ matrices. Li et al [154] performed more detailed *ab initio* molecular dynamics simulations in an attempt to probe the stress-reduction mechanism reported in DLC-films doped with carbide-forming metals. They concentrated on the case of Ti, Cr and W and their simulations revealed that at small atomic percentages (the percentage differs for each metal) the compressive residual stress significantly reduced.

The stress-reduction mechanism has been identified as the relaxation of both bond-distortions and bond-lengths which was possible due to presence of the less strong and directional $Me-C$ bonds that were introduced in the system. Our results are therefore consistent with these theoretical explanations, that at small metal contents the introduction of $Mo-C$ into the system coupled with the graphitization of the amorphous carbon matrix reduced the compressive residual stress. The bond strength and directionality between $Ag-C$ and $Mo-C$ is not significantly different to justify diversion between the two curves. Finally, the release of residual stress is expected to favor films stability by minimizing the internal stresses that might lead to premature failure; this is expected to increase the stress capacity of the system and will be further investigated next.

5.3.2 Effect of Mo-doping on the nanomechanical response

Multi-depth indentations were performed on the deposited films such as to account for the substrate contribution on the overall mechanical response. More precisely, 20 indentations at increasing loads/depths were executed in order to quantify the depth dependency on hardness, $H = f(h_c)$, where h_c is the contact depth at a given load, estimated through the Oliver and Pharr method [69]. Figure 5.8(a) shows the evolution of hardness with h_c/t. As anticipated, the measured hardness approaches the value of the substrate material (here silicon) for large indentation depths [79,125]. As the h_c/t reduces the measured hardness increases reaching a maximum at around $h_c/t = 0.2$. For even smaller indentation depths we observe a decrease in the mechanical response which relates to the non-ideal sharp geometry of the probe [100] at the very edge which gives rise to a gradual transition from elasticity to elastoplasticity. This upward tendency of hardness at small indentation depths can be fitted to a mechanical model that will help eliminate the contribution of the substrate and obtain film only parameters [126]. The multi-depth data on the DLC and $DLC:Mo$ films were fitted to the analytical model proposed by Bhattacharya and Nix in Ref. [82] and the intrinsic hardness was calculated through equation 4.4 (see also section 4.3.3 for further discussion on fitting parameters).

The measured average hardness properties from 20 different depths for the case of the DLC: $Mo_{0.3at.\%}$, as well as, the effect of molybdenum content on the DLC: Mo films response is summarized in Figure 5.8. It is evident that the pure DLC shows the maximum hardness (23.7 ± 1.7 GPa), which is very close to the expected hardness data presented in the literature for amorphous carbon materials with similar density and sp^3 percentage [15]. Adding molybdenum into the material system results in a mechanical capacity drop; for the highest molybdenum content tested herein the percentage hardness drop is measured at -30%. This reduction in the ability of the material to resist penetration from the indenter can be related to molybdenum contributions which (a) possesses a lower hardness (measured around $2-4$ GPa [155]) thus acting as a softer nanoinclusion and (b) indirectly leads to matrix softening, through the graphitization process that is induced within amorphous carbon (see Table 5.1 and Figure 5.6(a)).

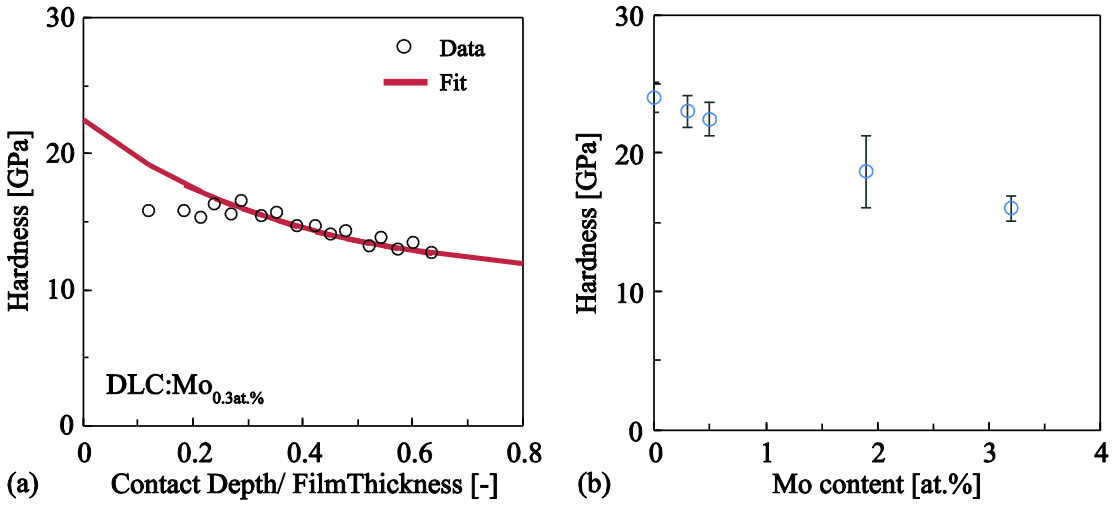

Figure 5.8 (a) Scaling of DLC:Mo $_{0.3at.\%}$ hardness with the normalized contact depth; experimental indentation data and modeling fit using Eq. (2). (b) Effect of molybdenum content on DLC:Mo hardness.

5.3.3 Effect of Mo-doping on the nanotribological response

The nanotribological performance of the deposited films was probed using the same instrumented indentation platform used for nanoindentations but in the scratching mode. In contrast to micrometer level scratch testers, the nanoscratch platform allows for nanoscale-level monitoring of the surface profiles before and after scratch testing. The necessary stresses required to yield and subsequently crack and fail/delaminate the film are achieved through micron scale probe radii that enhance the contact pressure [112]. It

has been demonstrated that scratch speed, loading rate, and loading per unit length do not significantly affect the overall tribological response of films [113,130]. In general the only two parameters that are expected to influence the critical loads that lead to yielding, cracking and subsequently film failure are the geometrical characteristics of the probe (in particular its radius) and the thickness of the film which can change the stress distribution generated through contact [113,131,132]; in order to concentrate on the material properties the film thickness and the probe radius were kept the same for all tests within this investigation. Subsequently, any deviations between the critical loads measured on each deposited film can be attributed to material-related characteristics and not to test-related conditions.

Several metrics can be extracted from such tests, the most important of which relate to the three critical loads that are linked to distinct mechanical responses exhibited by the film/substrate arrangement as the contact load increases [112,135]:

1. P_y is the critical force required to initiate permanent deformations within the film/substrate system and was identified through the onset of plastic deformations that can be observed in the residual surface profile scan
2. P_{CL1} is the critical force required to induce film cracking, commonly manifested by a sudden height change in the residual surface topography
3. P_{CL2} is the critical load that leads to film delamination and failure, spotted either through the significant height change in residual topography or through the discontinuity on the coefficient of friction curve (see for example Figure 5.13(a)).

The three critical loads together with the coefficient of friction (COF) for all DLC: Mo films studied herein are summarized in Table 5.2 and graphically presented in Figure 5.9(a). It can be observed that P_y is inversely related to the molybdenum content. While the incorporation of molybdenum is expected to soften the DLC: Mo composite film, as also evidenced with hardness in Figure 5.8(b), the source of this drop requires a more detailed investigation. Towards this end, one can use P_y in calculating the mean contact pressure beneath the spherical part of the probe through the analytical solution of Hertz (see a more detailed explanation in section 4.3.4 of chapter 4) .

The mean pressures at yield, p_m^y, quantified using Equation (4.5) for $P = P_y$, appear to remain more or less constant at $9.5 - 10.5$ GPa. This value (a) does not scale with

molybdenum content, (b) is much lower than the measured hardness values of DLC and DLC: Mo films and (c) is similar in magnitude to the hardness of silicon. Furthermore, the maximum shear stress which is the critical parameter that will initiate plastic deformations is calculated at a depth of $200 - 300\text{nm}$, which is higher than t. All of the above suggest that the macroscopic plasticity onset detected by P_y is driven by the plastic response of the silicon substrate. This observation is in agreement with the conclusions of Beake *et al* [72] that reported scratch tests on tetrahedral amorphous carbon films with thicknesses in the $5 - 150\text{nm}$ range and the experiments of Constantinou *et al* [139] that reported scratch tests on $\sim 125\text{nm}$ DLC: Ag films with various silver contents.

The critical load to initiate cracking, P_{CL1}, is not significantly affected by the doping content. In fact, the range of reported values for all DLC: Mo films ($45.4 - 60.4\text{mN}$) is within $\pm 15\%$ to the critical load for cracking measured in the case of pure DLC (51.5mN), which does not significantly deviate from the standard deviations reported for all films ($4 - 13\%$). Given the fact that after substrate yielding the film starts bending which eventually leads to local cracking, it is not surprising that the doping level does not play a pivotal role in the process. In contrast, the critical load that leads to complete film failure, P_{CL2}, scales with the Mo content (Figure 59(a)). More precisely, the nanoscratch capacity of the DLC: $Mo_{3.2at.\%}$ film is enhanced by $+87\%$ compared to the pure DLC film. This is also evident from the scan electron microscopy investigation presented in Figure 5.10. The gradual increase of the contact load to the maximum target value of 350mN sequentially leads to plastic deformations, microcracking and film fracture/delamination. While severe brittle damage is observed for pure DLC, the failure mode becomes more ductile as the molybdenum content increases, a phenomenon which is directly linked with higher P_{CL2}.

Table 5.2 Nanotribological metrics for all DLC and DLC:Mo films studied herein.

Material	P_y	P_{CL1}	P_{CL2}	Deviation from DLC	COF
	[mN]	[mN]	[mN]	[%]	[-]
DLC	10.8±0.7	51.5±7.8	145.4±11.3	0	0.118±0.001
DLC:Mo$_{0.3at\%}$	9.0±0.9	48.3±4.2	182.0±16.5	+25	0.114±0.001
DLC:Mo$_{0.5at\%}$	6.8±0.6	45.4±5.5	179.4±23.1	+23	0.117±0.003
DLC:Mo$_{1.9at\%}$	6.2±0.6	60.4±11.1	213.0±47.3	+46	0.123±0.003
DLC:Mo$_{3.2at\%}$	6.4±0.7	56.8±13.2	272.6±39.5	+87	0.132±0.003

Film failure and delamination during scratch loading is expected when the film stress, which includes the contribution of the external loading and internal stresses that pre-exist in the film, exceeds the film-substrate adhesive strength. When referring to internal stresses we account for both the residual compressive stresses generated during the deposition process and the interface stresses that result from the film/substrate lattice misfits [136]. With this perspective in mind, enhancements in the scratch resistance of films can originate from various sources. In our case the enhancements observed in the critical load to failure of the molybdenum-doped films can be traced (a) to the molybdenum-driven graphitization of the matrix that leads to a softer but more ductile, (b) to the increasing percentage of $\mathrm{Mo}-\mathrm{C}$ bonds produced due to doping that enhances the materials toughness, and (c) the reduction on residual stresses as evidenced in Figure 5.7; the interface stresses due to lattice mismatch between Carbon and Silicon are expected to be negligible [136]. These enhancements can be noted at the measured critical loads for failure reported in Table 5.2 and Figure 5.9(a) but also evidenced from post-scratch scan electron microscopy images (Figure 5.10 and Figure 5.11). The post-cracking performance of materials is of great importance and signifies the ability of film to retain structural integrity until complete failure. This property relates to the toughness of the material and in scratch tests it may be examined using the index $\mathrm{P_{CL2}}-\mathrm{P_{CL1}}$ [72,137]. The effect of molybdenum content on this toughness index is graphically represented in Figure 5.9(b). The significant enhancements induced by molybdenum doping are clearly evident and consistent with previous observations for other metal-doped DLC films. What is even more important, however, is the superior reinforcement to DLC provided by molybdenum in comparison with silver, the data of which has been reported in Ref. [139]. Given the fact that the residual stress relaxation induced by

metal-doping is similar for both silver and molybdenum, the enhanced tribological response of DLC: Mo films can be linked to the metal-C bonds that are favored in the case of molybdenum (Figure 5.6(b)). It appears that $\mathrm{Mo}-\mathrm{C}$ bonds provided additional resistance to microcracking that resulted in an enhanced toughness as quantified through the $\mathrm{P_{CL2}}-\mathrm{P_{CL1}}$ difference. In fact the $\mathrm{P_{CL2}}-\mathrm{P_{CL1}}$ value for the case of DLC: $Mo_{3.2at\%}$ is 40% higher compared to the equivalent DLC: Ag film with a similar metal content. Finally, a significant contribution on the overall nanoscratch resistance comes from the residual stress reduction (Figure 5.7) that can be achieved by the doping procedure [5,18] that increases the stress-capacity of the DLC: Mo films prior to delamination, fracture and failure. SEM images of the whole scratch tracks and magnified SEM images at the end of the scratch tracks, shown in Figure 5.10 and Figure 5.11, respectively suggest that the failure-mode shifts from a brittle-type delamination occurring ahead of the tip with associated micrometer level debris into circular fractures preceding the probe with smaller size film fragments. In an attempt to quantify the efficiency of molybdenum-doping towards the enhancements of the scratch resistance ability of the DLC: Me film we have plotted the critical load to film failure as a function of metal content for three types of metals (Mo [this study], Ag [139], W [156]). We note that while identical testing conditions have been used for Mo and Ag the probe geometry and film thickness for the case of W were different. In order to present the results in a unified manner the critical loads to delamination have been normalized by the critical load required to delaminate the pure DLC that formed the host- matrix in each case. The results, which are presented in Figure 5.12 suggest that the enhancement is more pronounced in the case of carbide-forming elements (Mo and W) in comparison with the non-carbide forming silver. Also comparing the cases of DLC:Mo and DLC:W, one can see better scratched resistance for the case of DLC:Mo due to the lower hardness value of molybdenum element (hardness around 2-4 GPa [155]) compared to tungsten element which has hardness on the order 6 GPa [157]

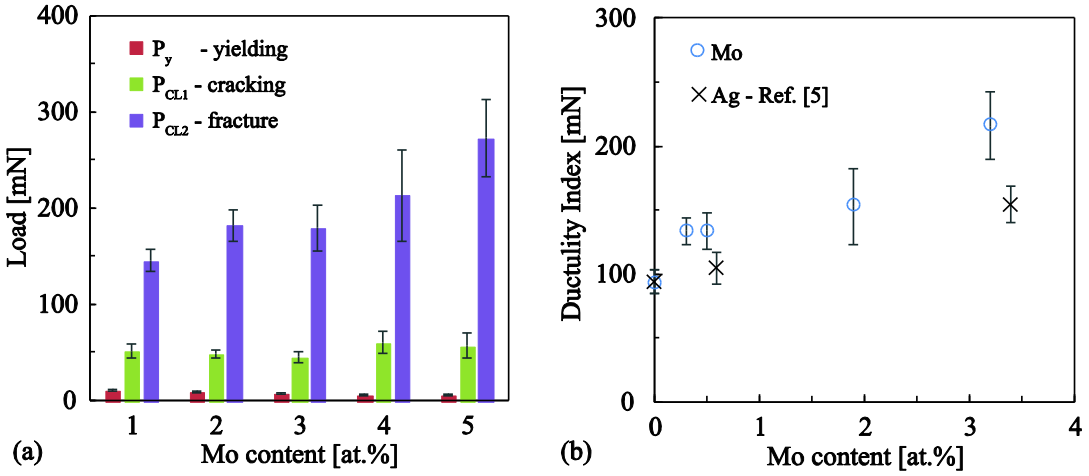

Figure 5.9 (a) Critical loads extracted from nanoscratch tests: yielding (P_y), cracking (P_{CL1}), and fracturing (P_{CL2}). (b) Ductility/Toughness index as a function of molybdenum content. Results for DLC:Ag from Ref. [139] **are also included for comparison.**

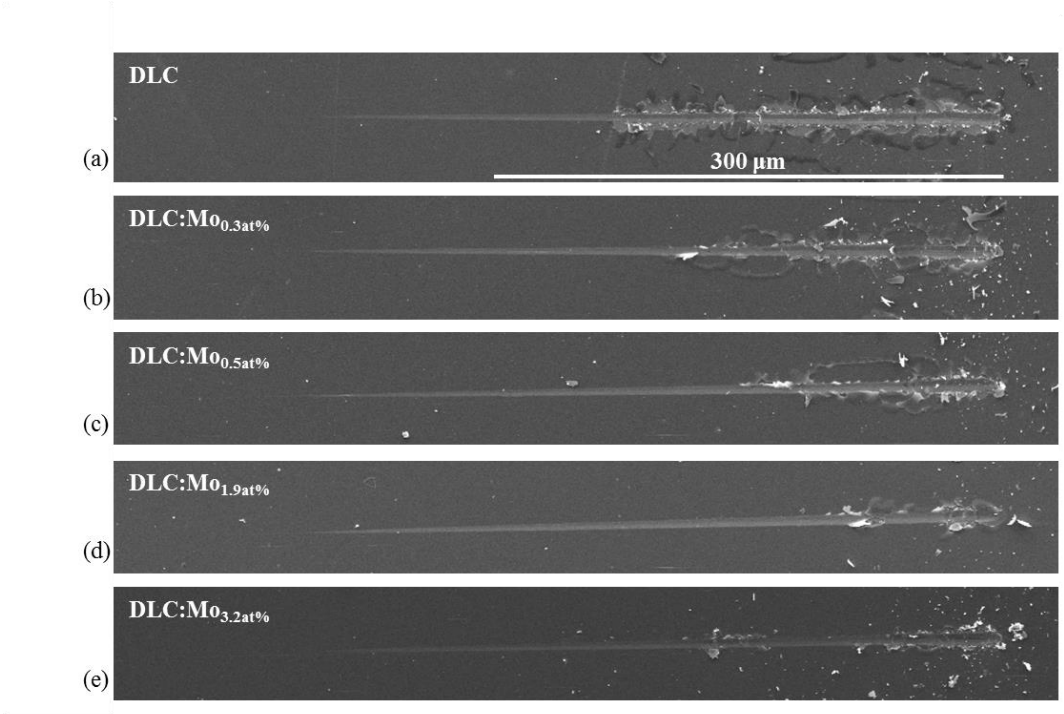

Figure 5.10 Post-nanoscratch scan electron microscopy images for (a) DLC, (b) DLC:$Mo_{0.3at.\%}$, (c) DLC:$Mo_{0.5at.\%}$, (d) DLC:$Mo_{1.9at.\%}$, and (e) DLC:$Mo_{3.2at.\%}$.

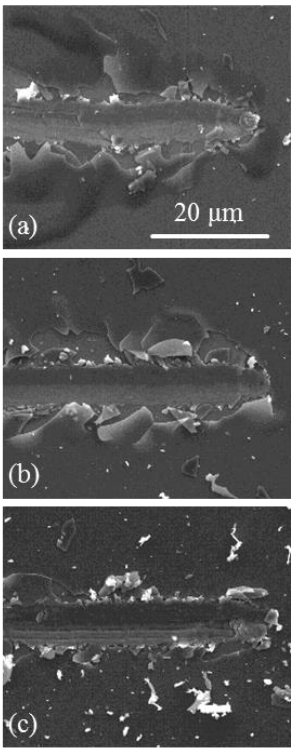

Figure 5.11 Magnified scan electron microscopy images showing the end of the scratch lines post-scratch topography for the (a) DLC, (b) DLC:$Mo_{0.5at.\%}$, and (c) DLC:$Mo_{3.2at.\%}$.

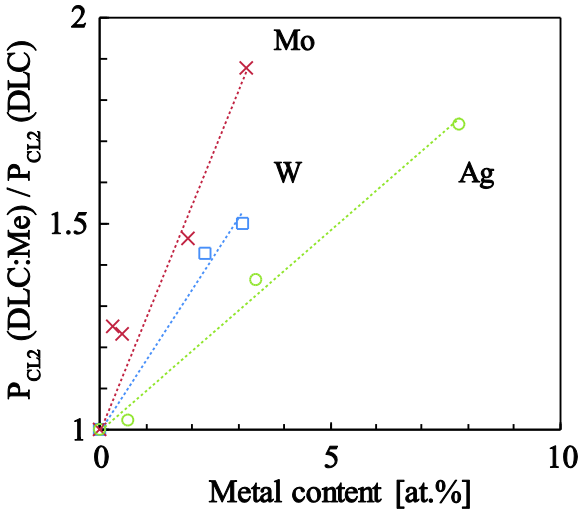

Figure 5.12 Amplification of the critical load for delamination calculated by normalizing the results with the critical load required to fracture the pure DLC matrix (without any doping) as a function of the metal content; results collected herein are contrasted with literature results on Ag [139] **and W** [156]**.**

In closing, the data on coefficient of friction is discussed. Figure 5.13(a) plots the evolution of friction coefficient with the applied normal load for DLC: $Mo_{3.2at.\%}$. The

friction coefficient (μ) is low for small loads and exhibits an upward trend until steady-state conditions are reached when plasticity is fully developed. For the particular material a sudden deviation is observed at $\sim 250\text{mN}$ which coincides with the critical load for film failure and delamination for this particular specimen/test. In reporting a characteristic value for the coefficient of friction an average value is obtained in the normal load range of 0 to 100mN (Figure 5.13(b)). The average values for all specimens are given in Table 5.2 and plotted in Figure 5.14(b). Indicatively, we note that the DLC coefficient of friction is measured at $\mu = 0.118$, which is consistent with the sub-nanometer roughness measured through AFM (Figure 5.3) and amorphous carbon friction coefficient data reported in the literature [15,138]. While a small rise in coefficient of friction with molybdenum content can be observed (approximately $+10\%$), this increase is insignificant and it can be stated that all DLC:Mo films retain their high smoothness and low frictional response. The low COF (< 0.12) exhibited by hydrogen-free DLC films was reported in many publications and was attributed to a friction-induced phase transformation that occurred at the interface between the DLC film and the contacting probe [150,158]. The pressure and shear distribution generated by the contacting bodies induces a relaxation of the sp^3 phase into the layered sp^2 form. These graphite-like formed sp^2 domains can be easily sheared from the surface of the DLC film and adhere onto the surface of the contacting probe generating in the process a lubricious transfer layer with low frictional characteristics (< 0.12) and low wear rates ($\sim 10^{-9}\text{mm}^3\text{N}^{-1}\text{m}^{-1}$). It is, therefore, understandable why DLC:Mo films exhibit similar COF values; the lubricating film will be phase-transformed as contact pressure builds up at the interface, irrespective of the metal content.

The evolution of COF with scratch length is also plotted in Figure 5.14(a) and shows the similar response between DLC and $\text{DLC:Mo}_{3.2\text{at.\%}}$, with the exemption the scratch distance for which film failure occurs. Given the load-controlled nature of the experiment which is linearly ramped with distance travelled, the spatial discrepancy between the location of film failures translates into a different critical applied load, consistent with earlier observations (Figure 5.9(a)). The slight increase in the COF of $\text{DLC:Mo}_{3.2\text{at.\%}}$ can be attributed to (a) the higher roughness exhibited by molybdenum-doped DLC films and (b) the increased adhesion to the substrate and subsequently the

increased shear resistance probably provided by the $Mo-C$ bonds that hinder the unobstructed sliding of the graphite like sp^2 bonds.

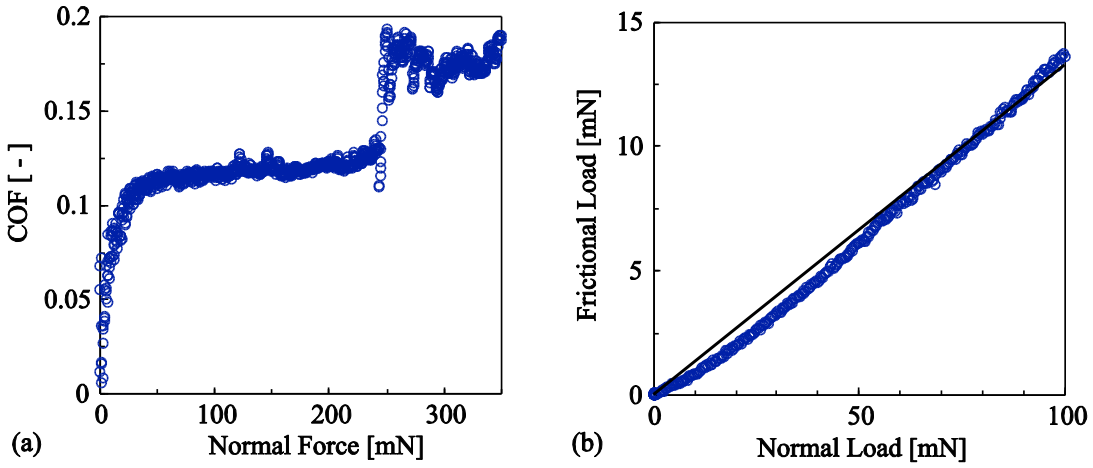

Figure 5.13 (a) Coefficient of friction for various normal loads applied during the scratch test. (b) Frictional load developed for the various applied normal forces in the 0-100mN range. Results are for DLC:$Mo_{3.2at.\%}$.

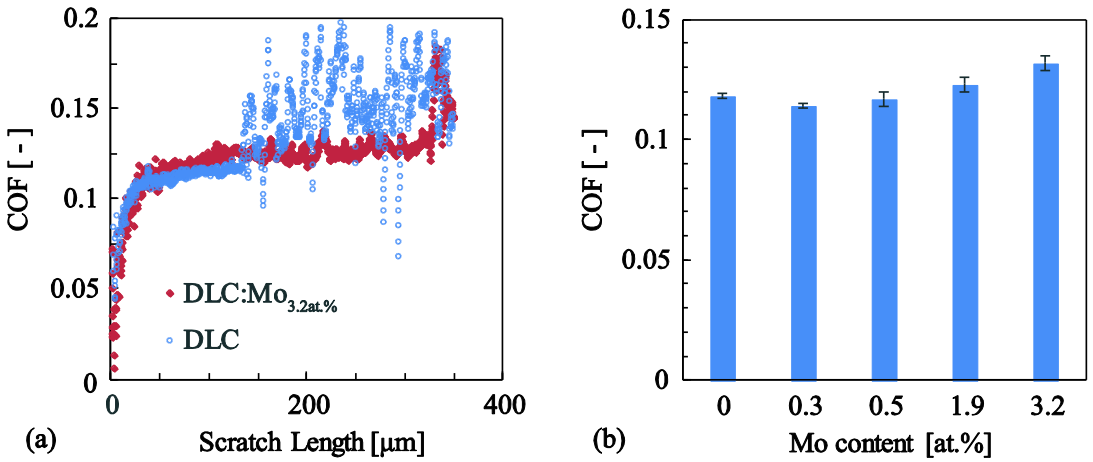

Figure 5.14 (a) COF as a function of the scratch length for two different Mo contents. (b) Average COF vales for all DLC:Mo tested herein.

5.4 Chapter summary

Through this systematic synthesis and characterization of pulsed laser deposited DLC and DLC: Mo films we can conclude that:

- Pulsed laser deposition is an efficient route for delivering hydrogen free, smooth and low friction DLC: Mo nanocomposites.

- The incorporation of molybdenum into the DLC matrix leads to the graphitization of the matrix with a subsequent reduction in the hardness of the composite material.
- While molybdenum content tends to slightly rise the roughness and friction coefficient of DLC: Mo films, the increase is insignificant and the surfaces of the coatings maintain very low coefficients of friction and sub-nanometer roughness.
- The matrix graphitization coupled with the creation of a composite system tend to increase the ductility and fracture resistance of the DLC: Mo system as quantified through the nanoscratch response of the thin films. In fact a $3.2\text{at.}\%$ molybdenum content results in a $+87\%$ enhancement in the required load to delaminate the film.
- The enhanced critical load for film failure reported for the Mo-doped DLC films is partly credited to the increased system ductility and partly to the reduced residual compressive stresses resulting from the metal-induced amorphous carbon matrix graphitization. The scratch resistance enhancements reported herein for molybdenum are more pronounced compared with the enhancements previously reported for the non-carbide forming metal, Ag.
- The critical load required for film delamination monotonically increases with the molybdenum content in the metal-doping range $(0 - 3.2\text{at.}\%)$ considered in this study.

Given the combination of high hardness, low friction, high scratch-resistance and coupled with the reported biocompatibility for both DLC and Mo [140,159] these material systems show potential for engineering applications as wear-, friction- and corrosion-reducing coatings in the automotive, biomedical or microelectronics sectors. Nevertheless, further investigation and optimization is required that will consider issues like chemical stability, diffusion barrier characteristics, etc. [136].

CHAPTER 6 Microstructure and nanomechanical properties of PECVD/PVD DLCH:Me (Me=Ag,Ti) nanocomposite films[3]

6.1 Introductory remarks

In Chapter 4 and 5 results have been presented on hydrogen-free amorphous carbon metal films. Chapter 6 and 7 deal with hydrogenated versions of amorphous carbon matrices. More precisely, metal embedded nanocomposite films $a-C:H:Ag$, $a-C:H:Ti$ are studied and show that can be competitive with respect to conventional $a-C:H$ materials. This would enable more material efficient use and application that demands durability and ductile behavior while in service. A major challenge of this study relates to the development of a hybrid PECVD/PVD system that was recently installed within the premises of the Research Unit for Nanostructured Materials Systems (RUNMS), to produce carbon composite materials with controlled structural bonding and amount of metal. The potential of PECVD/PVD system to produce $a-C:H$ films (that has the ability to provide very low lubricity under dry atmosphere than hydrogen free $a-C$, and more ductile behavior under scratch) was used. Of course, the final aim was to explore the potential opportunities of composite materials for new application. A variety of characterization methods were used to characterize the microstructure of the materials, such as X-ray reflectivity, Raman spectroscopy, Atomic Force Microscopy, and Transmission Electron Microscopy (TEM) for measuring density, thickness, chemical bonding, composition, roughness and particulate size/shape. Moreover Scanning Electron Microscopy was used for observing the failure modes of films after scratching.

[3] Results presented in this chapter have been published in the following paper: M. Constantinou, P. Nikolaou, L. E.Koutsokeras, A. Avgeropoulos, D. Moschovas, C. Varotsis, P. Patsalas, P. Kelires, G. Constantinides, Metal (Ag/Ti)-Containing Hydrogenated Amorphous Carbon Nanocomposite Films with Enhanced Nanoscratch Resistance: Hybrid PECVD/PVD System and Microstructural Characteristics, Nanomaterials, 8(4), 209, 2018.

6.2 Materials and methods

6.2.1 Deposition of nanocomposite a-C:H:Me films

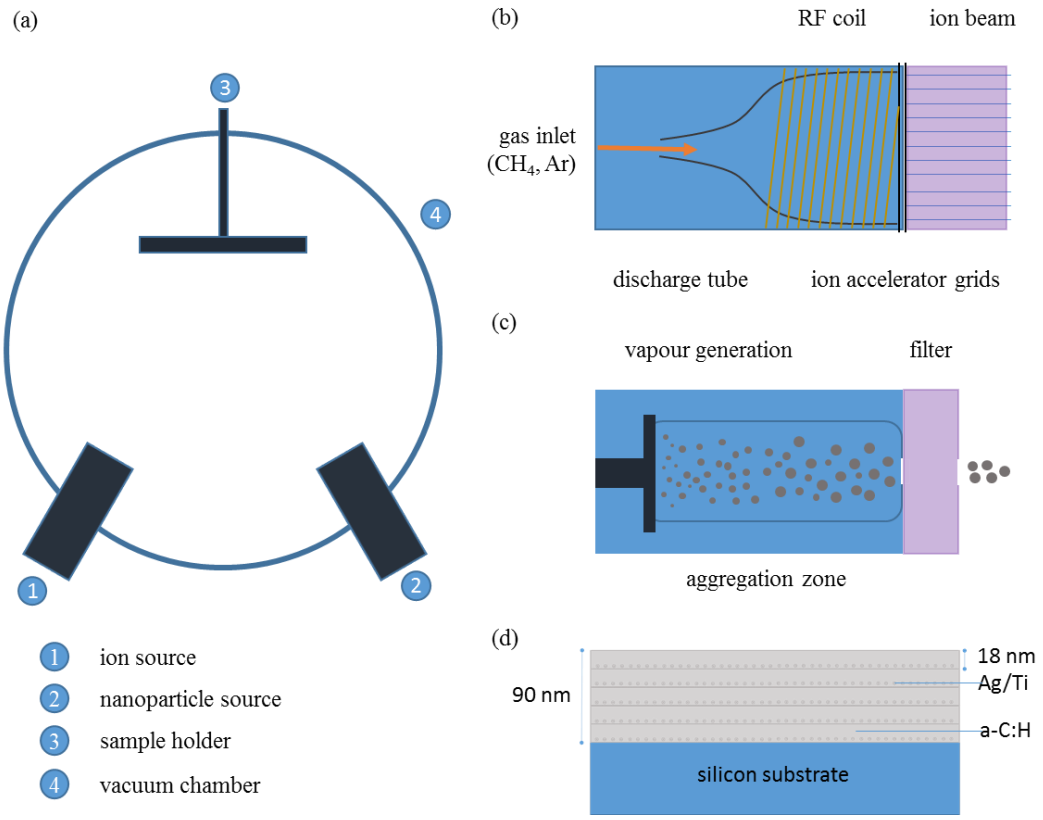

Figure 6.1 (a) Schematic of the hybrid PECVD/PVD system used within this study. Details of (b) the ion source and (c) the nanoparticle source. (d) Schematic of the metal reinforced hydrogenated amorphous carbon nanocomposite films deposited within this study (a-C:H:Ag, a-C:H:Ti).

6.2.1.1 Ion beam source

Metal-reinforced hydrogenated amorphous carbon films were deposited using a custom-made hybrid deposition system, which combines plasma enhanced chemical vapor deposition (PECVD)and physical vapor deposition (PVD) technologies. A schematic of the deposition chamber is presented in Fig. 6.1a. PECVD was achieved through radio frequency (RF) ion-beam technology, a diagram of which is presented in Fig. 6.1b. The ion beam source has an external RF antenna that spirals around the plasma tube in the form of a coil. The RF waves emitted by the antenna enter the transparent plasma tube to ionize the gas introduced therein to produce charged ions. The main chamber of the system is pumped down to 10^{-8} mbar (basic pressure) using one roughing and one turbo-molecular pumps. The energetic carbon/hydrogen ions generated from this gas-cracking process (we here use methane (CH_4) as the carbon source) are accelerated

towards the substrate by a voltage applied on a grid located between the plasma source and the substrate material. The voltage applied on the grid related to the kinetic energy of the ions. The transportation of ions from the source to the substrate occurs in line of sight conditions and working pressure on the order of 10^{-3} mbar, the exact value of which depends on the total gas flow within the discharge tube. The accelerated ion species are deposited on the substrate material to grow hydrogenated amorphous carbon ($a-C:H$) films. The ion beam arrives at an incidence angle of $30°$ to the substrate which is located $22\,cm$ away from the ion beam. In optimizing the density and deposition rate a parametric study on the effects of deposition conditions on the physical characteristics of $a-C:H$ films preceded the deposition of the metal-containing nanocomposite films ($a-C:H:Me$).

6.2.1.2 Nanoparticle source

Metal nanoparticles were generated using Nanogen50 (Mantis Deposition Ltd, UK). The nanoparticle generator (Fig. 6.1c) utilizes a variant of the PVD method, called Terminated Gas Condensation (TGC); this technology uses magnetron sputtering coupled with a condensation zone that is used to grow metallic nanoparticles (NPs). More details on the operating mechanisms of TGC can be found in Ref. [160]. Here, silver or titanium were physically vapored by momentum transfer of argon ions onto the solid target (application of sputtering voltage/power promotes the creation and then acceleration of argon ions onto the solid target). The sputtered atoms of metal target nucleate and grow into larger clusters through collisions in the gas phase. The length of the condensation zone which can be varied, affects the size distribution of the metallic clusters; longer times spend in the condensation zone results in higher collision in gas phase and thus larger clusters. The size of the metallic NPs since they have negative charge, can be consequently filtered by a quadrupole (complex of four rods) mass spectrometer (MesoQ, Mantis Deposition Ltd, UK) which is located in series with the condensation zone (see Fig. 6.1c). The quadrupole can be controlled to preselect specific NPs mass to pass through it and at the same time measure the charge/current of them (which qualitatively relates to the number of NPs per unit area per time).

In order to investigate the control on the particle size, Ag and Ti NPs were deposited on silicon substrates with sub-nanometer roughness of $0.4\,nm$ (measured through AFM). Prior to deposition, the substrates were cleaned with compressed air to remove any

possible dust particles or debris from their surfaces. Argon gas flow, sputtering current and condensation distance were set to 60 sccm, 60 mA and 8.5 cm, respectively; the working pressure in the main chamber was on the order of 10^{-3} mbar.

6.2.1.3 Hybrid deposition of a-C:H:Me(Ag,Ti) nanocomposite films

Nanocomposite films of $a-C:H:Ag$ and $a-C:H:Ti$ were deposited by sequential operation of the PECVD and PVD guns. A pattern of five layers of $a-C:H$ films (each with $\sim 18nm$ thickness with a deposition rate of $\sim 4\,nm/min$) and intermediate depositions of metallic NPs (selected nominal mean particle diameters of 4 nm for Ag and 10 nm for Ti) between each $a-C:H$ layer have been implemented. No energetic bias was applied on the substrate while the temperature was at $25-35℃$. An RF power of 200 W is applied on a CH_4/Ar mixture of $6.0\,sccm/0.5\,sccm$ while the produced carbon ions were accelerated on the substrate material using 150 V grid voltage and a background pressure of 10^{-3} mbar to produce $a-C:H$ layers with a density of $1.7g/cm^3$ (measured through X-ray reflectivity). For Ag and Ti NPs deposition, argon flow, sputtering current and condensation distance are set to 60 sccm, 60 mA and 8.5 cm respectively while the deposition time of NPs was controlled so to get a composite with different NP metal contents.

6.2.2 Characterization of nanoparticles and films

6.2.2.1 X-ray reflectivity

An X-ray diffractometer **(**Rigaku Ultima IV) was used to measure the specular X-ray reflectivity of the various deposited films. The diffractometer was equipped with a Cu tube, operated at 40 kV accelerating voltage ad 40 mA emission current. The incidence X-ray beam has been collimated into a parallel beam with a 0.03 divergence and additionally monochromatized to Cu Ka ($\lambda = 0.15419$ nm) by a curved multilayer mirror. Density and thickness of the thin films were extracted by fitting the respective experimental data to the theoretical reflectivity calculated using Parratt's formalism [161–163].

6.2.2.2 Raman spectroscopy

The microstructural details of $a-C:H:Me$ films were probed using Raman spectroscopy. Raman data were collected by a confocal LabRAM from HORIBA Jobin Yvon equipped with a CCD detector and an Olympus BX41 microscope. The 441 nm

was provided by a Kimmon Helium–Cadmium laser source. This characterization method was employed in order to (a) access the bond characteristics of the deposited $a-C:H$ films and indirectly link the information with sp^2/sp^3 configurations, and hydrogen content (i.e., I_D/I_G and FWHM(G)) [32] and (b) trace the chemical modifications imparted on the nanocomposites, $a-C:H:Ag$ and $a-C:H:Ti$, though the introduction of metal nanoparticles.

6.2.2.3 Atomic force microscopy

Atomic force microscopy (AFM) was used to quantify the size and amount of metallic nanoparticles and also to quantify the roughness of the resulting nanocomposite films. All measurements were performed in semi-contact mode using a scanning probe microscope (Ntegra Prima, NT-MDT) equipped with an NT-MDT probe (NSG10) having a mean force constant of $11.8\ N/m$ and a tip nominal radius of 6 nm. For nanoparticle size calibration AFM images were $500\ nm \times 500\ nm$ in size collected with a tip scan rate of $1Hz$ and a resolution $512\ x\ 512$ points in x-y direction. The surface topography of the deposited $a-C:H$ and $a-C:H:Me$ films was measured using contact mode and a $CSG10$ probe having a mean force constant of $0.11\ N/m$ and a nominal tip radius of 6 nm. Images of 3 μm × 3 μm and 256×256 data density were collected and subsequently software-analyzed for quantifying the root mean square (RMS) roughness of the deposited surfaces.

6.2.2.4 Transmission electron microscopy

Selected specimens were studied using transmission electron microscopy (JEOL JEM HR-2100) operated at $200\ kV$ in bright field mode. In studying the shape/size of the generated nanoparticles several depositions were made directly on formvar/carbon coated 300 mesh Cu TEM grids (Science Services GmbH, Germany).

6.2.2.5 Nanomechanical testing

The nanotribological response of the deposited $a-C:H:Me$ films was tested on an instrumented nanoindentation platform (Micro Materials Ltd, UK) using a friction bridge transducer and a conospherical diamond probe with a tip radius of 3.2 μm, as calibrated through elastic indentations on a material with known properties. The three-pass experiment with 1 ramp-load scratch test between 2 topography passes was used for scratch testing all films with 6 repetitions, with a total scratch length of 300 μm, a load applied after 50 μm distance, a scan speed of $2\ \mu m/s$ and a scratch loading rate of

$1.6\,\mathrm{mN/s}$ to reach a maximum load of $200\,\mathrm{mN}$. A $50\,\mu\mathrm{m}$ distance between each scratch was used. During all scratch tests friction data was collected that provided access to the friction coefficient. Residual scratches were subsequently studied in a scanning electron microscope (Quanta 200, FEI, Hillsboro, Oregon, USA) at various magnifications in order to link microstructural characteristics with nanotribological metrics.

6.2.2.6 Residual stress measurements

Residual stresses generated within the film during deposition were estimated using Stoney's equation (see Eq. (5.1), described in Section 5.2.2) [164]. The validity of Eq. (5.1) was ensured by respecting that the fundamental assumptions on which it was derived persist [165,166]: (i) substrate and film thicknesses are significantly smaller than the plane dimensions, (ii) film thickness ($t_f = 80\mathrm{nm}$) is significantly smaller than the substrate thickness ($t_s = 375\mu\mathrm{m}$), (iii) substrate and film are homogeneous, and (iv) residual stresses induce equal bending in both $x-y$ directions (i.e., spherical curvature and thus the biaxial stress is equal in the whole plate).

6.3 Results and discussion

6.3.1 Ion source and a-C:H deposition rate

Prior to the deposition of the nanocomposite films a series of pristine $a-C:H$ were deposited in order to study the effects of ion source characteristics on the deposition rate and physical properties of the films. The resulting thickness and density of the produced films was quantified through X-ray reflectivity measurements. The various depositions performed investigated the parameters that affect the ion beam characteristics and their link with microstructural characteristics of the films so to produce $a-C:H$ with dense packing of carbon atoms and efficient deposition rates. In general, the ion beam process can be divided into three basic steps: (i) creation of deposited species, (ii) acceleration of species from the source to the substrate, and (iii) deposition and growth of the film; the controlling variables that affect those processes are the RF power, the gas flow, grid voltage, and substrate bias/temperature. For this study, substrate bias and temperature were kept at $0\,\mathrm{V}$ and 25ºC respectively.

In investigating the effect of gas flow rate and grid voltage a series of specimens were deposited while systematically varying these two parameters. Fig. 6.2a shows that the deposition rate increases with grid voltage and the dependency is more pronounced for higher CH_4/Ar concentrations. In the system presented herein the kinetic energy of the accelerated ions is controlled by the voltage applied to the exit grid of the discharge quartz tube. It is apparent that the increase of grid voltage does not only affect the kinetic energy of the plasma generated ions but also the rate at which they pass through the grid, having as a result an increase deposited species and subsequently film thickness. Furthermore, the deposition rate also increases when the CH_4 concentration in the tube increases. Fig. 6.2(b) quantifies the effect of argon gas flow on the deposition rate of the $a-C:H$ films. It is apparent that an increase in the relative volume fraction of argon flow relative to the total gas flow in the discharge tube (argon and methane) significantly reduces the film thickness. It should be noted that the total gas flow rate was kept constant (6.5 sccm) such as the pressure within the chamber remained relatively unaffected. The highest thickness among the produced films is observed for argon/methane flow rates of 0.5 sccm$/6.0$ sccm (a volume fraction of ~8%) whereas for argon/methane flow rates of 2.5 sccm$/4.0$ sccm (argon volume fraction of ~38%) the thickness of the deposited films is significantly reduced by -65%. This phenomenon is partly related to the fact that argon ions generated within the plasma chamber and accelerated towards the specimen promote etching to the surface of the deposited material (it should be noted that argon atoms are significantly heavier than carbon atoms) thus decreasing deposition rate and thickness of $a-C:H$ films. Furthermore, the increase of argon volume fraction while maintaining a constant gas flow rate within the chamber leads to a gradual reduction in the methane volume fraction which is the source of carbon ions, and its reduction inevitably leads to a reduction in the deposition rate and thickness of the deposited material. The density values of all films deposited herein vary within 1.52 g$/$cm$^3 - 1.80$ g$/$cm^3.

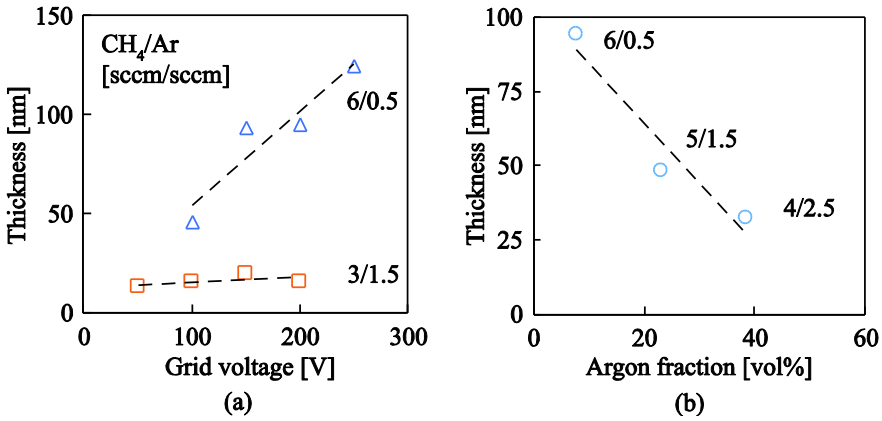

Figure 6.2(a) Effect of grid voltage on thickness for two different gas flow rate combinations: CH_4/Ar=6.0 sccm/0.5 sccm and CH_4/Ar=3.0 sccm/1.5 sccm; results are for RF power of 200 W and grid voltage of 150 V. (b) Effect of volume fraction on film thickness; results are for RF power of 200 W and grid voltage of 150 V and a constant total gas flow rate in the chamber (CH_4 + Ar = 6.5sccm).

6.3.2 Ag and Ti nanoparticles

A series of silver and titanium nanoparticle depositions were performed on silicon and TEM grid substrates in order to confirm the ability of the nanoparticle source to generate nanoparticles with precise sizes and calibrate at the same time the deposition rates that were required for the controlled composition of the nanocomposite films. Table 6.1 shows details of the set of silver nanoparticle samples synthesized using NanoGen50 where the preselected nominal particle size has been varied while retaining a grounded substrate and a constant deposition flux, defined as the product of ion current (j) with deposition time (t):

$$K = j \times t \qquad (6.1)$$

Consequently, for a given ion current (which is experimentally tractable) the deposition flux can be easily controlled by controlling the duration of a given deposition.

Table 6.1 Deposition details for a series of silver nanoparticle specimens with nominal diameters in the 4 to 12 nm range. Argon flow, magnetron position, and sputtering current where set at 60 sccm, 8.5 cm, and 60 mA respectively. The substrate was grounded and the size was selected using the MesoQ filter. The deposition time varied in order to maintain constant flux conditions.

Samples	Working pressure (mbar)	Nominal size (nm)	Deposition time (s)	J (nA)	K = J*t (nA.s)
Ag_{12nm}	4.9×10^{-3}	12	60	0.03	1.8
Ag_{9nm}	4.8×10^{-3}	9	18	0.10	1.8
Ag_{6nm}	4.8×10^{-3}	6	11	0.17	1.8
Ag_{4nm}	4.8×10^{-3}	4	45	0.04	1.8

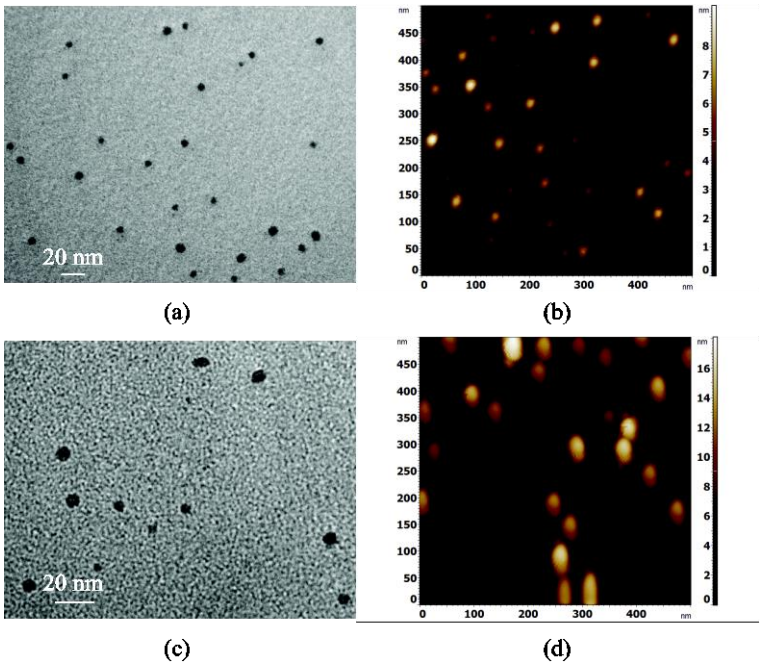

Figure 6.3 TEM (a, c) and AFM (b,c) images of Ag (a,b) and Ti (b,c) nanoparticles synthesized using the nanoparticle source. Nominal diameters for Ag and Ti were 4 nm and 11 nm.

Figure 6.3 shows TEM (Fig. 6.3a and 6.3c) and AFM (Fig. 6.3b and 6.3d) images of the generated Ag (Fig. 6.3a and 6.3b) and Ti (Fig 6.3c and 6.3d) nanoparticles. The images testify towards the ability of the nanoparticle source to generate a non-agglomerated group of almost spherical nanoparticles with controlled diameters. In order to quantify the sizes of the Ag and Ti nanoparticles the images were digitally analyzed. For all the samples, the size and number of NPs were counted by the threshold method [167,168] which makes the assumption that the nanoparticles are spherical and rest on a substrate with minimal roughness. During the levelling process the particles were excluded from the fit to avoid local distortions of the data. Figure 6.4 shows the experimentally

obtained diameters in comparison with their nominal values for the various Ag NPs synthesized. It is evident that the TEM results are in excellent agreement with AFM data and confirm the ability of NanoGen to deposit NPs with controlled sizes and minimal size distributions. Some minor deviations between the experimental and nominal values can be attributed to the quadrupole filter which potentially could be optimized for even more refined correspondence between the two.

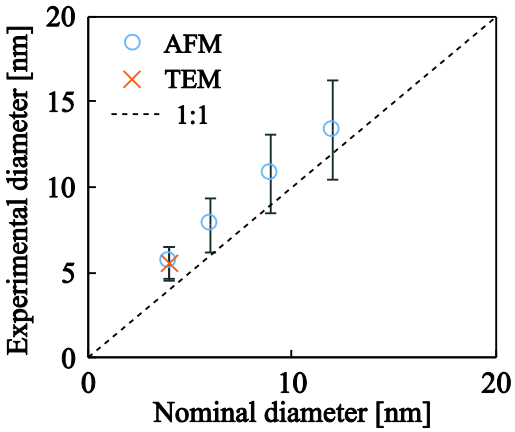

Figure 6.4 Experimental versus nominal nanoparticle diameters for a series of Ag nanoparticle depositions. Experimental diameters were obtained from AFM and TEM images after digital image analysis.

Figure 6.5a shows the particle density, calculated through AFM images in billions of nanoparticles per square millimeter, as a function of the deposition time. The details of the samples synthesized towards this end are presented in Table 6.2 and the experiments were performed in order to quantify a measure of the deposition rate that allowed us to generate nanocomposite $a-C:H:Me$ films with controlled compositions. The samples presented in Fig. 6.5a had a nominal size of $4\,nm$ and various deposition times preselected to achieve various coverages/densities. Fig. 6.5b and 6.5c show AFM images of low and high NP coverage respectively. The AFM images were analyzed using the threshold routine and the values of np density are plotted in Fig. 6.5a. As expected, an increase in deposition time increases the number of NPs per mm^2 and this trend appears to be linear with a resulting deposition rate of $0.0722 \times 10^9\ mm^{-2}min^{-1}$. The same experimental process has been followed for Ti NPs showing an almost identical deposition rate.

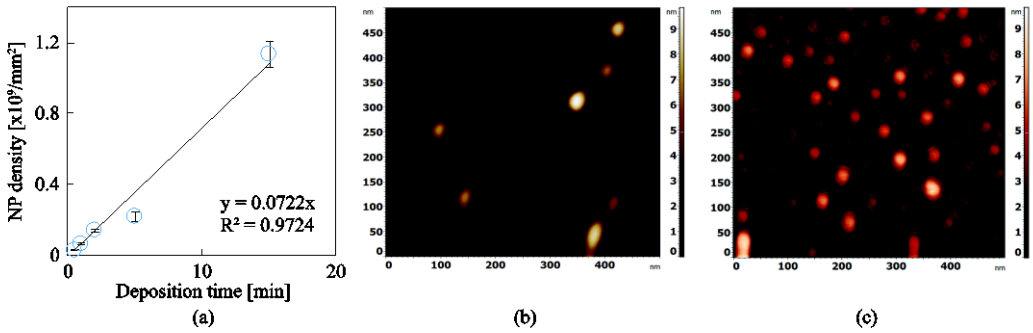

Figure 6.5 (a) Ag nanoparticle density for various deposition times; results associated with samples presented in Table 6.2. (b) AFM image of a low deposition time and (c) high deposition time.

Table 6.2 Deposition conditions for 4 nm nominal diameter Ag nanoparticles grown at various durations and 0 V substrate bias. Argon flow, magnetron position, and sputtering current were set at 60 sccm, 8.5 cm and 60 mA.

Samples	Working pressure [mbar]	Nominal size [nm]	Deposition time [s]	J [nA]	K = J*t [nA.s]
Ag_{30s}	4.7 x 10^{-3}	4	30	0.3	9
Ag_{60s}	4.7 x 10^{-3}	4	60	0.3	18
Ag_{120s}	4.7 x 10^{-3}	4	120	0.3	36
Ag_{300s}	4.7 x 10^{-3}	4	300	0.3	90
Ag_{900s}	4.7 x 10^{-3}	4	900	0.3	270

6.3.3 a-C:H:Ag and a-C:H:Ti nanocomposite films

6.3.3.1 Microstructural details and bonding characteristics

Details of the nanocomposite films prepared and tested within this study are shown in Table 6.3. The reported particle size relates to the experimentally obtained values (AFM and TEM analysis) whereas the metal contents were estimated through the calibration curves reported in Fig. 6.4 and Fig. 6.5. The PECVD and PVD guns were operating in alternating turns (5 repetitions each) in order to generate multi-layer films of ~80nm in thickness and intermediate nanoparticle depositions with concentrations as reported in Table 6.3. The hydrogenated amorphous carbon matrix used in all nanocomposite films was deposited using an RF power of 200 W, a gas mixture of $CH_4/Ar = 6.0$ sccm / 0.5 sccm and grid voltage of 150 V, which resulted in a film density of 1.7 g/cm^3 as quantified through X-ray reflectivity measurements.

Table 6.3 Deposition details of the nanocomposite films grown in this study and the resulting surface roughness as quantified through AFM. PVD conditions: Argon flow, magnetron position, and sputtering current were set at 60 sccm, 8.5 cm and 60 mA. PECVD conditions: 6 sccm/0.5 sccm (CH_4/Ar), 200W RF power and 150 V grid current.

Material	NP size [nm]	Me content [at.%]	RMS roughness [nm]
$\mathbf{a-C:H}$	-	0	0.4 ± 0.1
$\mathbf{a-C:H:Ag_{0.23at.\%}}$	5.6	0.23	1.8 ± 1.0
$\mathbf{a-C:H:Ag_{0.33at.\%}}$	5.6	0.33	2.0 ± 0.6
$\mathbf{a-C:H:Ti_{0.33at.\%}}$	11.3	0.33	5.3 ± 0.9
$\mathbf{a-C:H:Ti_{0.56at.\%}}$	11.3	0.59	4.8 ± 0.2

TEM images suggest that the metallic nanoparticles are crystalline in nature (single crystals in most cases) and retain their original compositions, i.e., neither Ag nor Ti nanoparticles chemically react with the surrounding $a-C:H$ matrix. Figure 6.6 shows a high resolution TEM image of a Ti nanoparticle embedded in an $a-C:H$ matrix. A closer investigation at the $Ti/a-C:H$ interphase coupled with a 2-dimensional fast Fourier transform of the cropped section suggests that (a) the nanoparticle exhibits d-spacings of 0.234 nm which correspond to the interplanar distance of Ti (002) planes, which translates to the fact that titanium carbide is not formed and (b) the aureole that is formed around the Ti NP shows characteristics of crystallinity with d-spacings on the order of 0.172 nm that can be related to the (004) planes of graphite, suggesting that the vicinity to the nanoparticles surface graphitizes, the extend of which can be estimated up to 10 atomic planes (~ 3 nm).

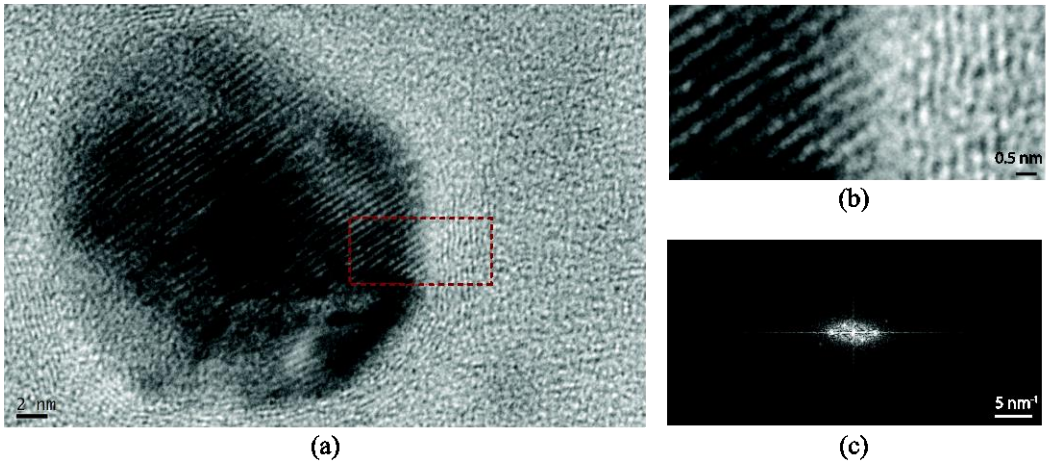

Figure 6.6 (a) High resolution TEM image of a Ti nanoparticle with the surrounding a-C:H matrix. (b) A magnified view of the a-C:H/Ti interface showing the transition in crystalline domains. (c) 2D FFT of image selection, identifying the two dominant d-spacings.

The Raman spectra for $a-C{:}\,H$ and $a-C{:}\,H{:}\,Me$ nanocomposites are presented in Fig. 6.7a. All spectra exhibit the characteristic shape for amorphous carbon; the cumulative response was deconvoluted to the D-band ($\sim 1350\ cm^{-1}$) and G-band ($\sim 1550\ cm^{-1}$) contributions using Gaussian fits. Several important metrics, including the location of the G peak, the intensity ratio of D over G peaks (I_D/I_G) and the full width at half maximum of the G Peak (FWHM (G)) were extracted and the results are shown in Figure 6.7. In general, the D peak is due to the vibration of sp^2 rings and the G peak to the resonance of the sp^2 atoms organized in both rings and chains. Subsequently, the higher the I_D/I_G ratio the higher the sp^2 clustering within an $a-C{:}\,H$ sample.

Figure 6.7a shows the Raman spectra for $a-C{:}\,H$ and its deconvolution into the contributions of D and G bands that yield an intensity ratio of $I_D/I_G = 0.45$. Empirical relations obtained from experimental data on a large collection of data on hydrogenated amorphous carbon films suggest that this intensity ratio is inversely related with both the hydrogen content [32] and (indirectly through the Tauc gap) with the sp^3 hybridization state [169]. A comparison of this experimentally obtained value with literature data suggests that the pure $a-C{:}\,H$ film synthesized within this study consists of a hydrogen content of $20-25\ at.\%$ and an sp^3 content of approximately $50\ at.\%$. An $a-C{:}\,H$ film with such characteristics is commonly referred to as diamond-like $a-C{:}\,H$ ($DLC{:}\,H$) with density values that vary between $1.5\ g/cm^3$ to $1.8\ g/cm^3$ and high sp^3 bonds (up to $70\ at.\%$), a significant percentage of which are hydrogenated

terminated [12,33]. Indeed, our $a-C:H$ matrix with a density of $1.7\ g/cm^3$ (measured through XRR), hydrogen content of ~ 25 at. % and sp^3 content of ~ 50 at. % falls within the $DLC:H$ category [32]. It should be noted that the empirical relations utilized herein were obtained with an excitation wavelength of 514 nm, whereas the wavelength utilized in this study was 441 nm. Nevertheless, experimental evidence suggests that the effect of excitation wavelength on the I_D/I_G is minimal and therefore the curves obtained with 514 nm excitation are not expected to significantly deviate from the 441 nm results [12,170].

The $FWHM(G)$ probes the structural disorder of the sp^2 clustering in amorphous carbon material [169,171]. A lower $FWHM(G)$ value denotes an $a-C:H$ with less unstrained sp^2 clustering, whereas a higher $FWHM(G)$ value suggests a material with an increased disordering in bond lengths and angles for the sp^2 clusters. The reduction of $FWHM(G)$ with metallic doping (from 165 to 155, see Figure 6.7b) suggests that the introduction of both Ag and Ti nanoparticles tends to reduce the structural disorder which is consistent with the graphitization of the surrounding matrix as evidenced in TEM images (Fig. 6.6) and the observed increase in the I_D/I_G ratios and the subsequent reduction of the residual stresses through the relief of strain energy introduced in distorted bond lengths and bond angles. Furthermore, the G peak position shifted slightly to higher wavenumbers, in particular from $1552\ cm^{-1}$ to $1559\ cm^{-1}$ with the incorporation of Ag and/or Ti metal within $a-C:H$ matrix resulting to higher sp^2 clustering. This is consistent with the $FWHM(G)$ reduction which also signifies an increase of sp^2 clustering as it falls following a reverse trajectory from amorphitization for composite samples. Our results are in very good agreement with literature data [9,18,172].

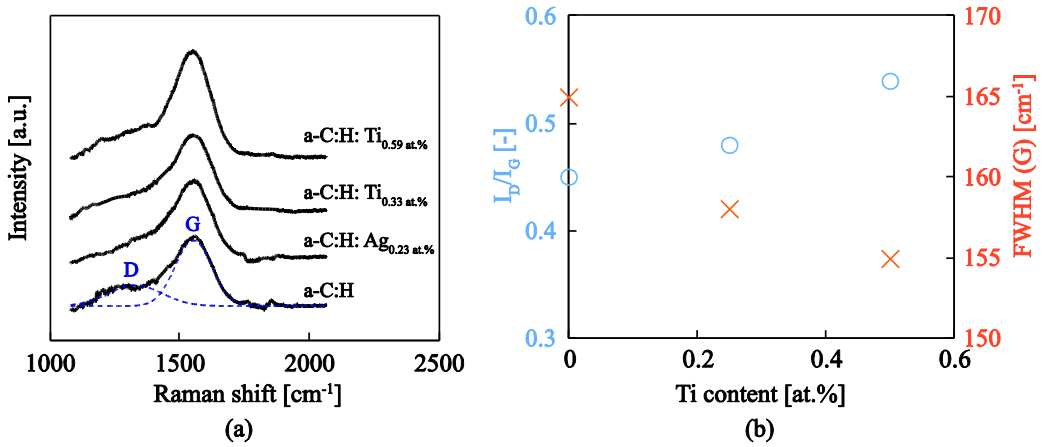

Figure 6.7 Raman spectra for the nanocomposite films tested within this study showing also the deconvoluted Raman spectra for $a-C:H$, fitted by Gaussian curves at D and G carbon band resonant frequencies.

The surface roughness of $a-C:H$ films deposited under controlled conditions onto a flat silicon substrate is measured at $0.4 \pm 0.1\,nm$ which is consistent with hydrogenated amorphous carbon values reported in the literature. The introduction of metallic nanoparticles within the $a-C:H$ matrix increases the surface roughness of the $a-C:H:Ag$ and $a-C:H:Ti$ nanocomposite films as presented in Table 6.3. The increase in roughness for composites can be attributed to nanoscale protrusions that are generated beyond the nanoparticles as an overlay of $a-C:H$ film is deposited. It is interesting to note that the increase in the roughness for the $a-C:H:Ti$ is more pronounced which is probably related to the higher nanoparticle size used for these nanocomposites in comparison to $a-C:H:Ag$.

Residual compressive stresses as calculated through curvature measurements and the Stoney equation are shown in Figure 6.8. Consistent with literature data, $a-C:H$ films deposited using PECVD contain a significant amount of stresses ($\sim 2.3\,GPa$) that are trapped within the material during the deposition process. The introduction of metallic nanoparticles appears to have a positive effect on the nanocomposite response as a significant proportion of the residual stresses are relaxed: -26% for Ag and -33% for Ti. This is related to the graphitization of the matrix with the introduction of metallic nps and the release of energy trapped within angular and linear bond-distortions. This observation is also in line with the Raman results presented above. This stress-reduction

mechanism increases the stability of the film and enhances the required critical load for film delamination, as it is evidenced below.

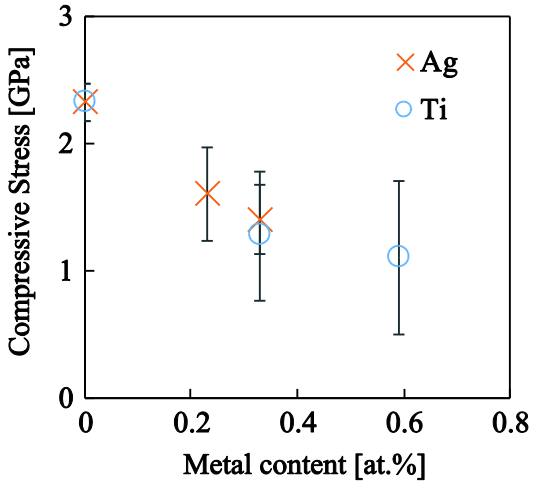

Figure 6.8 Residual stresses of the nanocomposite films as a function of the metal content.

6.3.3.2 Nanotribological response: scratch resistance and friction coefficient

The tribological performance of all $a-C:H$ and $a-C:H:Me$ nanocomposites deposited within this study was investigated by the nanoscratch method [113,173–175] and the extracted critical loads for yielding, cracking, and delamination are reported in Table 6.4. Figure 6.9 shows typical data from a three-pass scratch test on $a-C:H$ film, using a conospherical probe. A low load scan before and after the scratch test provided topography information that (a) were used to correct from initial background tilt and topography and (b) detect film/substrate deformation responses due to applied contact pressures. The key features that are observed in scratch tests are: (a) the load related to the departure from elastic to plastic deformation (denoted as P_y), (b) the load to initiate film edge cracking (denoted as P_{CL1} and P_{CL2}; note that the difference between these two critical loads might be lie in subsequent cracks beyond edge cracks something that it is worth more investigation) , and (c) the load for full film fracture (denoted as P_{CL3}). The load required to initiate plastic deformations can be detected from the deviation of the residual scratch depth from initial topography that is an increase of the residual depth (topography scan during pass 3, Figure 6.9b). It should be noted that P_y is indicative to the substrate initial plastic deformation and not to the film properties itself as evidenced by calculations on the maximum stress location which is well within the substrate material [72,139]. An additional step on the residual scratch depth reveals film crack initiation while any large fluctuations of residual scratch depth relate to film fracture

and delamination from the substrate. Furthermore, the friction force evolution with scratch distance (Figure 6.9c) is an alternative convenient means to detect/confirm P_{CL3} for delamination fracture. Plastic deformation, cracking and film failure changes were also confirmed microscopically from SEM images. For the pristine $a-C:H$ the average critical loads for yielding, cracking and failure were $Py = 5.3\,mN$, $P_{CL1} = 18.2\,mN$, $P_{CL2} = 48.0\,mN$, and$P_{CL3} = 114.8\,mN$. The extracted critical loads for all the films tested herein are summarized in Table 6.4.

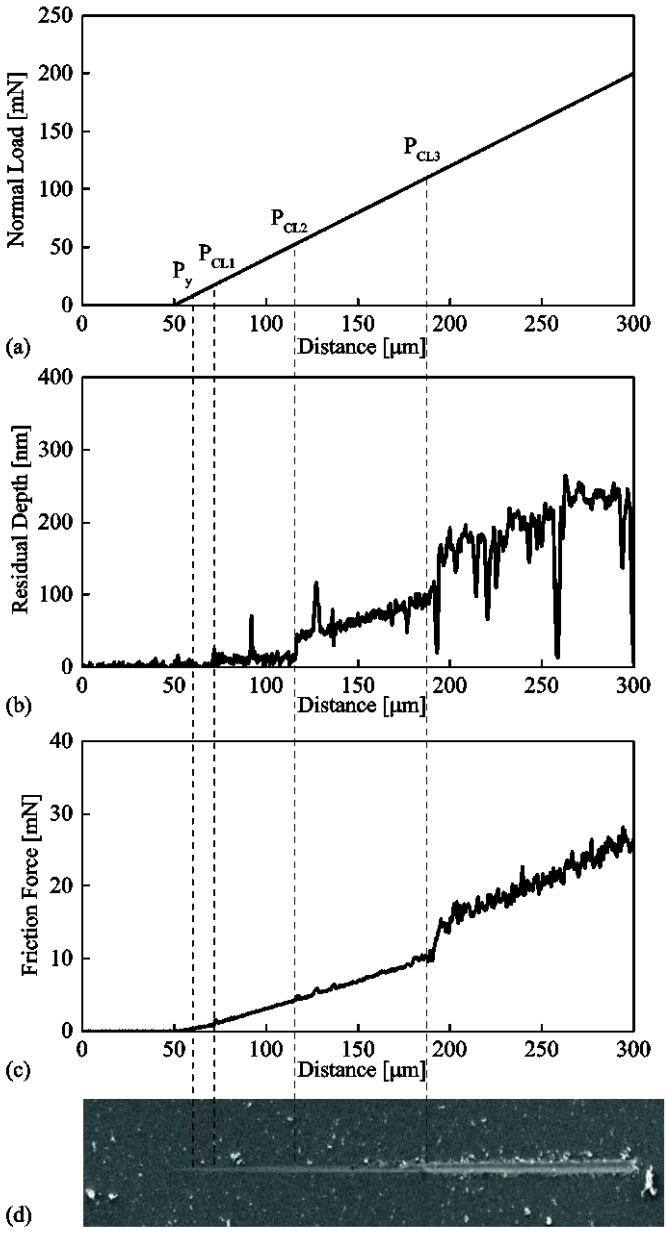

Figure 6.9 Typical results from a nanoscratch test on a-C:H film. (a) Applied load, (b) residual depth and (c) resulting frictional force as a function of the scratch distance.

Table 6.4 Summary of tribomechanical metrics extracted from nanoscratch tests.

Samples	P_y (mN)	P_{CL1} (mN)	P_{CL2} (mN)	P_{CL3} (mN)	COF (-)
a-C:H	5.3 ± 0.6	18.2 ± 2.7	48.0 ± 7.7	114.8 ± 24.7	0.035 ± 0.002
a-C:H:Ag$_{0.23at\%}$	4.5 ± 0.3	22.6 ± 3.7	54.2 ± 9.1	156.6 ± 7.5	0.019 ± 0.004
a-C:H:Ag$_{0.33at\%}$	5.4 ± 0.7	23.5 ± 3.8	54.7 ± 9.3	162.8 ± 12.5	0.020 ± 0.003
a-C:H:Ti$_{0.33at\%}$	4.7 ± 0.6	18.5 ± 2.9	49.8 ± 2.9	123.8 ± 31.5	0.041 ± 0.004
a-C:H:Ti$_{0.59at\%}$	4.9 ± 0.4	18.8 ± 1.7	52.0 ± 5.0	133.0±13.1	0.040 ± 0.006

The $a-C:H$, $a-C:H:Ag$, and $a-C:H:Ti$ films exhibited similar critical loads for transitioning from elastic to plastic deformations. More precisely, the average P_y values for these films were found to be 5.3 mN, 4.5 mN, 5.4 mN, 4.7 mN and 4.9 mN respectively. Beyond that, the average values of the critical loads required for cracking initiation, P_{CL1}, were found to be 18.2 mN, 22.6 mN, 23.5 mN, 18.5 mN and 18.8 mN respectively; for all nanocomposite cases the average values were higher than the value for neat $a-C:H$ film. Furthermore, the delamination loads found for composite films in all the cases were higher compared to the neat $a-C:H$ film; this can be clearly seen comparing either the residual imprints. Indicative SEM images of residual imprints on pristine and metal doped nanocomposite films are shown in Figure 6.10, where is evident that the initiation of delamination is shifted to higher loads, see also Figure 6.11.

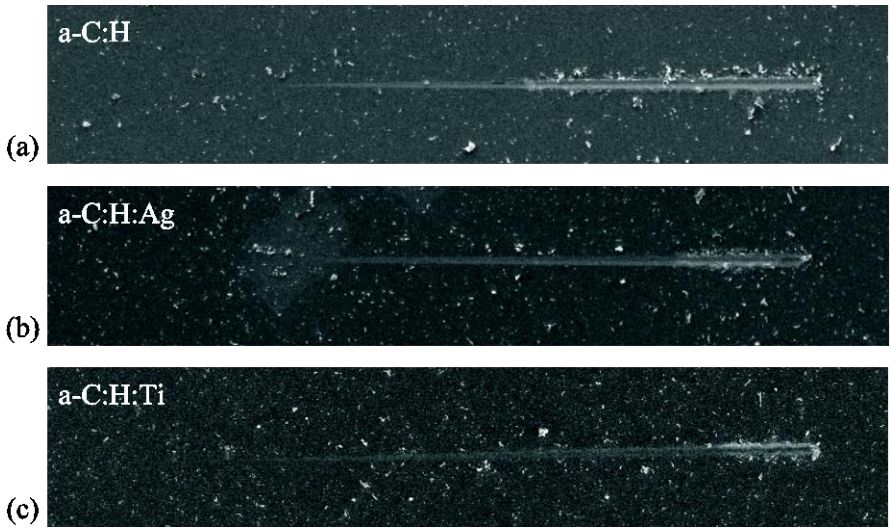

Figure 6.10 Characteristic residual scratches on a-C:H and a-C:H/Ag films.

The enhancement in scratch resistance exhibited by $a-C:H:Ag$ and $a-C:H:Ti$ systems is in line with bonding characteristics extracted from Raman measurements. The increase of (I_D/I_G) ratio and decrease of structural disorder through FWHM(G)

value with metal content imply an increase of sp^2 clustering and deviation from amorphitization trajectory and hard materials. It is therefore clear that silver and titanium promote the graphite-like properties and both reduce hardness and increase ductility and abrasion resistance as well. These conclusions are well supported from experimental and theoretical studies in literature; concerning the increase of sp^2 clustering with the present of amount and size of silver on can refer to Refs. [9,102,151], while the decrease of hardness and increase of abrasion resistance is discussed in Ref. [139]. Here it is important to state that although nanoparticle size found to well control during deposition, the existing of higher clusters are inevitable which are more detrimental for $C-C\ sp^3$ breaking and thus promote increase of sp^2 phase.

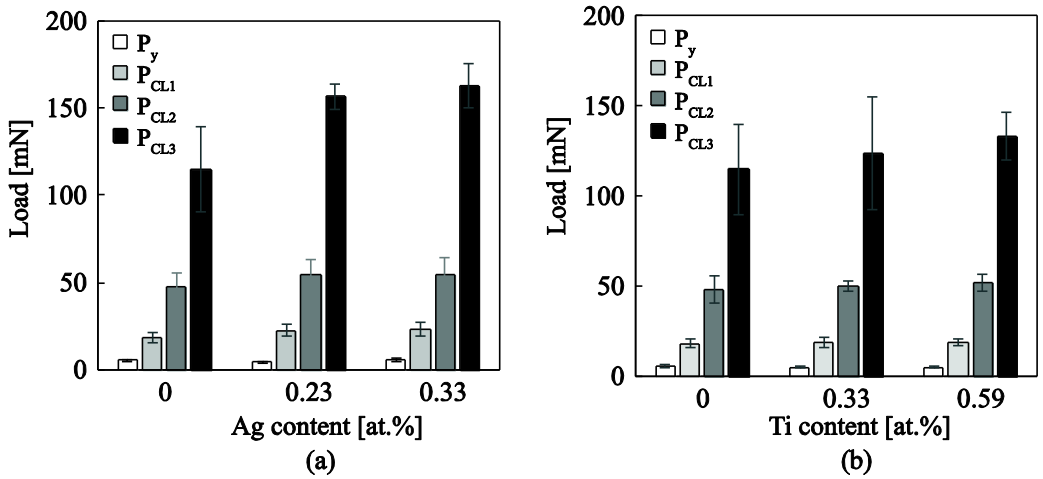

Figure 6.11 Critical loads for yield, cracking and delamination as quantified through scratch tests for (a) a-C:H:Ag and (b) a-C:H:Ti.

For such systems residual stresses is also significant parameter the increase of which prompt delamination and early fracture during scratching. Here residual stresses measured for metal-$a-C$ systems samples were found decreased compared with $a-C:H$ (see Figure 6.8). This decrease of residual stresses together with the chemical, physical and synthesis characteristics of metallic particles are beneficial for the increase of abrasion resistance of the films. For example, for $a-C:H:Ag$ composite,Ag softness, chemical inertness with carbon, and, good dispersion and geometrical characteristics as well as lowering of residual stresses, provoking ductility, toughness and scratch resistance to higher values in contrast with $a-C:H$ matrix. The same stands for $a-C:H:Ti$ films.

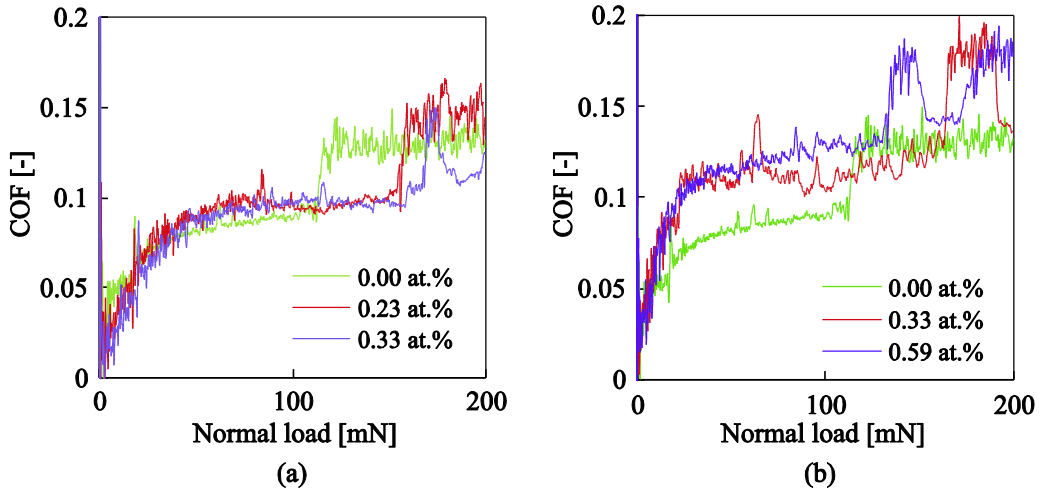

Figure 6.12 Coefficient of friction as a function of applied load for (a) a-C:H:Ag and (b) a-C:H:Ti nanocomposite films.

The coefficient of friction (COF) is another property of great significance which controls the tribological characteristics of these type of films. Figs. 6.12(a) and 6.12(b) show the evolution of COF with the applied load during the scratch test for $a-C:H:Ag$ and $a-C:H:Ti$ respectively. For low loads the contact pressure is below the yield limit of either the film or the substrate and the COF is very low ($\sim 0.02-0.04$). As the contact pressure increases COF increases in a non-linear fashion with the applied load, subsequently reaching constant values until the film fails which can be noted with a sudden increase in the COF vs. applied load response. The increase of COF with the applied load relates to the plasticity and plowing effect of diamond probe within the $a-C:H$ film [176]. As COF increases the stress beneath the contacting probe becomes more significant with the possibility of failure to follow the probe [177]. Such a response is not directly detectable in the COF vs applied load evolution but can be observed in the residual surface profiles through probe line scans or SEM images (see Figure 6.9).

The average COF values calculated within the elastic contact regime ($P < P_y$) for all films tested herein are shown in Figure 6.13. The COF value for pure $a-C:H$ is 0.035±0.002 which is in agreement with values reported in the literature for similar material systems and testing conditions [178]. The very low COF values have been attributed to the formation of a tribolayer between the probe and film that acts as a solid

lubricant that suppresses both COF and wear. The introduction of silver into the system tends to lower the COF into even smaller values (~0.020). The enhancement of lubrication in the silver-doped amorphous carbon systems has been reported in [179,180] and can be attributed to the solid lubricant properties induced by the soft silver nanoparticles [9,181]. The introduction of Ti nanoparticles into the a − C: H tends to slightly increase the COF (even though the increase is within the standard deviation of the experimental results) which might be attributed to the increased roughness generated by the larger size of Ti NPs and the increased elasticity/hardness of the Ti NPs which might delay the yielding of the a − C: H and the generation of the transfer layer. An increased COF for surfaces with higher roughness has been documented in Erdemir *et al* [182] and has been attributed to the more extensive ploughing contribution that existed in such surfaces.

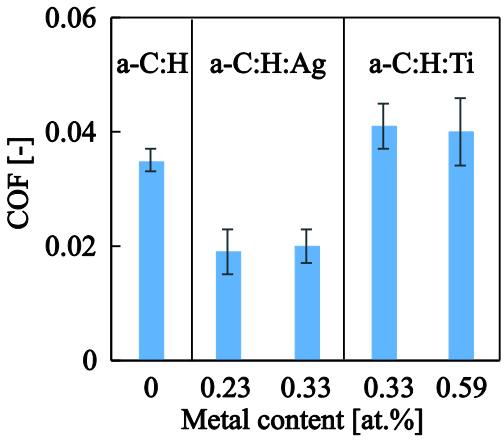

Figure 6.13 COF values for the a-C:H and a-C:H:Me films deposited in this study. The COF values reported correspond to the average values calculated within the elastic domain ($P < P_y$).

6.4 Chapter summary

During this study a novel hybrid (PVD/CVD) deposition system was used to deposit nanocomposite a − C: H: Me films. The following conclusions are drawn:

- The matrix characteristics can be tailored by controlling the gas flow within the discharge tube, the RF power and the grid voltage.

- The nanoparticle source can deliver non-agglomerated spherical nanoparticles whereas the quadruple filter (MesoQ) can narrow the particle size distribution and pre-select particles with nanometer accuracy.
- AFM and TEM results testified towards the ability of particle size monitoring and were also used to calibrate the deposition rate for controlled nanocomposite film compositions.
- The PECVD system delivered an $a-C:H$ matrix with $20-25\%$ hydrogen content and sp^3content of about 50% as indirectly estimated through Raman spectroscopy.
- Hydrogenated amorphous carbon films with embedded Ag or Ti nanoparticles were deposited and exhibited very low coefficients of frictions (< 0.05) and enhanced nanoscratch resistance ($10-50\%$). This improved nanotribological response can be traced to the reduced residual stresses, and the higher matrix ductility caused by the graphitization of the $a-C:H$ and the release of strain energy.
- These improved material systems retain their nanometer scale roughness and could be potentially exploited for biomedical or protective applications.

CHAPTER 7 Nanotribological response of a-C:H coated metallic biomaterials: the cases of stainless-steel, titanium, and niobium[4]

7.1 Introduction

The potential of hydrogenated amorphous carbon films developed within Chapter 6 is here explored for biomedical applications. a-C:H films are deposited on metallic substrates that are commonly employed as implants. Several studies evaluated the *in vitro* and *in vivo* performance of $a-C$ coated stents and mechanical heart valves [183,184]. They have concluded that the coating may contribute to a reduction in thrombogenicity by suppressing platelet adhesion and activation, and in inflammatory response by minimizing the release of cytotoxic metal ions. Additionally, $a-C$ coating has been shown to improve the corrosion resistance behavior of titanium and Ti_6Al_4V alloys for dental implants [185], as wells as to serve as a galvanic corrosion barrier between dental implant abutments and nickel-chromium superstructures [186]. Although numerous studies have indicated the excellent potential of $a-C$ in biomedical applications, the findings have been variable in terms of material substrate, deposition method and coating characteristics. We here provide a systematic characterization of the morphological, nanomechanical and nanotribological properties of three metallic materials, commonly used for the fabrication of orthopedic, cardiovascular and dental implants: stainless steel(SS), titanium (Ti) and niobium (Nb). Whether as bare metals or with a coating material, SS and Ti have been the most popular metals for biomedical applications due to their good mechanical properties and excellent corrosion resistance. Nb appears as a very promising alloying element that satisfies the prerequisites of biocompatibility and hemocompatibility and that could substitute the cytotoxic nickel element from titanium alloys while retaining the key characteristics (i.e. shape memory

[4] Results presented in this chapter have been published in the following paper: Konstantinos Kapnisis, Marios Constantinou, Maria Kyrkou, Petros Nikolaou, Andreas Anayiotos, Georgios Constantinides, 'Nanotribological response of a-C:H coated metallic biomaterials: the cases of stainless steel, titanium, and niobium', Journal of Applied Biomaterials and Functional Materials, 2018.

effect, super-elasticity) of nitinol[187–189] .The tested materials were subsequently coated with hydrogenated amorphous carbon ($a-C:H$), using a plasma-enhanced chemical vapor deposition system, in order to evaluate for improved nanotribological response.

7.2 Materials and methods

7.2.1 Metallic substrates

Metallic plates have been purchased from Goodfellow Cambridge Ltd. Stainless steel 316L grade (SS), titanium (Ti) and niobium (Nb) metal plates (1 cm x 1 cm) were pre- and post-coating deposition examined for their topographical and morphological characteristics, using an atomic force microscope and a scanning electron microscope, respectively. Furthermore, the materials were tested for their nanomechanical and nanotribological properties using an instrumented indentation platform, from which the hardness, elastic modulus and coefficient of friction have been extracted.

7.2.2 Synthesis and characterization of $a-C:H$ coated metallic susbtrates

A plasma-enhanced chemical vapor deposition system (PECVD) described in detail in Section 6.2.1.1 was used to deposit $a-C:H$ film on SS, Ti and Nb substrates. The coating thickness and density were determined by X-ray reflectivity (XRR) measurements (example data of which are presented in Figure 7.1), while substrates and film roughness were determined by analyzing 10μm x10μm images acquired using contact mode atomic force microscopy (AFM), procedures also described in section 6.2.2.1 and 6.2.2.3.Nanoindentation and nanoscratch testing were performed with a NanoTest system, details of which are provided in Section 4.2.3 and 4.2.4. Nanoindentation was performed using a Berkovich indenter at a maximum applied load of 100 mN. Nanoscratch tests were performed using a spheroconical diamond indenter. Load-displacement responses, scratch depths (Fig. 7.2 (b)), friction forces (Fig.7.2(c)) and post-test SEM were used to investigate mechanical values and failure behavior of films.

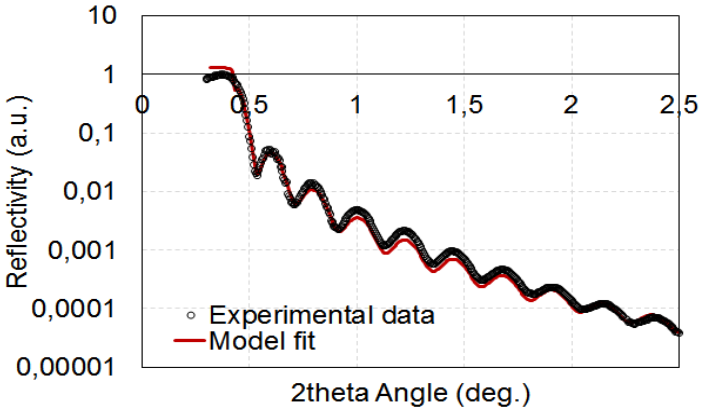

Figure 7.1 X-ray reflectivity data and model fit on the hydrogenated amorphous carbon coated silicon substrate for density and thickness determination purposes.

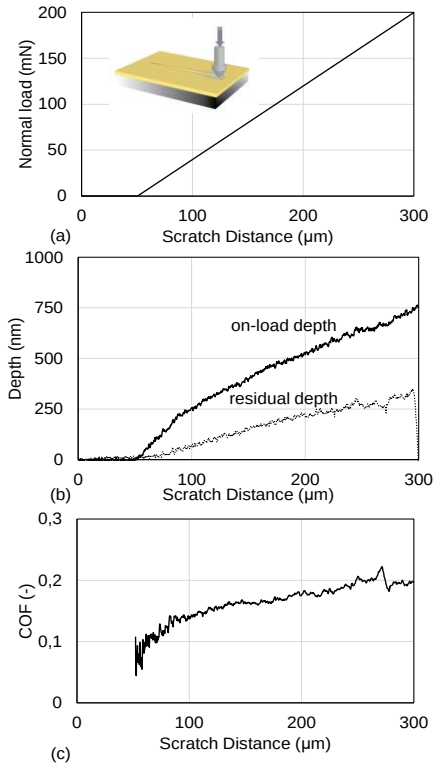

Figure 7.2 A typical nanoscratch test on SS bare metal: (a) Load profile, (b) on-load (solid line) and residual (dotted line) depth profile, (c) coefficient of friction (COF) evolution with scratch distance.

7.3 Results and discussion

7.3.1 Morphological and microstructural characteristics

Figure 7.3 shows $10\mu m \times 10\mu m$ AFM images of bare (uncoated) and $a-C:H$ coated Stainless Steel (SS), Titanium (Ti) και Niobium (Nb) surfaces. The bare metal

SS specimen was mechanically abraded and polished in successive steps of increasing grit until nanoscale roughness was achieved (12.9 ± 1.4 nm). The Ti and Nb specimens were left in their delivered surface conditions (430.8 ± 227.1 nm and 17.0 ± 7.0 nm respectively) to investigate coating performance on native (unpolished) surfaces. Evaluation of the $a-C{:}H$ coated specimens showed an approximately 2-fold decrease in surface roughness for the SS (6.8 ± 0.8 nm) and Ti (250.5 ± 46.5 nm) and a moderate decrease for the Nb (14.5 ± 3.4 nm) sample. The calculated RMS roughness for all coated and uncoated samples are reported in Table 7.1.

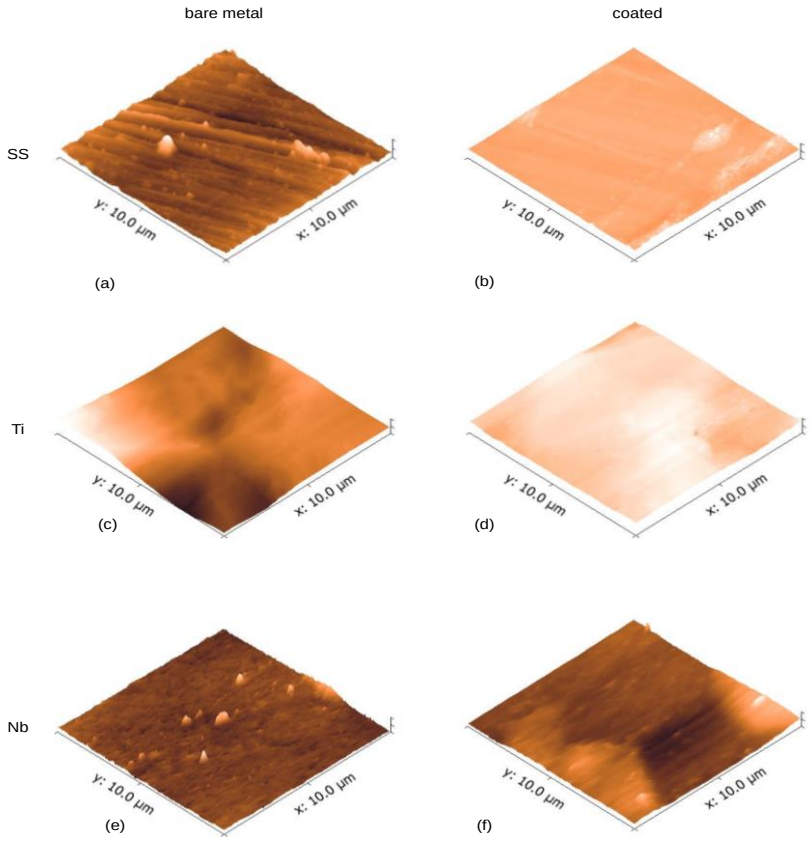

Figure 7.3 AFM images of uncoated and a-C:H coated Stainless Steel (SS), Titanium (Ti) and Niobium (Nb) surfaces.

Table 7.1 Mean values of the extracted nanotribological characteristics of bare metal (uncoated) and a-C:H coated surfaces.

Material	Roughness [nm]		COF [-]		Maximum residual depth [nm]	
	Uncoated	Coated	Uncoated	Coated	Uncoated	Coated
Stainless Steel (SS)	12.9±1.4	6.8±0.8	0.17±0.03	0.15±0.02	339±12	243±38
Titanium (Ti)	430.8±227.1	250.5±46.5	0.36±0.06	0.35±0.06	1570±215	1387±118
Niobium (Nb)	17.0±7.0	14.5±3.4	0.41±0.11	0.20±0.02*	2872±342	1866±283

***corresponds to the COF before film failure, i.e. in the 10-100mN range.**

X-ray reflectivity data and model fit on a hydrogenated amorphous carbon coated silicon substrate, for density and thickness determination purposes, are shown in Figure 7.1(a). The graph demonstrates that the experimental data are well fit by the model and the resulting coating thickness was quantified at $\sim 40\ \mathrm{nm}$ with a density value of $\sim 1.7\ \mathrm{g\ cm^{-3}}$.

7.3.2 Nanomechanical response

The local mechanical properties of the metallic substrate samples were probed through nanoindentation. Typical $\mathrm{P-h}$ curves shown in Figure 7.4(a) were collected during load–displacement tests to a maximum load of $100\ \mathrm{mN}$ and loading/unloading rate of $10\ \mathrm{mNs^{-1}}$. All the derived nanomechanical parameters are summarized in Table 7.2. The corresponding data for the uncoated SS, Ti and Nb surfaces are in line with the nominal mechanical properties of these materials, previously reported in literature [[190]]. The higher u_p values of Nb and Ti, compared to the SS alloy, denote materials with a greater ability to dissipate energy in plastic deformations and thus less vulnerable to fracture and fatigue failure. Stainless steels are nowadays being replaced by more corrosion and fatigue resistant alloys, in permanent implants, such as Ti and $\mathrm{Ti-Nb}$ alloys. Nevertheless, the low cost of stainless steels has maintained their application in many temporary orthopedic devices, such as bone screws, bone plates, intramedullary nails and rods [[190]].

The nanoindentation platform was also used to study the comparative creep responses between the three substrate samples and the resulting displacement-time data are shown in Figure 7.4(b). Creep, which relates to the tendency of materials to deform in time under a persisting stress, even below the yield strength of the material, is a typical response for all solids which might eventually lead to failure. The Nb and Ti samples

showed comparable creep deformations both in the primary and secondary stage. In contrast, SS quickly moves from a non-linear to a linear behavior demonstrating the least indentation creep response. The superior creep response experienced by SS is in part related to the higher hardness of the material which leads to a lower percentage of plastic deformation and subsequently less susceptibility to time dependent deformation. Nevertheless, the nanoscale deformations for all materials which get saturated after several seconds are of secondary importance for body temperature applications.

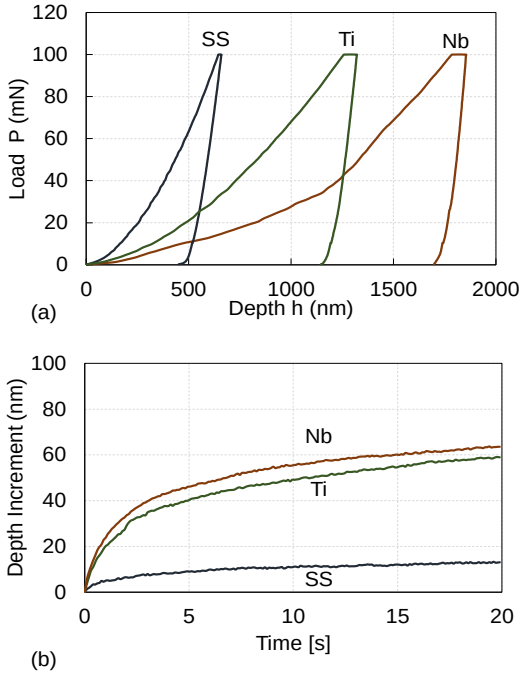

Figure 7.4 Nano indentation response of bare metal SS, Ti and Nb surfaces: (a) load–displacement and (b) creep data.

Table 7.2 Nanomechanical characteristics of bare metal SS, Ti and Ni surfaces.

	Max.depth (nm)	Plastic depth (nm)	Reduced elastic modulus (GPa)	Hardness (GPa)	Plastic work (nJ)	Elastic work (nJ)	Plastic work ratio (%)
Stainless Steel (SS)	667±12	557±14	233.6±5.0	12.3±0.6	18.1±1.2	7.2±0.1	71.5±1.6
Titanium (Ti)	1308±106	1233±104	131.6±18.0	2.7±0.5	45.4±5.0	6.2±0.2	87.9±1.0
Niobium (Nb)	1763±155	1699±155	105.1±13.3	1.4±0.3	63.5±10.8	5.7±0.2	91.6±1.2

7.3.3 Nanotribological response

The nanotribological characteristics of the bare metal and a $-$ C: H coated surfaces have been studied using nanoscratch testing. The nanoscratch responses of the SS, Ti and Nb surfaces and the evolution of friction coefficient are shown in Figure 7.5. In general, SS

shows smooth depth and COF responses with scratch distance due to the flat surface finish and nanoscale roughness whereas the native surfaces of Ti and Nb lead to fluctuating responses; nevertheless, the mean response trends of all materials are similar. The response of on-load depth and residual depth with scratch distance increases for all specimens in response to the gradual increase of the normal applied load (Figure 7.2(a)). As expected, the on-load depth profile of the various materials investigated herein scales with their hardness (denoting resistance to penetration) whereas the residual depth scales with the plastic work ratio which quantifies the tendency of the material to dissipate energy in the form of plastic deformations (see Table 7.1); Nb demonstrates the highest plastic capacity and lowest hardness followed by Ti and then SS. The steady state friction coefficient of the SS substrate is low, $\mu = 0.17 \pm 0.03$, in contrast to higher values calculated for Ti ($\mu = 0.36 \pm 0.06$) and Nb ($\mu = 0.41 \pm 0.11$). The COF values reported herein and in Table 7.1 reflect the average values for normal loads in the $1 - 100$ mN range.

The effect of $a-C:H$ coating on the nanotribological characteristics of the metallic surfaces are shown in Figures 7.6 – 7.8. Figure 7.6, in particular, demonstrates the capacity of the nanoscale film to reduce the plastic deformation and wear of the bare metal surfaces; the reduction being more evident in the case of SS. In all cases the deposited film improved the tribological performance of the metal surfaces reducing the residual depth imprint: 28% reduction for SS, 12% for Ti and 35% for Nb. The interatomic bonds developing between the SS/Ti crystals and the $a-C:H$ coating, compose stable structures with minor reduction in friction coefficient (Figure 7.7). On the contrary, Nb demonstrated significant reduction in COF before the associated critical load (~ 100 mN) that led to film failure and delamination (see Figure 7.8(f)) a result associated with its highest plastic deformation and lowest abrasion resistance. The extracted nanotribological characteristics for all tested uncoated and $a-C:H$ coated surfaces, are listed in Table 7.1.

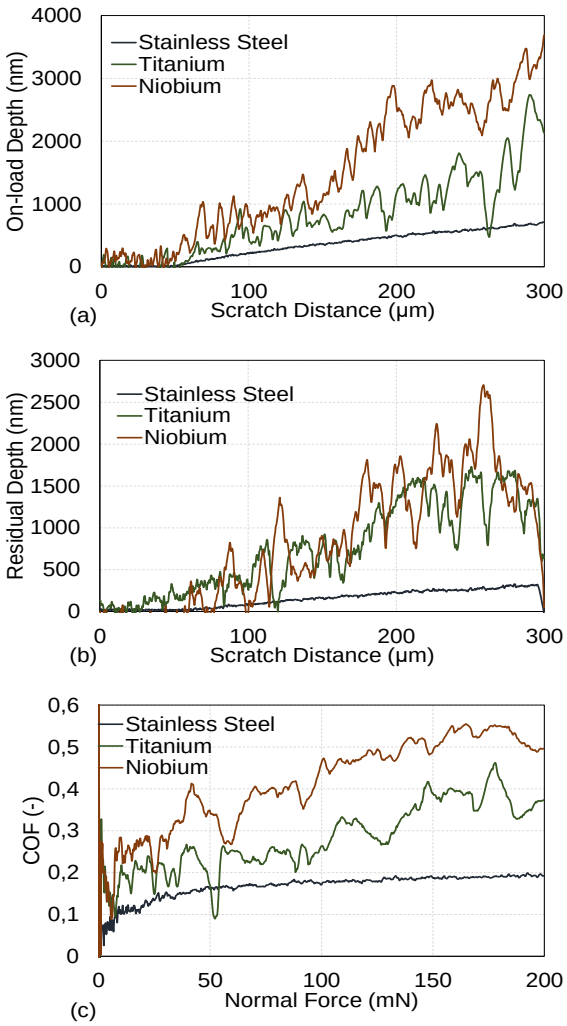

Figure 7.5 Nanoscratch responses of SS, Ti and Nb surfaces: (a) on load depth profile, (b) residual depth profile and (c) COF evolution with applied normal load.

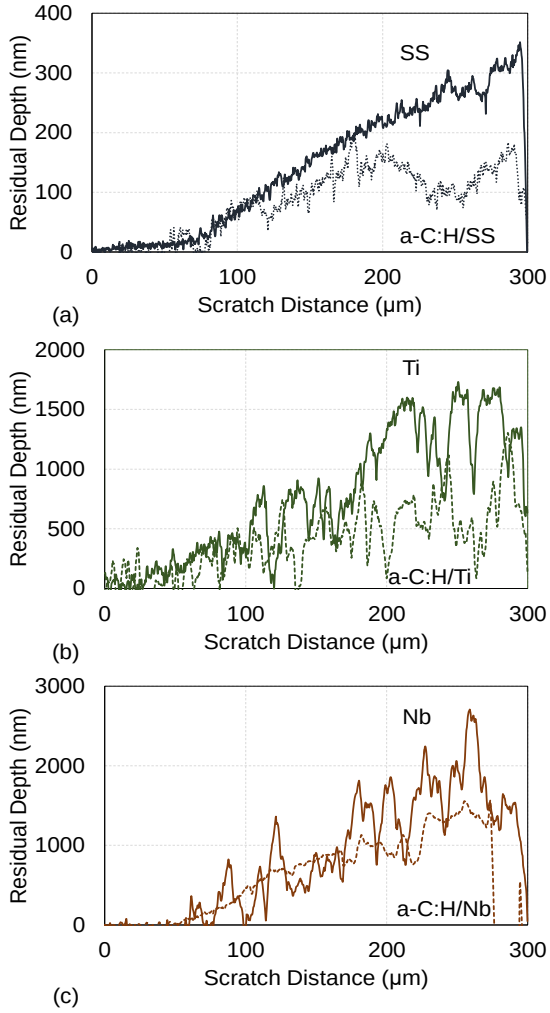

Figure 7.6 Effect of a-C:H coating on the residual depth response of (a) SS, (b) Ti and (c) Nb metals.

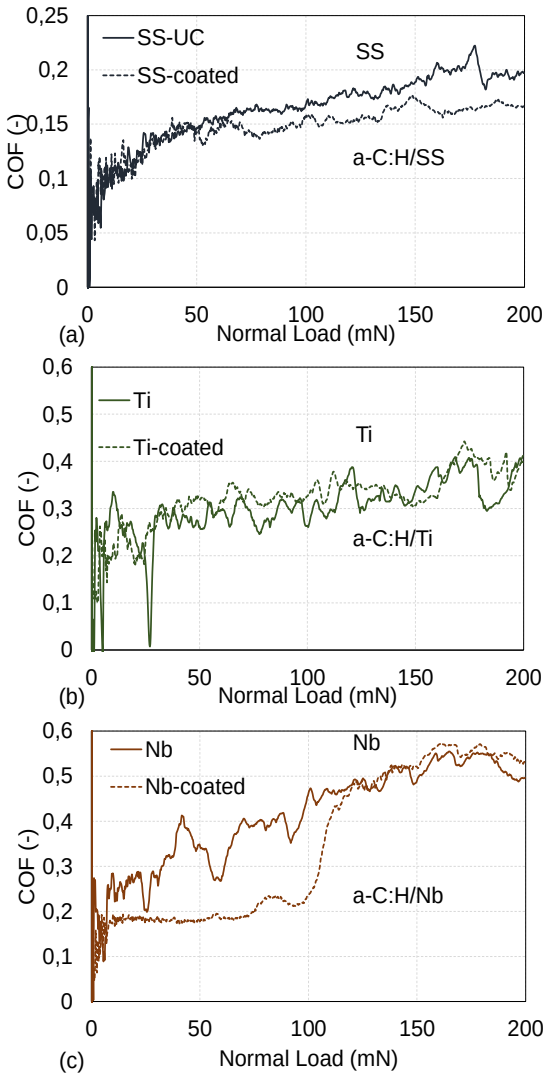

Figure 7.7 Effect of a-C:H coating on the COF response of (a) SS, (b) Ti and (c) Nb metals.

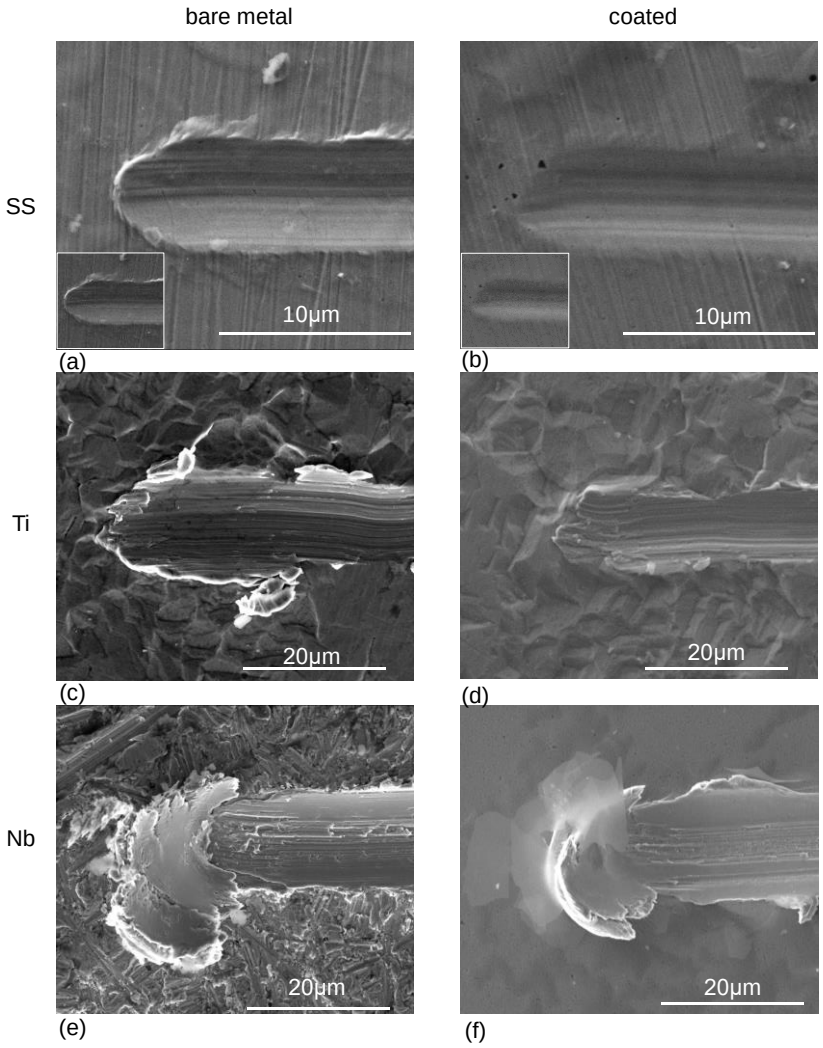

Figure 7.8 SEM images of residual scratched surfaces for the bare metal ((a), (c) and (e)) and a-C:H coated ((b), (d) and (f)) SS, Ti and Nb surfaces. Insets in (a) and (b) show the residual scratches at the same magnification (x6000) as the rest of the images for comparison purposes.

Figure 7.8 shows SEM images of the residual imprints left on the surface of the scratched specimens. By comparing the images of the coated metals (right column) versus the bare metal responses (left column), one can notice the reduction in the size of the residual mark and wear volume, in line with the residual depth results presented in Figure 7.6. These enhancements are evident in all specimens irrespective of whether the surfaces have been polished or left in their as-delivered state. The improvements in the tribomechanical response can be attributed in part to the reduction of friction between the indenter and the tested materials (Figure 7.7) and in part to the redistribution of stresses caused by the introduction of a hard, protective coating. The relatively uniform

plastic deformations imparted on the a − C: H coated SS and Ti substrates indicate their enhanced tribomechanical response (Figures 7.8a-b and 7.8c-d). Surface damage can be observed for Nb substrate at late stages of the scratch distance which correlates with a critical load for film failure, also evident from a discontinuity in the COF evolution (Figure 7.7(c)). As the contact load increases, plastic deformations are observed on the film followed by coating failure and delamination (Figure 7.8(f)).

7.4 Towards application steps

a − C: H can be coated on various components found application on aerospace engineering, automobile industry, manufacturing industry, textile industry, food packaging and biomedical field. For most occasions a reduced friction is very important property. It allows decrease to the resistance of sliding and hence reduction of energy losses as well as decrease of material losses and emmision of dangerous gases. In Figure 7.9 one can see cobalt chromium stent for vascular applications coated with a − C: H. The excellent mechanical and tribological properties of a − C: H, as well as its good adherence and haemocompatibility (e.g., prevention of thrombus formation and restenosis [191–193]) is the key issues to apply a − C: H on vascular stents. At this first step investigation it is evidence that only few cracks were found on the a − C: H coated stent surface after pressure deformation, subsequently quarantee more life adhesion (see Fig. 7.9).

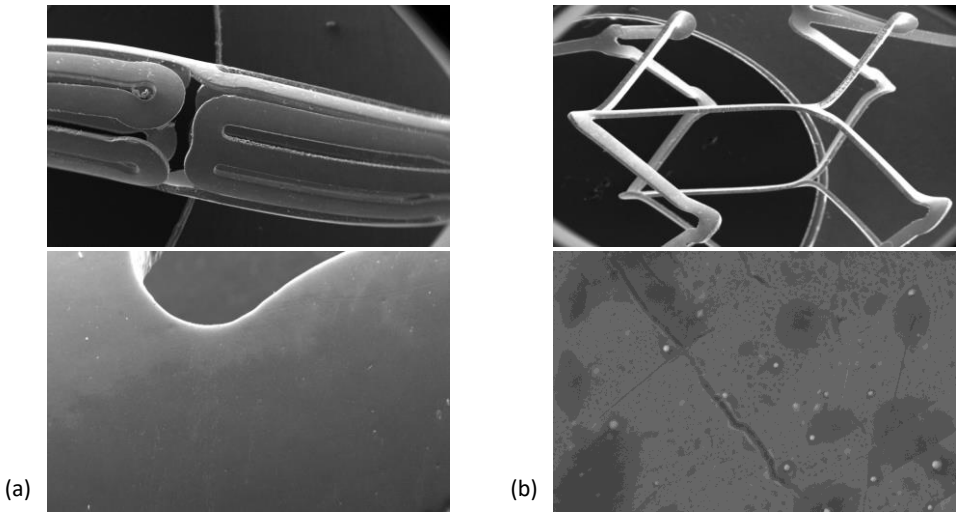

Figure 7.9 SEM micrographs of cobalt chromium stent obtained after coated with a-C:H. (a) unstrained stent surface; and (b) fractured stent surface with line-crack markings formed after expanding stent structure at 10 atm.

7.5 Conclusions

Plasma-enhanced chemical vapor deposition has been effectively employed for depositing nanoscale $a-C:H$ on SS, Ti and Nb plates. It is concluded that:

- The deposition of even a $40nm$ thick film improves the tribomechanical response of these metallic surfaces as evidenced through nanotribomechanical tests.
- Residual imprints and wear volumes have been reduced which can be attributed in part to a slight reduction in the COF and a contact stress redistribution caused by the deposition of a hard, protective surface.
- Despite the fluctuations of load during the tribomechanical testing of metallic surfaces left in their as-delivered state (non-polished), tribomechanical improvements can be observed on all specimens which suggest that the efficiency of $a-C:H$ coating is irrespective of whether the metallic surfaces are mirror polished or left in their native rough state.
- Hydrogenated amorphous carbon presents a promising material for serving as a protective coating on metallic implants.

CHAPTER 8 Concluding Remarks

8.1 Summary of results

This thesis investigated how hydrogen-free (DLC: Ag and DLC: Mo) and hydrogenated (a − C: H: Ag and a − C: H: Ti) amorphous carbon metal films can be designed to meet ductility and toughness requirements under the action of indentation and scratching at ambient temperature and low loading rates. The behavior of a composite material is a function of their characteristics, like, the properties of the constituent phases, phase amounts, geometrical characteristics of the dispersed phase, interface bonds - either between the matrix and the dispersed phase or between the whole film with the substrate material), and internal residual stresses. Taking into account the above principles and having implemented a complete synthesis and characterization scheme, the main conclusions from the studies presented herein follow.

8.1.1 Hydrogen-free amorphous carbon metal films

- Using Pulsed Excimer Laser Deposition and subsequently controlling the laser wavelength, and energy density, it was possible to grow DLC: Ag and DLC: Mo with significant proportion of hard sp^3 at. % compared to similar films grown by Pulsed Laser Deposition using an Nd: YAG laser source.
- The major mechanism that drop hardness and residual stresses, hence increase the scratch resistance of hydrogen-free DLC films is the drop of sp^3 at. % that decreases by the incorporation of even dispersed carbide ceramic phases (here MoC) or inert metals (here Ag).
- For both materials the enhancement of mechanical toughness increases by raising metal concentration within the hydrogen-free DLC structure. Moreover, the scratch resistant of such thin film alloy systems is found to be strongly dependent to the metal content, where too much metal led to a film system with excess deformation under scratch.
- The increase of metal atomic fraction drives the graphitization process, approximately having an average rate of about 10 at. % of sp^3 reduction for every 1 at. % of metal (see Fig. 5.6). Nevertheless, the character of particulate

matter is still a topic of future investigation, as the type and size distribution of the nanoparticles may influence the drop rate of sp^3.

- Also the formation of robust carbide bonds within DLC: Mo structure, enhances even more the scratch resistance compared to DLC: Ag films, due to its ability to act as an obstacle and mechanically interlock the propagation of cracks, deformation, buckling and eventual delamination.
- As friction force/friction coefficient is a parameter that were affected from both increased roughness or once from the increase of carbide compounds when existent, the ability to decrease friction coefficient seems to be a difficult task and strongly dependent on synthesis process.

8.1.2 Hydrogenated amorphous carbon metal films

- A novel PECVD/PVD system has been presented that can deliver a-C:H:Me nanocmpomposite films with tunable matrix, metal type, content and size. The parameters that affect the ion beam have been studied and the conclusions are: a) The gas flow should be kept at small concentrations inside the discharge tube (< 8 sccm). This provides source stability and ion beam efficiency for long lasting depositions. We here kept gas flow at 6.5 sccm. b) A film with a desirable density and thickness is achieved for RF power at 200W, beam energy at 150V and gas flow at $6/0.5$ sccm for methane and argon gases respectively.

- The nanoparticle source and in particular the size and number of metallic (Ag and/or Ti) NPs have been calibrated in order to quantify NPs characteristics and control their deposition during film growth. Microscopic results showed that NPs size and shape can be well controlled and defined through mesoQ Mass filter as experimental particles size/shape found to be in a good agreement with set MesoQ nominal values and TEM imaging results. Moreover, the increase of deposition time increases, as expected, the amount of NPs on the substrate material.

- Using the above experimental process and characterization results metal-carbon composite materials with predetermined density and thickness for $a-C:H$ matrix as well as phase amount, size and dispersion for metallic nanoparticles were prepared. For specific conditions chosen to prepare the matrix for

composites, hydrogen content of about $20-25\%$, and sp^3content of about 50% was indirectly estimated through literature previous Raman studies [32,65,169]. Controlling the size, number and dispersion of metallic NPs composite of the sort of $a-C:H:Ag$ and $a-C:H:Ti$ – have been synthesized by sequential deposition of hybrid deposition PECVD/PVD technology both showing increase mechanical resistance to scratch compared with pure $a-C:H$ matrix.

- The mechanical and tribological performance of $a-C:H$ films was also tested on three metallic implants i.e, SS, Ti and Nb. For all coated substrates results showed improved tribological resistance with low friction coefficient.
- Since $a-C:H$ films are known to be biocompatible having low wear rates, here a first step investigation proved its good adherence on cobalt chromium stent and subsequently a promising long life adhesion.

8.2 Future directions

From the above studies it is clear that $a-C:$ and $a-C:H:Me$ films hold great promise for a variety of applications and further research needs to be invested.

8.2.1 From a materials synthesis perspective

There is a need to further reduce the cost of coatings, increase their quality, and uniformity under industrial large-scale production through the development of synthesis procedures. In particular, these indicates the need to develop powerful, low temperature processes which are insensitive to abrupt changes. Form our side this effort could be implemented by investing to the potential capabilities of the new hybrid PECVD/PVD deposition technology. The ability to produce various types of $a-C:H/a-C:H:Me$ films with controlled compositional/chemical characteristics and moreover at low temperature depositions would allow us to build nanostructured materials with multifunctional applications. Such low temperature processes would also deem important for the synthesis of films on various types of substrate like metals, ceramics and polymers, expanding as well their applicability potential and lowering cost. Moreover the need to further reduce the roughness of $a-C:H/a-C:H:Me$ coatings, to decrease their friction coefficient and thus their scratch length strength, would be another challenge to invest on synthesis procedure. This idea is well supported from the

conclusions of our previous studies. Another one challenge still the better understanding of working operation of the hybrid PECVD/PVD deposition technology so to increase its working stability under long lasting operations. Although an effort to understand its working principles as well as growth of $a-C:H:Ag/a-C:H:Ti$ films were completed, some limitations that affect the efficiency/stability of ion beam have been noted. One of this is the decrease of deposition rate - resulting by increasing the amount of work/power - that may affect either the increase of pressure within the tube and indirectly the decrease of amount of species that pull out of the plasma, or the chemistry of deposited species and indirectly the mixture of ions that are accelerated towards the substrate material. A key to this problem might be the decrease of temperature within the discharged tube something would enable the decrease of pressure. This idea follows the ideal gas law where pressure is proportional to temperature according to the relationship $PV = nRT$ which is also valid when the pressure of gas is low.

8.2.2 From a materials composition perspective

This thesis dealt with the design route to get tougher $a-C$ films brought by the addition of metallic elements and tested under low loading rates and ambient temperature using nanoindentation and scratch techniques. However, as many applications of $a-C$ films, like cutting tools, aerospace and aircraft, require films refractory under high temperature and high loading rates, we raise a point of testing the already prepared materials using high temperature and high loading rates. A short description of both techniques - available on our nanoindentation platform as well - are subsequently presented.

Nanoindentation tests can be also conducted under high temperature conditions. This routine requires setup the experimental procedure as shown in Figure 8.1. Here the sample is mounted on a heater element stub which allows to the user to rise the temperature of the tested material up to 750^0C. The indenter is mounted on the pendulum with the same manner as for simple nanoindentation test but the whole pendulum system it is now protected by a suitable thermal shield to avoid high temperature interference to the rest instrumentation in the leftmost part (see Fig. 8.1). A power supply, temperature controller and thermocouples are needed to be installed on nanoindentation platform as well.

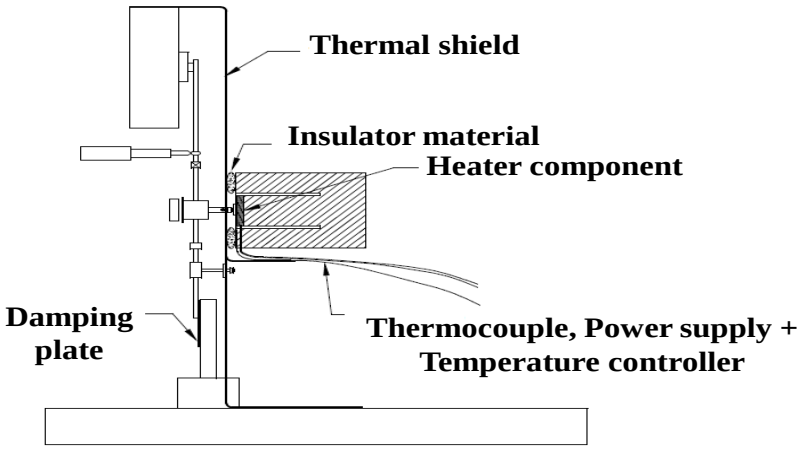

Figure 8.1 An assemblage of the experimental setup for hot stage nanoindentation.

Two kinds of experiments can be performed using the impact experimental setup, namely single impact and multiple-impact/fatigue tests (i.e., high loading rate cyclic stresses imposed on the material). The instrumentation setup includes a lab power supply, a control unit box and a propulsion impact solenoid installed permanently underneath of the pendulum. The communication is controlled by the suitable software installed on the nanoindentation platform. The procedure is as follows; the power applies voltage signal to the solenoid-magnet system to attract the pendulum, next the pendulum is released and loads the specimen with a certain loading rate , and, then the load and displacement of the indenter are measured via load and displacement sensors respectively. The information are collected and sent to the computer to display. A contact fatigue test or compression-compression test can be also performed on the same configuration. Here the indenter is fixed on the pendulum and the motion is carried out by the sample which is glued on a piezoelectric impact stub and it is on contact with the diamond probe. An additional generator box who supplies the signal for the movement of the piezoelectric material is also equipped with the nanoindentation platform. The output signal of the generator (amplitude and frequency) can be tuned manually and depending on the experimental circumstances. Such test can be used for example to simulate the contact fatigue on cutting tool surface.

Some inadequacies of $a-C$ films can be also eliminated by the incorporation of two additives (i.e., growth of three-phase composite film), for which the matrix is the $a-C$ film. The knowledge of already studied conventional metal alloys will enhance this idea. For example the addition of $AgCu$ (sterling silver) mixture within $a-C$ matrix

anticipate to increase not only toughness and scratch resistance but also corrosion resistance without depreciating toughness property.

$a-C$ matrix may be also reinforced by embedding metallic nanoparticles having different crystallographic structures (i.e., BCC, FCC, and HCP). Although a conclusion from so far studies was that the type of metal does not significantly influence the drop of sp^3 carbon state which is the major contributor to the decrease of hardness and increase in scratch resistance, this case in working this types of metals must be examined because the symmetry of the crystallographic structure affect the isotropic properties of materials and this may have impact on scratch resistant contributors. The ability to form nanocomposite $a-C$-metal films with well preselected size, shape and dispersion cab be also used to check the contribution of size to the reduction of hard sp^3 parameter.

REFERENCES

[1] P.I. Dolez, Nanomaterials Definitions, Classifications, and Applications, in: Nanoengineering, Elsevier, 2015: pp. 3–40. doi:10.1016/B978-0-444-62747-6.00001-4.

[2] P. Satalkar, B.S. Elger, D.M. Shaw, Defining Nano, Nanotechnology and Nanomedicine: Why Should It Matter?, Sci. Eng. Ethics. (2015). doi:10.1007/s11948-015-9705-6.

[3] H. Frey, H.R. Khan, Handbook of Thin-Film Technology, Springer Berlin Heidelberg, 2015. doi:10.1007/978-3-642-05430-3.

[4] P.M. Martin, Handbook of Deposition Technologies for Films and Coatings, Elsevier Inc., 2010.

[5] C.H. Woong, C. Jung-Hae, L. Kwang-Ryeol, A. Jae-Pyoung, O.K. Hwan, Structure and mechanical properties of Ag-incorporated DLC films prepared by a hybrid ion beam deposition system, Thin Solid Films. 516 (2007) 248–251. doi:10.1016/j.tsf.2007.06.154.

[6] C. Wang, X. Yu, M. Hua, Microstructure and mechanical properties of Ag-containing diamond-like carbon films in mid-frequency dual-magnetron sputtering, Appl. Surf. Sci. 256 (2009) 1431–1435. doi:10.1016/j.apsusc.2009.08.103.

[7] G.A. Tritsaris, C. Mathioudakis, P.C. Kelires, E. Kaxiras, Optical and elastic properties of diamond-like carbon with metallic inclusions: A theoretical study, J. Appl. Phys. 112 (2012) 103503. doi:10.1063/1.4765721.

[8] J. Cui, L. Qiang, B. Zhang, X. Ling, T. Yang, J. Zhang, Mechanical and tribological properties of Ti-DLC films with different Ti content by magnetron sputtering technique, Appl. Surf. Sci. 258 (2012) 5025–5030. doi:10.1016/j.apsusc.2012.01.072.

[9] L. Qiang, B. Zhang, Y. Zhou, J. Zhang, Improving the internal stress and wear resistance of DLC film by low content Ti doping, Solid State Sci. 20 (2013) 17–22. doi:10.1016/j.solidstatesciences.2013.03.003.

[10] X.S. Tang, H.J. Wang, L. Feng, L.X. Shao, C.W. Zou, Mo doped DLC nanocomposite coatings with improved mechanical and blood compatibility properties, Appl. Surf. Sci. 311 (2014) 758–762. doi:10.1016/j.apsusc.2014.05.155.

[11] J. Robertson, Diamond-like amorphous carbon, Mater. Sci. Eng. R Reports. 37 (2002) 129–281. doi:10.1016/S0927-796X(02)00005-0.

[12] A.C. Ferrari, J. Robertson, Resonant Raman spectroscopy of disordered, amorphous, and diamondlike carbon, Phys. Rev. B. 64 (2001) 75414. doi:10.1103/PhysRevB.64.075414.

[13] J. Robertson, Properties of diamond-like carbon, Surf. Coatings Technol. 50 (1992) 185–203. doi:10.1016/0257-8972(92)90001-Q.

[14] Y. Lifshitz, Diamond-like carbon — present status, Diam. Relat. Mater. 8 (1999) 1659–1676. doi:10.1016/S0925-9635(99)00087-4.

[15] S. Xu, D. Flynn, B.K. Tay, S. Prawer, K.W. Nugent, S.R.P. Silva, Y. Lifshitz, W.I. Milne, Mechanical properties and Raman spectra of tetrahedral amorphous carbon films with high sp 3 fraction deposited using a filtered cathodic arc, Philos. Mag. Part B. 76 (1997) 351–361. doi:10.1080/01418639708241099.

[16] K. Baba, R. Hatada, S. Flege, W. Ensinger, Y. Shibata, J. Nakashima, T. Sawase, T. Morimura, Preparation and antibacterial properties of Ag-containing diamond-like carbon films prepared by a combination of magnetron sputtering and plasma source ion implantation, Vacuum. 89 (2013) 179–184. doi:10.1016/j.vacuum.2012.04.015.

[17] M. Venkatesh, S. Taktak, E.I. Meletis, Characterization of nanocomposite a-C:H/Ag thin films synthesized by a hybrid deposition process, Phys. Met. Metallogr. 116 (2015) 781–790. doi:10.1134/S0031918X15080177.

[18] Y. Wu, J. Chen, H. Li, L. Ji, Y. Ye, H. Zhou, Preparation and properties of Ag/DLC nanocomposite films fabricated by unbalanced magnetron sputtering, Appl. Surf. Sci. 284 (2013) 165–170. doi:10.1016/j.apsusc.2013.07.074.

[19] R. Delmdahl, The excimer laser: Precision engineering, Nat. Photonics. 4 (2010) 286–286. doi:10.1038/nphoton.2010.106.

[20] R. Delmdahl, R. Pätzel, Excimer laser technology trends, J. Phys. D. Appl. Phys. 47 (2014) 34004. doi:10.1088/0022-3727/47/3/034004.

[21] D.R. McKenzie, Tetrahedral bonding in amorphous carbon, Reports Prog. Phys. 59 (1996). doi:10.1088/0034-4885/59/12/002.

[22] J. Robertson, Amorphous carbon, Adv. Phys. 35 (1986) 317–374. doi:10.1080/00018738600101911.

[23] C. Charitidis, S. Logothetidis, M. Gioti, A comparative study of the nanoscratching behavior of amorphous carbon films grown under various deposition conditions, Surf. Coatings Technol. 125 (2000) 201–206. doi:10.1016/S0257-8972(99)00546-0.

[24] S. Logothetidis, Haemocompatibility of carbon based thin films, Diam. Relat. Mater. 16 (2007) 1847–1857. doi:10.1016/j.diamond.2007.05.012.

[25] J. Hu, P. Yang, C.M. Lieber, Nitrogen-driven sp 3 to sp 2 transformation in carbon nitride materials, Phys. Rev. B. 57 (1998) R3185–R3188. doi:10.1103/PhysRevB.57.R3185.

[26] M.A. Tamor, W.C. Vassell, K.R. Carduner, Atomic constraint in hydrogenated "'diamond-like'" carbon, Appl. Phys. Lett. 58 (1991) 592–594. doi:10.1063/1.104597.

[27] P. Koidl, C. Wild, B. Dischler, J. Wagner, M. Ramsteiner, Plasma Deposition, Properties and Structure of Amorphous Hydrogenated Carbon Films, Mater. Sci. Forum. 52–53 (1990) 41–70. doi:10.4028/www.scientific.net/MSF.52-53.41.

[28] M.C. Polo, J.L. Andújar, A. Hart, J. Robertson, W.I. Milne, Preparation of tetrahedral amorphous carbon films by filtered cathodic vacuum arc deposition, Diam. Relat. Mater. 9 (2000) 663–667. doi:10.1016/S0925-9635(99)00339-8.

[29] I. Hiroshi, F. Kenji, H. Shinya, S. Shinji, T. Satoru, Y. Minoru, E. Masayoshi, Tetrahedral Amorphous Carbon Films By Filtered Cathodic Vacuum-Arc Deposition For Air-Bearing-Surface Overcoat, Jpn. J. Appl. Phys. 42 (2003) 2824–2828. doi:10.1143/JJAP.42.2824.

[30] F. Garrelie, A.. Loir, C. Donnet, F. Rogemond, R. Le Harzic, M. Belin, E. Audouard, P. Laporte, Femtosecond pulsed laser deposition of diamond-like

carbon thin films for tribological applications, Surf. Coatings Technol. 163 (2003) 306–312. doi:10.1016/S0257-8972(02)00481-4.

[31] A. Erdemir, C. Donnet, Tribology of diamond-like carbon films: recent progress and future prospects, J. Phys. D. Appl. Phys. 39 (2006) R311–R327. doi:10.1088/0022-3727/39/18/R01.

[32] C. Casiraghi, A.C. Ferrari, J. Robertson, Raman spectroscopy of hydrogenated amorphous carbons, Phys. Rev. B - Condens. Matter Mater. Phys. 72 (2005) 1–14. doi:10.1103/PhysRevB.72.085401.

[33] A.C. Ferrari, A. Libassi, B.K. Tanner, V. Stolojan, J. Yuan, L.M. Brown, S.E. Rodil, B. Kleinsorge, Density , sp 3 fraction , and cross-sectional structure of amorphous carbon films determined by x-ray reflectivity and electron energy-loss spectroscopy, Phys. Rev. B - Condens. Matter Mater. Phys. 62 (2000) 89–103.

[34] M. Weiler, S. Sattel, K. Jung, H. Ehrhardt, V.S. Veerasamy, J. Robertson, Highly tetrahedral, diamond-like amorphous hydrogenated carbon prepared from a plasma beam source, Appl. Phys. Lett. 64 (1994) 2797–2799. doi:10.1063/1.111428.

[35] M. Weiler, K. Lang, E. Li, J. Robertson, Deposition of tetrahedral hydrogenated amorphous carbon using a novel electron cyclotron wave resonance reactor, Appl. Phys. Lett. 72, 1314. (1998). doi:10.1063/1.121069.

[36] S. V. Hainsworth, N.J. Uhure, Diamond like carbon coatings for tribology: production techniques, characterisation methods and applications, Int. Mater. Rev. 52 (2007) 153–174. doi:10.1179/174328007X160272.

[37] T. Hasebe, A. Hotta, H. Kodama, A. Kamijo, K. Takahashi, T. Suzuki, Recent advances in diamond-like carbon films in the medical and food packing fields, New Diam. Front. Carbon Technol. 17 (2007) 263–279.

[38] N. Boutroy, Y. Pernel, J.M. Rius, F. Auger, H.J. von Bardeleben, J.L. Cantin, F. Abel, A. Zeinert, C. Casiraghi, A.C. Ferrari, J. Robertson, Hydrogenated amorphous carbon film coating of PET bottles for gas diffusion barriers, Diam. Relat. Mater. 15 (2006) 921–927. doi:10.1016/j.diamond.2005.10.049.

[39] A.C. Ferrari, Diamond-like carbon for magnetic storage disks, Surf. Coatings

Technol. 180–181 (2004) 190–206. doi:10.1016/j.surfcoat.2003.10.146.

[40] R. Hauert, A review of modified DLC coatings for biological applications, Diam. Relat. Mater. 12 (2003) 583–589. doi:10.1016/S0925-9635(03)00081-5.

[41] C.A. Love, R.B. Cook, T.J. Harvey, P.A. Dearnley, R.J.K. Wood, Diamond like carbon coatings for potential application in biological implants—a review, Tribol. Int. 63 (2013) 141–150. doi:10.1016/j.triboint.2012.09.006.

[42] F.M. Kimock, B.J. Knapp, Commercial applications of ion beam deposited diamond-like carbon (DLC) coatings, Surf. Coatings Technol. 56 (1993) 273–279. doi:10.1016/0257-8972(93)90261-L.

[43] F. Piazza, D. Grambole, D. Schneider, C. Casiraghi, A.C. Ferrari, Protective diamond-like carbon coatings for future optical storage disks, Diam. Relat. Mater. 14 (2005) 994–999. doi:10.1016/j.diamond.2004.12.028.

[44] M.A. Tamor, D.R. McKenzie, D. Muller, B.A. Pailthorpe, Y. Lifshitz, S.R. Kasi, J.W. Rabalais, J. Robertson, C.A. Davis, P.C. Kelires, Synthesis, Properties and Applications of Superhard Amorphous Coatings, MRS Proc. 383 (1995) 423. doi:10.1557/PROC-383-423.

[45] A.C. Ferrari, S.E. Rodil, J. Robertson, W.I. Milne, Is stress necessary to stabilise sp3 bonding in diamond-like carbon?, Diam. Relat. Mater. 11 (2002) 994–999. doi:10.1016/S0925-9635(01)00705-1.

[46] A.C. Ferrari, B. Kleinsorge, N.A. Morrison, A. Hart, V. Stolojan, J. Robertson, Stress reduction and bond stability during thermal annealing of tetrahedral amorphous carbon, J. Appl. Phys. 85 (1999) 7191. doi:10.1063/1.370531.

[47] C. Wang, X. Yu, M. Hua, Microstructure and mechanical properties of Ag-containing diamond-like carbon films in mid-frequency dual-magnetron sputtering, Appl. Surf. Sci. 256 (2009) 1431–1435. doi:10.1016/j.apsusc.2009.08.103.

[48] G.A. Tritsaris, C. Mathioudakis, P.C. Kelires, E. Kaxiras, Optical and elastic properties of diamond-like carbon with metallic inclusions: A theoretical study, J. Appl. Phys. 112 (2012) 103503. doi:10.1063/1.4765721.

[49] T. Le Huu, H. Zaidi, D. Paulmier, P. Voumard, Transformation of sp3 to sp2 sites

of diamond like carbon coatings during friction in vacuum and under water vapour environment, Thin Solid Films. 290–291 (1996) 126–130. doi:10.1016/S0040-6090(96)09198-5.

[50] Y. Liu, A. Erdemir, E.I. Meletis, An investigation of the relationship between graphitization and frictional behavior of DLC coatings, Surf. Coatings Technol. 86–87 (1996) 564–568. doi:10.1016/S0257-8972(96)03057-5.

[51] A. Erdemir, C. Bindal, J. Pagan, P. Wilbur, Characterization of transfer layers on steel surfaces sliding against diamond-like hydrocarbon films in dry nitrogen, Surf. Coatings Technol. 76–77 (1995) 559–563. doi:10.1016/0257-8972(95)02518-9.

[52] A. Erdemir, G.R. Fenske, Tribological Performance of Diamond and Diamondlike Carbon Films at Elevated Temperatures, Tribol. Trans. 39 (1996) 787–794. doi:10.1080/10402009608983596.

[53] V. Teixeira, P. Soares, A.J. Martins, J. Carneiro, F. Cerqueira, Nanocomposite Metal Amorphous-Carbon Thin Films Deposited by Hybrid PVD and PECVD Technique, J. Nanosci. Nanotechnol. 9 (2009) 4061–4066. doi:10.1166/jnn.2009.M11.

[54] V. Majji, T. Sukru, M. Efstathios, Synthesis of Ag-doped hydrogenated carbon thin films by a hybrid PVD–PECVD deposition process, Bull. Mater. Sci. 37 (2014) 1669–1676. doi:10.1007/s12034-014-0728-4.

[55] K. Gregorczyk, M. Knez, Hybrid nanomaterials through molecular and atomic layer deposition: Top down, bottom up, and in-between approaches to new materials, Prog. Mater. Sci. 75 (2016) 1–37. doi:10.1016/j.pmatsci.2015.06.004.

[56] H. Zoubos, L.E. Koutsokeras, D.F. Anagnostopoulos, E. Lidorikis, S.A. Kalogirou, A.R. Wildes, P.C. Kelires, P. Patsalas, Broadband optical absorption of amorphous carbon/Ag nanocomposite films and its potential for solar harvesting applications, Sol. Energy Mater. Sol. Cells. 117 (2013) 350–356. doi:10.1016/j.solmat.2013.06.019.

[57] V.S. Dhandapani, R. Subbiah, E. Thangavel, M. Arumugam, K. Park, Z.M. Gasem, V. Veeraragavan, D.E. Kim, Tribological properties, corrosion resistance

and biocompatibility of magnetron sputtered titanium-amorphous carbon coatings, Appl. Surf. Sci. 371 (2016) 262–274. doi:10.1016/j.apsusc.2016.02.194.

[58] P. Zhang, B.K. Tay, Y.B. Zhang, S.P. Lau, K.P. Yung, The reversible wettability of Ti containing amorphous carbon films by UV irradiation, Surf. Coatings Technol. 198 (2005) 184–188. doi:10.1016/j.surfcoat.2004.10.030.

[59] K.D. Bakoglidis, S. Schmidt, M. Garbrecht, I.G. Ivanov, J. Jensen, G. Greczynski, L. Hultman, Low-temperature growth of low friction wear-resistant amorphous carbon nitride thin films by mid-frequency, high power impulse, and direct current magnetron sputtering, J. Vac. Sci. Technol. A Vacuum, Surfaces, Film. 33 (2015) 05E112. doi:10.1116/1.4923275.

[60] R.J. Beane, Using the Scanning Electron Microscope for Discovery Based Learning in Undergraduate Courses, J. Geosci. Educ. 52 (2004) 250–253. doi:10.5408/1089-9995-52.3.250.

[61] D.B. Williams, C.B. Carter, The Transmission Electron Microscope, in: Transm. Electron Microsc., Springer US, Boston, MA, 2009: pp. 3–22. doi:10.1007/978-0-387-76501-3_1.

[62] M. Yasaka, X-ray thin-film measurement techniques, V. X-Ray Reflectivity Meas. Rigaku J. 26 (2010) 1–9. doi:10.1097/01.ss.0000026967.27546.82.

[63] Y. Waseda, E. Matsubara, K. Shinoda, Fundamental Properties of X-rays, in: X-Ray Diffr. Crystallogr., Springer Berlin Heidelberg, Berlin, Heidelberg, 2011: pp. 1–20. doi:10.1007/978-3-642-16635-8_1.

[64] S. Kobayashi, X-ray thin film measurements techniques IV in plane XRD measuremenst, Rigaku J. 26 (2010) 3–11.

[65] A.C. Ferrari, A. Libassi, B.K. Tanner, V. Stolojan, J. Yuan, L.M. Brown, S.E. Rodil, B. Kleinsorge, J. Robertson, Density, sp3 fraction, and cross-sectional structure of amorphous carbon films determined by x-ray reflectivity and electron energy-loss spectroscopy, Phys. Rev. B - Condens. Matter Mater. Phys. 62 (2000) 11089–11103. doi:10.1103/PhysRevB.62.11089.

[66] Y. Huai, M. Chaker, J. Broughton, E. Gat, Study of density in pulsed-laser

deposited amorphous carbon films using x-ray reflectivity, Appl. Phys. Lett. 65 (1994) 830–833. doi:10.1063/1.112245.

[67] P. van der Heide, X-Ray Photoelectron Spectroscopy, John Wiley & Sons, Inc., Hoboken, NJ, USA, 2011. doi:10.1002/9781118162897.

[68] A.C. Fischer-Cripps, Contact Mechanics, in: 2004: pp. 1–20. doi:10.1007/978-1-4757-5943-3_1.

[69] W.C. Oliver, G.M. Pharr, An improved technique for determining hardness and elastic modulus using load and displacement sensing indentation experiments, J. Mater. Res. 7 (1992) 1564–1583. doi:10.1557/JMR.1992.1564.

[70] K.D. Bouzakis, M. Pappa, G. Skordaris, E. Bouzakis, S. Gerardis, Correlation between PVD coating strength properties and impact resistance at ambient and elevated temperatures, Surf. Coatings Technol. 205 (2010) 1481–1485. doi:10.1016/j.surfcoat.2010.07.055.

[71] G. Constantinides, Z.I. Kalcioglu, M. McFarland, J.F. Smith, K.J. Van Vliet, Probing mechanical properties of fully hydrated gels and biological tissues, J. Biomech. 41 (2008) 3285–3289. doi:10.1016/j.jbiomech.2008.08.015.

[72] B.D. Beake, S.R. Goodes, B. Shi, Nanomechanical and nanotribological testing of ultra-thin carbon-based and MoST films for increased MEMS durability, J. Phys. D. Appl. Phys. 42 (2009) 65301. doi:10.1088/0022-3727/42/6/065301.

[73] G.M. Wilson, J.F. Smith, J.L. Sullivan, A DOE nano-tribological study of thin amorphous carbon-based films, Tribol. Int. 42 (2009) 220–228. doi:10.1016/j.triboint.2008.06.006.

[74] W.C. Oliver, G.M. Pharr, Nanoindentation in materials research: Past, present, and future, MRS Bull. 35 (2011) 897–907. doi:10.1557/mrs2010.717.

[75] J. Menčík, L.H. He, M. V. Swain, Determination of viscoelastic–plastic material parameters of biomaterials by instrumented indentation, J. Mech. Behav. Biomed. Mater. 2 (2009) 318–325. doi:10.1016/j.jmbbm.2008.09.002.

[76] S. Bec, A. Tonck, J.-M. Georges, E. Georges, J.-L. Loubet, Improvements in the indentation method with a surface force apparatus, Philos. Mag. A. 74 (1996) 1061–1072. doi:10.1080/01418619608239707.

[77] N. Fujisawa, M. V. Swain, Effect of unloading strain rate on the elastic modulus of a viscoelastic solid determined by nanoindentation, J. Mater. Res. 21 (2006) 708–714. doi:10.1557/jmr.2006.0087.

[78] J. Menčík, D. Munz, E. Quandt, E.R. Weppelmann, M. V. Swain, Determination of elastic modulus of thin layers using nanoindentation, J. Mater. Res. 12 (1997) 2475–2484. doi:10.1557/JMR.1997.0327.

[79] G. Constantinides, K.S. Ravi Chandran, F.J. Ulm, K.J. Van Vliet, Grid indentation analysis of composite microstructure and mechanics: Principles and validation, Mater. Sci. Eng. A. 430 (2006) 189–202. doi:10.1016/j.msea.2006.05.125.

[80] G. Constantinides, F.J. Ulm, The nanogranular nature of C-S-H, J. Mech. Phys. Solids. 55 (2007) 64–90. doi:10.1016/j.jmps.2006.06.003.

[81] W.C. Oliver, G.M. Pharr, An improved technique for determining hardness and elastic modulus using load and displacement sensing indentation experiments, J. Mater. Res., Vol. 7, No. 6. (1992). https://doi.org/10.1557/JMR.1992.1564.

[82] A.K. Bhattacharya, W.D. Nix, Analysis of elastic and plastic deformation associated with indentation testing of thin films on substrates, Int. J. Solids Struct. 24 (1988) 1287–1298. doi:10.1016/0020-7683(88)90091-1.

[83] G. Huajian, C. Cheng-Hsin, L. Jin, Elastic contact versus indentation modeling of multi-layered materials, Int. J. Solids Struct. 29 (1992) 2471–2492. doi:10.1016/0020-7683(92)90004-D.

[84] C.A. Clifford, Martin P Seah, Nanoindentation measurement of Young's modulus for compliant layers on stiffer substrates including the effect of Poisson's ratios., Nanotechnology. 20 (2009) 145708. doi:10.1088/0957-4484/20/14/145708.

[85] E. Barthel, A. Perriot, Elastic contact to a coated half-space - Effective elastic modulus and real penetration, J. Mater. Res. 19 (2004) 600–608. doi:10.1557/jmr.2004.19.2.600.

[86] D.B. Marshall, A.G. Evans, Measurement of adherence of residually stressed thin films by indentation. I. Mechanics of interface delamination, J. Appl. Phys. 56

(1984) 2632–2638. doi:10.1063/1.333794.

[87] B. Rother, D.A. Dietrich, Evaluation of coating-substrate interface strength by differential load feed analysis of load-indentation measurements, Thin Solid Films. 250 (1994) 181–186. doi:10.1016/0040-6090(94)90183-X.

[88] K.I. Schiffmann, Determination of fracture toughness of bulk materials and thin films by nanoindentation: comparison of different models, Philos. Mag. 91 (2011) 1163–1178. doi:10.1080/14786435.2010.487984.

[89] A.T. Akono, F.J. Ulm, Scratch test model for the determination of fracture toughness, Eng. Fract. Mech. 78 (2011) 334–342. doi:10.1016/j.engfracmech.2010.09.017.

[90] A.T. Akono, P.M. Reis, F.J. Ulm, Scratching as a fracture process: From butter to steel, Phys. Rev. Lett. 106 (2011) 2–5. doi:10.1103/PhysRevLett.106.204302.

[91] A.T. Akono, N.X. Randall, F.-J. Ulm, Experimental determination of the fracture toughness via microscratch tests: Application to polymers, ceramics, and metals, J. Mater. Res. 27 (2012) 485–493. doi:10.1557/jmr.2011.402.

[92] A.T. Akono, F.J. Ulm, Fracture scaling relations for scratch tests of axisymmetric shape, J. Mech. Phys. Solids. 60 (2012) 379–390. doi:10.1016/j.jmps.2011.12.009.

[93] B.D. Beake, G. a. Bell, S.R. Goodes, N.J. Pickford, J.F. Smith, Improved nanomechanical test techniques for surface engineered materials, Surf. Eng. 26 (2010) 37–49. doi:10.1179/174329409X451137.

[94] S. Bec, a. Tonck, J.-M. Georges, E. Georges, J.-L. Loubet, Improvements in the indentation method with a surface force apparatus, Philos. Mag. A. 74 (1996) 1061–1072. doi:10.1080/01418619608239707.

[95] P. Lemoine, J.P. Quinn, P.D. Maguire, J.F. Zhao, J.A. Mclaughlin, Intrinsic mechanical properties of ultra-thin amorphous carbon layers, 253 (2007) 6165–6175. doi:10.1016/j.apsusc.2007.01.028.

[96] W.C. Oliver, G.M. Pharr, Measurement of hardness and elastic modulus by instrumented indentation: Advances in understanding and refinements to methodology, J. Mater. Res. 19 (2004) 3–20. doi:10.1557/jmr.2004.19.1.3.

[97] K.J. Van Vliet, L. Prchlik, J.F. Smith, Direct measurement of indentation frame compliance, J. Mater. Res. 19 (2004) 325–331. doi:10.1557/jmr.2004.19.1.325.

[98] A. Gouldstone, H.J. Koh, K.Y. Zeng, A.E. Giannakopoulos, S. Suresh, Discrete and continuous deformation during nanoindentation of thin films, Acta Mater. 48 (2000) 2277–2295. doi:10.1016/S1359-6454(00)00009-4.

[99] W.W. Gerberich, J.C. Nelson, E.T. Lilleodden, P. Anderson, J.T. Wyrobek, Indentation induced dislocation nucleation: The initial yield point, Acta Mater. 44 (1996) 3585–3598. doi:10.1016/1359-6454(96)00010-9.

[100] G. Constantinides, E.C.C.M. Silva, G.S. Blackman, K.J. Van Vliet, Dealing with imperfection: Quantifying potential length scale artefacts from nominally spherical indenter probes, 18 (2007). doi:10.1088/0957-4484/18/30/305503.

[101] Y.L. Chiu, A.H.W. Ngan, Time-dependent characteristics of incipient plasticity in nanoindentation of a Ni3Al single crystal, Acta Mater. 50 (2002) 1599–1611. doi:10.1016/S1359-6454(02)00025-3.

[102] G. Matenoglou, G.A. Evangelakis, C. Kosmidis, S. Foulias, D. Papadimitriou, P. Patsalas, Pulsed laser deposition of amorphous carbon/silver nanocomposites, Appl. Surf. Sci. 253 (2007) 8155–8159. doi:10.1016/j.apsusc.2007.02.125.

[103] H.S. Zhang, J.L. Endrino, A. Anders, Comparative surface and nano-tribological characteristics of nanocomposite diamond-like carbon thin films doped by silver, Appl. Surf. Sci. 255 (2008) 2551–2556. doi:10.1016/j.apsusc.2008.07.193.

[104] A. Pardo, C. Gómez-Aleixandre, Wear Behavior of Plasma Assisted Chemical Vapor Deposited Nanocomposites Made of Metal Nanoparticles Embedded in a Hydrogenated Amorphous Carbon Matrix, Surf. Coatings Technol. 206 (2012) 3116–3124. doi:10.1016/j.surfcoat.2011.12.041.

[105] H. Zoubos, L.E. Koutsokeras, D.F. Anagnostopoulos, E. Lidorikis, S.A. Kalogirou, A.R. Wildes, P.C. Kelires, P. Patsalas, Broadband optical absorption of amorphous carbon/Ag nanocomposite films and its potential for solar harvesting applications, Sol. Energy Mater. Sol. Cells. 117 (2013) 350–356. doi:10.1016/j.solmat.2013.06.019.

[106] O. Garcia-Zarco, S.E. Rodil, M. a. Camacho-López, Deposition of amorphous

carbon–silver composites, Thin Solid Films. 518 (2009) 1493–1497. doi:10.1016/j.tsf.2009.09.092.

[107] R.J. Narayan, Pulsed laser deposition of functionally gradient diamondlike carbon–metal nanocomposites, Diam. Relat. Mater. 14 (2005) 1319–1330. doi:10.1016/j.diamond.2004.12.047.

[108] D. Briggs, M.P. Seah, eds., Practical Surface Analysis, Auger and X-ray Photoelectron Spectroscopy (Volume 1), First, Wiley, 1996.

[109] G. Constantinides, F.J. Ulm, The effect of two types of C-S-H on the elasticity of cement-based materials: Results from nanoindentation and micromechanical modeling, Cem. Concr. Res. 34 (2004) 67–80.

[110] M. Vandamme, C.A. Tweedie, G. Constantinides, F.-J. Ulm, K.J. Van Vliet, Quantifying plasticity-independent creep compliance and relaxation of viscoelastoplastic materials under contact loading, J. Mater. Res. 27 (2012) 302–312.

[111] I.N. Sneddon, Boussinesq's problem for a rigid cone, Math. Proc. Cambridge Philos. Soc. 44 (1948) 492–507.

[112] B.D. Beake, S.P. Lau, Nanotribological and nanomechanical properties of 5–80 nm tetrahedral amorphous carbon films on silicon, Diam. Relat. Mater. 14 (2005) 1535–1542. doi:10.1016/j.diamond.2005.04.002.

[113] B.D. Beake, a J. Harris, T.W. Liskiewicz, Review of recent progress in nanoscratch testing, Tribol. - Mater. Surfaces Interfaces. 7 (2013) 87–96. doi:10.1179/1751584X13Y.0000000037.

[114] B. Druz, E. Ostan, S. Distefano, A. Hayes, V. Kanarov, V. Polyakov, A. Rukovishnikov, N. Rossukanyi, A. Khomich, Diamond-like carbon films deposited using a broad, uniform ion beam from an RF inductively coupled CH4-plasma source, Diam. Relat. Mater. 7 (1998) 965–972. doi:10.1016/S0925-9635(97)00338-5.

[115] M. Chhowalla, J. Robertson, C.W. Chen, S.R.P. Silva, C.A. Davis, G.A.J. Amaratunga, W.I. Milne, Influence of ion energy and substrate temperature on the optical and electronic properties of tetrahedral amorphous carbon (ta-C)

films, J. Appl. Phys. 81 (1997) 139. doi:10.1063/1.364000.

[116] P. Patsalas, M. Handrea, S. Logothetidis, M. Gioti, S. Kennou, W. Kautek, A complementary study of bonding and electronic structure of amorphous carbon films by electron spectroscopy and optical techniques, Diam. Relat. Mater. 10 (2001) 960–964. doi:10.1016/S0925-9635(00)00480-5.

[117] N.T. Panagiotopoulos, E.K. Diamanti, L.E. Koutsokeras, M. Baikousi, E. Kordatos, T.E. Matikas, D. Gournis, P. Patsalas, Nanocomposite catalysts producing durable, super-black carbon nanotube systems: applications in solar thermal harvesting., ACS Nano. 6 (2012) 10475–85. doi:10.1021/nn304531k.

[118] S. Neuville, Carbon Structure Analysis With Differentiated Raman Spectroscopy, Lambert Academic Press, 2014.

[119] C.A. Davis, G.A.J. Amaratunga, K.M. Knowles, Growth Mechanism and Cross-Sectional Structure of Tetrahedral Amorphous Carbon Thin Films, Phys. Rev. Lett. 80 (1998) 3280–3283. doi:10.1103/PhysRevLett.80.3280.

[120] M. Fyta, P.C. Kelires, Stress variations near surfaces in diamond-like amorphous carbon, J. Non. Cryst. Solids. 266–269 (2000) 760–764. doi:10.1016/S0022-3093(99)00810-8.

[121] P. Patsalas, S. Kaziannis, C. Kosmidis, D. Papadimitriou, G. Abadias, G.A. Evangelakis, Optimized pulsed laser deposition by wavelength and static electric field control: The case of tetrahedral amorphous carbon films, J. Appl. Phys. 101 (2007) 15–18. doi:10.1063/1.2745445.

[122] G.M. Matenoglou, H. Zoubos, A. Lotsari, C.E. Lekka, P. Komninou, G.P. Dimitrakopulos, C. Kosmidis, G.A. Evangelakis, P. Patsalas, Metal-containing amorphous carbon (a-C:Ag) and AlN (AlN:Ag) metallo-dielectric nanocomposites, Thin Solid Films. 518 (2009) 1508–1511. doi:10.1016/j.tsf.2009.09.098.

[123] C.A. Tweedie, G. Constantinides, K.E. Lehman, D.J. Brill, G.S. Blackman, K.J. Van Vliet, Enhanced stiffness of amorphous polymer surfaces under confinement of localized contact loads, Adv. Mater. 19 (2007) 2540–2546.

[124] S. Logothetidis, S. Kassavetis, C. Charitidis, Y. Panayiotatos, A. Laskarakis,

Nanoindentation studies of multilayer amorphous carbon films, Carbon N. Y. 42 (2004) 1133–1136. doi:10.1016/j.carbon.2003.12.054.

[125] E. Martínez, Study of the mechanical properties of tetrahedral amorphous carbon films by nanoindentation and nanowear measurements, Diam. Relat. Mater. 10 (2001) 145–152. doi:10.1016/S0925-9635(00)00461-1.

[126] ISO 14577-4, Metallic materials -- Instrumented indentation test for hardness and materials parameters -- Part 4: Test method for metallic and non-metallic coatings, (2007).

[127] M. Zhao, W.S. Slaughter, M. Li, S.X. Mao, Material-length-scale-controlled nanoindentation size effects due to strain-gradient plasticity, Acta Mater. 51 (2003) 4461–4469. doi:10.1016/S1359-6454(03)00281-7.

[128] D. Christopher, R. Smith, A. Richter, Atomistic modelling of nanoindentation in iron and silver, Nanotechnology. 12 (2001) 372–383. doi:10.1088/0957-4484/12/3/328.

[129] X. Li, H. Gao, C.J. Murphy, K.K. Caswell, Nanoindentation of Silver Nanowires, Nano Lett. 3 (2003) 1495–1498. doi:10.1021/nl034525b.

[130] B.D. Beake, A.A. Ogwu, T. Wagner, Influence of experimental factors and film thickness on the measured critical load in the nanoscratch test, Mater. Sci. Eng. A. 423 (2006) 70–73. doi:10.1016/j.msea.2005.09.121.

[131] J. Sekler, P.A. Steinmann, H.E. Hintermann, The scratch test: Different critical load determination techniques, Surf. Coatings Technol. 36 (1988) 519–529. doi:10.1016/0257-8972(88)90179-X.

[132] P.A. Steinmann, Y. Tardy, H.E. Hintermann, Adhesion testing by the scratch test method: The influence of intrinsic and extrinsic parameters on the critical load, Thin Solid Films. 154 (1987) 333–349. doi:10.1016/0040-6090(87)90377-4.

[133] G.S. Fox-Rabinovich, B.D. Beake, J.L. Endrino, S.C. Veldhuis, R. Parkinson, L.S. Shuster, M.S. Migranov, Effect of mechanical properties measured at room and elevated temperatures on the wear resistance of cutting tools with TiAlN and AlCrN coatings, Surf. Coatings Technol. 200 (2006) 5738–5742. doi:10.1016/j.surfcoat.2005.08.132.

[134] T.O. Kääriäinen, P.J. Kelly, D.C. Cameron, B. Beake, H. Li, P.M. Barker, C.F. Struller, Nanoscratch testing of atomic layer deposition and magnetron sputtered TiO2 and Al2O3 coatings on polymeric substrates, J. Vac. Sci. Technol. A Vacuum, Surfaces, Film. 30 (2012) 01A132. doi:10.1116/1.3665418.

[135] B.D. Beake, T.W. Liskiewicz, Comparison of nano-fretting and nano-scratch tests on biomedical materials, Tribol. Int. 63 (2013) 123–131. doi:10.1016/j.triboint.2012.08.007.

[136] S. Neuville, A. Matthews, A perspective on the optimisation of hard carbon and related coatings for engineering applications, Thin Solid Films. 515 (2007) 6619–6653. doi:10.1016/j.tsf.2007.02.011.

[137] S. Zhang, D. Sun, Y. Fu, H. Du, Toughness measurement of thin films: a critical review, Surf. Coatings Technol. 198 (2005) 74–84. doi:10.1016/j.surfcoat.2004.10.021.

[138] S. Kataria, S. Dhara, H.C. Barshilia, S. Dash, A.K. Tyagi, Evolution of coefficient of friction with deposition temperature in diamond like carbon thin films, J. Appl. Phys. 112 (2012) 1–9. doi:10.1063/1.4740082.

[139] M. Constantinou, M. Pervolaraki, P. Nikolaou, C. Prouskas, P. Patsalas, P. Kelires, J. Giapintzakis, G. Constantinides, Microstructure and nanomechanical properties of pulsed excimer laser deposited DLC:Ag films: Enhanced nanotribological response, Surf. Coatings Technol. 309 (2017) 320–330. doi:10.1016/j.surfcoat.2016.11.084.

[140] A.M. Ribeiro, T.H.S. Flores-Sahagun, R.C. Paredes, A perspective on molybdenum biocompatibility and antimicrobial activity for applications in implants, J. Mater. Sci. 51 (2016) 2806–2816. doi:10.1007/s10853-015-9664-y.

[141] M. Khrushchov, I. Levin, E. Marchenko, V. Avdyukhina, M. Petrzhik, Effect of structure and deposition technology on tribological properties of DLC coatings alloyed with VIA group metals, J. Phys. Conf. Ser. 729 (2016) 12016. doi:10.1088/1742-6596/729/1/012016.

[142] R.K.. Fu, Y.. Mei, L.. Shen, G.. Siu, P.K. Chu, W.. Cheung, S.. Wong, Molybdenum–carbon film fabricated using metal cathodic arc and acetylene dual

plasma deposition, Surf. Coatings Technol. 186 (2004) 112–117. doi:10.1016/j.surfcoat.2004.04.024.

[143] Rusli, S.F. Yoon, Q.F. Huang, H. Yang, M.B. Yu, J. Ahn, Q. Zhang, E.J. Teo, T. Osipowicz, F. Watt, Investigation of molybdenum-carbon films (Mo-C : H) deposited using an electron cyclotron resonance chemical vapor deposition system, J. Appl. Phys. 88 (2000) 3699–3704. doi:10.1063/1.1288224.

[144] H. Rusli, S.F. Yoon, Q.F. Huang, J. Ahn, Q. Zhang, H. Yang, Y.S. Wu, E.J. Teo, T. Osipowicz, F. Watt, Metal-containing amorphous carbon film development using electron cyclotron resonance CVD, Diam. Relat. Mater. 10 (2001) 132–138. doi:10.1016/S0925-9635(00)00459-3.

[145] Q.F. Huang, S.F. Yoon, Rusli, Q. Zhang, J. Ahn, Dielectric properties of molybdenum-containing diamond-like carbon films deposited using electron cyclotron resonance chemical vapor deposition, Thin Solid Films. 409 (2002) 211–219. doi:10.1016/S0040-6090(02)00049-4.

[146] L.L. Wang, R.Y. Wang, S.J. Yan, R. Zhang, B. Yang, Z.D. Zhang, Z.H. Huang, D.J. Fu, Structure and properties of Mo-containing diamond-like carbon films produced by ion source assisted cathodic arc ion-plating, Appl. Surf. Sci. 286 (2013) 109–114. doi:10.1016/j.apsusc.2013.09.029.

[147] L. Ji, H. Li, F. Zhao, J. Chen, H. Zhou, Microstructure and mechanical properties of Mo/DLC nanocomposite films, Diam. Relat. Mater. 17 (2008) 1949–1954. doi:10.1016/j.diamond.2008.04.018.

[148] C. Anandan, L. Mohan, P.D. Babu, Electrochemical studies and growth of apatite on molybdenum doped DLC coatings on titanium alloy β-21S, Appl. Surf. Sci. 296 (2014) 86–94. doi:10.1016/j.apsusc.2014.01.049.

[149] A.A. Voevodin, M.S. Donley, Preparation of amorphous diamond-like carbon by pulsed laser deposition: a critical review, Surf. Coatings Technol. 82 (1996) 199–213. doi:10.1016/0257-8972(95)02734-3.

[150] A.A. Voevodin, A.W. Phelps, J.S. Zabinski, M.S. Donley, Friction induced phase transformation of pulsed laser deposited diamond-like carbon, Diam. Relat. Mater. 5 (1996) 1264–1269. doi:10.1016/0925-9635(96)00538-9.

[151] G.A. Tritsaris, C. Mathioudakis, P.C. Kelires, E. Kaxiras, Optical and elastic properties of diamond-like carbon with metallic inclusions: A theoretical study, J. Appl. Phys. 112 (2012). doi:10.1063/1.4765721.

[152] J.H. Choi, S.C. Lee, K.R. Lee, A first-principles study on the bond characteristics in carbon containing Mo, Ag, or Al impurity atoms, Carbon N. Y. 46 (2008) 185–188. doi:10.1016/j.carbon.2007.11.005.

[153] X. Li, K.R. Lee, A. Wang, Chemical bond structure of metal-incorporated carbon system, J. Comput. Theor. Nanosci. 10 (2013) 1688–1692. doi:10.1166/jctn.2013.3110.

[154] X. Li, P. Ke, A. Wang, Probing the Stress Reduction Mechanism of Diamond-Like Carbon Films by Incorporating Ti , Cr , or W Carbide-Forming Metals : Ab Initio Molecular Dynamics Simulation, (2015). doi:10.1021/acs.jpcc.5b00058.

[155] T.S. Srivatsan, B.G. Ravi, A.S. Naruka, L. Riester, S. Yoo, T.S. Sudarshan, Microstructure and hardness of copper powder consolidated by plasma pressure compaction, J. Mater. Eng. Perform. 10 (2001) 449–455. doi:10.1361/105994901770344872.

[156] Z.Q. Fu, C. biao Wang, W. Zhang, W. Wang, W. Yue, X. Yu, Z. jian Peng, S. sheng Lin, M. jiang Dai, Influence of W content on tribological performance of W-doped diamond-like carbon coatings under dry friction and polyalpha olefin lubrication conditions, Mater. Des. 51 (2013) 775–779. doi:10.1016/j.matdes.2013.04.098.

[157] Z. Wen, G. Xuanqiao, Z. Pingxiang, H. Zhongwu, L. Laiping, C. Jun, Nanoindentation Size Effect of Tungsten Single Crystal, Rare Met. Mater. Eng. 46 (2017) 3626–3632. doi:10.1016/S1875-5372(18)30048-1.

[158] Pulsed laser deposition of diamond-like carbon wear protective coatings: a review, Surf. Coatings Technol. 92 (1997) 42–49. doi:10.1016/S0257-8972(97)00007-8.

[159] G. Dearnaley, J.H. Arps, Biomedical applications of diamond-like carbon (DLC) coatings: A review, Surf. Coatings Technol. 200 (2005) 2518–2524. doi:10.1016/j.surfcoat.2005.07.077.

[160] Q. Yang, D.E. Joyce, S. Saranu, G.M. Hughes, a. Varambhia, M.P. Moody, P. a. J. Bagot, A combined approach for deposition and characterization of atomically engineered catalyst nanoparticles, Catal. Struct. React. 758 (2015) 2055075815Y.000. doi:10.1179/2055075815Y.0000000006.

[161] L.G. Parratt, Surface studies of solids by total reflection of x-rays, Phys. Rev. 95 (1954) 359–369. doi:10.1103/PhysRev.95.359.

[162] D. Photiou, N.T. Panagiotopoulos, L. Koutsokeras, G.A. Evangelakis, G. Constantinides, Microstructure and nanomechanical properties of magnetron sputtered Ti−Nb films, Surf. Coatings Technol. 302 (2016) 310–319. doi:10.1016/j.surfcoat.2016.06.014.

[163] M. Constantinou, M. Pervolaraki, L. Koutsokeras, C. Prouskas, P. Patsalas, P. Kelires, Enhancing the nanoscratch resistance of pulsed laser deposited DLC fi lms through molybdenum-doping, Surf. Coat. Technol. 330 (2017) 185–195. doi:10.1016/j.surfcoat.2017.09.048.

[164] T.R. Society, R. Society, C. Papers, P. Character, Downloaded from http://rspa.royalsocietypublishing.org/ on February 24 , 2017, (n.d.).

[165] N. Guyot, Y. Harmand, The role of the sample shape and size on the internal stress induced curvature of thin-film substrate systems, 41 (2004) 5143–5154. doi:10.1016/j.ijsolstr.2004.03.015.

[166] P. De Saurupt, Coating internal stress measurement through the curvature method : A geometry-based criterion delimiting the relevance of Stoney ' s formula, 200 (2006) 5259–5267. doi:10.1016/j.surfcoat.2005.06.018.

[167] V. Gelinas, D. Vidal, Determination of particle shape distribution of clay using an automated AFM image analysis method, Powder Technol. 203 (2010) 254–264. doi:10.1016/j.powtec.2010.05.016.

[168] Y. Gu, H. Xie, J. Gao, D. Liu, C.T. Williams, C.J. Murphy, H.J. Ploehn, AFM characterization of dendrimer-stabilized platinum nanoparticles, Langmuir. 21 (2005) 3122–3131. doi:10.1021/la047843e.

[169] A.C. Ferrari, J. Robertson, Raman spectroscopy of amorphous, nanostructured, diamond-like carbon, and nanodiamond., Philos. Trans. A. Math. Phys. Eng. Sci.

362 (2004) 2477–2512. doi:10.1098/rsta.2004.1452.

[170] Š. Meškinis, A. Vasiliauskas, K. Šlapikas, G. Niaura, R. Juškenas, M. Andrulevičius, S. Tamulevičius, Structure of the silver containing diamond like carbon films: Study by multiwavelength Raman spectroscopy and XRD, Diam. Relat. Mater. 40 (2013) 32–37. doi:10.1016/j.diamond.2013.09.004.

[171] A.C. Ferrari, J. Robertson, Interpretation of Raman spectra of disordered and amorphous carbon, Phys. Rev. B. 61 (1999) 14095–14107. doi:org/10.1103/PhysRevB.61.14095.

[172] K. Baba, R. Hatada, S. Flege, W. Ensinger, Preparation and properties of Ag-containing diamond-like carbon films by magnetron plasma source ion implantation, Adv. Mater. Sci. Eng. 2012 (2012). doi:10.1155/2012/536853.

[173] B.D. Beake, M.I. Davies, T.W. Liskiewicz, V.M. Vishnyakov, S.R. Goodes, Nano-scratch, nanoindentation and fretting tests of 5-80nm ta-C films on Si(100), Wear. 301 (2013) 575–582. doi:10.1016/j.wear.2013.01.073.

[174] B.D. Beake, V.M. Vishnyakov, R. Valizadeh, J.S. Colligon, Influence of mechanical properties on the nanoscratch behaviour of hard nanocomposite TiN/Si 3 N 4 coatings on Si, J. Phys. D. Appl. Phys. 39 (2006) 1392–1397. doi:10.1088/0022-3727/39/7/009.

[175] B. Shi, J.L. Sullivan, B.D. Beake, An investigation into which factors control the nanotribological behaviour of thin sputtered carbon films, J. Phys. D. Appl. Phys. 41 (2008) 45303. doi:10.1088/0022-3727/41/4/045303.

[176] K. Miyoshi, Adhesion, friction and micromechanical properties of ceramics, Surf. Coatings Technol. 36 (1988) 487–501. doi:10.1016/0257-8972(88)90177-6.

[177] G.M. Hamilton, Explicit equations for the stresses beneath a sliding spherical contact, Proc. Inst. Mech. Eng. 197C (1983) 53–59. doi:10.1243/PIME_PROC_1983_197_076_02.

[178] C.A. Charitidis, Int . Journal of Refractory Metals & Hard Materials Nanomechanical and nanotribological properties of carbon-based thin films : A review, Int. J. Refract. Met. Hard Mater. 28 (2010) 51–70. doi:10.1016/j.ijrmhm.2009.08.003.

[179] A. Pardo, C. Gómez-Aleixandre, Friction and Wear Behavior of Plasma Assisted Chemical Vapor Deposited Nanocomposites Made of Metal Nanoparticles Embedded in a Hydrogenated Amorphous Carbon Matrix, Surf. Coatings Technol. 206 (2012) 3116–3124. doi:10.1016/j.surfcoat.2011.12.041.

[180] X. Yu, Y. Qin, C.B. Wang, Y.Q. Yang, X.C. Ma, Effects of nanocrystalline silver incorporation on sliding tribological properties of Ag-containing diamond-like carbon films in multi-ion beam assisted deposition, Vacuum. 89 (2013) 82–85. doi:10.1016/j.vacuum.2011.11.007.

[181] R. Hatada, S. Flege, A. Bobrich, W. Ensinger, C. Dietz, K. Baba, T. Sawase, T. Watamoto, T. Matsutani, Preparation of Ag-containing diamond-like carbon films on the interior surface of tubes by a combined method of plasma source ion implantation and DC sputtering, Appl. Surf. Sci. 310 (2014) 257–261. doi:10.1016/j.apsusc.2014.03.071.

[182] A. Erdemir, C. Bindal, G.R. Fenske, C. Zuiker, P. Wilbur, Characterization of transfer layers forming on surfaces sliding against diamond-like carbon, Surf. Coatings Technol. 86–87 (1996) 692–697. doi:10.1016/S0257-8972(96)03073-3.

[183] J.H. Kim, J.H. Shin, D.H. Shin, M.-W. Moon, K. Park, T.-H. Kim, K.M. Shin, Y.H. Won, D.K. Han, K.-R. Lee, Comparison of diamond-like carbon-coated nitinol stents with or without polyethylene glycol grafting and uncoated nitinol stents in a canine iliac artery model., Br. J. Radiol. 84 (2011) 210–5. doi:10.1259/bjr/21667521.

[184] A. Salahas, A. Vrahatis, I. Karabinos, I. Antonellis, G. Ifantis, I. Gavaliatsis, P. Anthopoulos, A. Tavernarakis, Success, Safety, and Efficacy of Implantation of Diamond-Like Carbon-Coated Stents, Angiology. 58 (2007) 203–210. doi:10.1177/0003319707300360.

[185] L. Joska, J. Fojt, O. Mestek, L. Cvrcek, V. Brezina, The effect of a DLC coating adhesion layer on the corrosion behavior of titanium and the Ti6Al4V alloy for dental implants, Surf. Coatings Technol. 206 (2012) 4899–4906. doi:10.1016/j.surfcoat.2012.05.089.

[186] A. Ozkomur, M. Erbil, T. Akova, Diamondlike carbon coating as a galvanic corrosion barrier between dental implant abutments and nickel-chromium

superstructures., Int. J. Oral Maxillofac. Implants. 28 (2013) 1037–47.

[187] D. Photiou, N.T. Panagiotopoulos, L. Koutsokeras, G.A. Evangelakis, G. Constantinides, Microstructure and nanomechanical properties of magnetron sputtered Ti − Nb films, Surf. Coatings Technol. 302 (2016) 310–319. doi:10.1016/j.surfcoat.2016.06.014.

[188] W. Elmay, E. Patoor, T. Gloriant, F. Prima, P. Laheurte, Improvement of Superelastic Performance of Ti-Nb Binary Alloys for Biomedical Applications, J. Mater. Eng. Perform. 23 (2014) 2471–2476. doi:10.1007/s11665-014-0876-0.

[189] H. Tobe, H.Y. Kim, T. Inamura, H. Hosoda, T.H. Nam, S. Miyazaki, Effect of Nb content on deformation behavior and shape memory properties of Ti–Nb alloys, J. Alloys Compd. 577 (2013) S435–S438. doi:10.1016/j.jallcom.2012.02.023.

[190] Q. Chen, G.A. Thouas, Metallic implant biomaterials, Mater. Sci. Eng. R Reports. 87 (2015) 1–57. doi:10.1016/j.mser.2014.10.001.

[191] P.B. Sick, G. Gelbrich, U. Kalnins, A. Erglis, R. Bonan, W. Aengevaeren, D. Elsner, B. Lauer, M. Woinke, O. Brosteanu, G. Schuler, Comparison of early and late results of a Carbofilm-coated stent versus a pure high-grade stainless steel stent (the Carbostent-Trial), Am. J. Cardiol. 93 (2004) 1351–1356. doi:10.1016/j.amjcard.2004.02.029.

[192] M. Della Barbera, F. Laborde, G. Thiene, V. Arata, E. Pettenazzo, E. Pasquino, L. Behr, M. Valente, Sovering annuloplasty rings: experimental pathology in the sheep model., Cardiovasc. Pathol. 14 (2005) 96–103. doi:10.1016/j.carpath.2004.12.005.

[193] D. Antoniucci, A. Bartorelli, R. Valenti, P. Montorsi, G.M. Santoro, F. Fabbiocchi, L. Bolognese, A. Loaldi, M. Trapani, D. Trabattoni, G. Moschi, S. Galli, Clinical and angiographic outcome after coronary arterial stenting with the carbostent., Am. J. Cardiol. 85 (2000) 821–5.

[194] E. Meyer, Atomic force microscopy, Prog. Surf. Sci. 41 (1992) 3–49. doi:10.1016/0079-6816(92)90009-7.

[195] N. Jalili, K. Laxminarayana, A review of atomic force microscopy imaging

systems: application to molecular metrology and biological sciences, Mechatronics. 14 (2004) 907–945. doi:10.1016/j.mechatronics.2004.04.005.

[196] G.M. McClelland, R. Erlandsson, S. Chiang, Atomic Force Microscopy: General Principles and a New Implementation, in: Rev. Prog. Quant. Nondestruct. Eval., Springer US, Boston, MA, 1987: pp. 1307–1314. doi:10.1007/978-1-4613-1893-4_148.

[197] P. Markiewicz, M.C. Goh, Atomic force microscopy probe tip visualization and improvement of images using a simple deconvolution procedure, Langmuir. 10 (1994) 5–7. doi:10.1021/la00013a002.

[198] H.J. Butt, B. Cappella, M. Kappl, Force measurements with the atomic force microscope: Technique, interpretation and applications, Surf. Sci. Rep. 59 (2005) 1–152. doi:10.1016/j.surfrep.2005.08.003.

[199] E. Gnecco, R. Bennewitz, T. Gyalog, E. Meyer, Friction experiments on the nanometre scale, J. Physics-Condensed Matter. 13 (2001) R619–R642. doi:10.1088/0953-8984/13/31/202.

[200] Y. Martin, H.K. Wickramasinghe, Magnetic imaging by “force microscopy” with 1000 Angstrom resolution, Appl. Phys. Lett. 50 (1987) 1455–1457. doi:10.1063/1.97800.

[201] A.M. Rawlett, T.J. Hopson, L.A. Nagahara, R.K. Tsui, G.K. Ramachandran, S.M. Lindsay, Electrical measurements of a dithiolated electronic molecule via conducting atomic force microscopy, Appl. Phys. Lett. 81 (2002) 3043–3045. doi:10.1063/1.1512815.

[202] A. San Paulo, R. García, High-Resolution Imaging of Antibodies by Tapping-Mode Atomic Force Microscopy: Attractive and Repulsive Tip-Sample Interaction Regimes, Biophys. J. 78 (2000) 1599–1605. doi:10.1016/S0006-3495(00)76712-9.

[203] I. Schmitz, M. Schreiner, G. Friedbacher, M. Grasserbauer, Tapping-Mode AFM in Comparison to Contact-Mode AFM as a Tool for in Situ Investigations of Surface Reactions with Reference to Glass Corrosion, Anal. Chem. 69 (1997) 1012–1018. doi:10.1021/ac9607020.

[204] R. García, R. Pérez, Dynamic atomic force microscopy methods, Surf. Sci. Rep. 47 (2002) 197–301. doi:10.1016/S0167-5729(02)00077-8.

[205] R. Garcia, C.J. Gómez, N.F. Martinez, S. Patil, C. Dietz, R. Magerle, Identification of nanoscale dissipation processes by dynamic atomic force microscopy, Phys. Rev. Lett. 97 (2006) 1–4. doi:10.1103/PhysRevLett.97.016103.

[206] B. Jähne, Practical handbook on image processing for scientific and technical applications, CRC Press, 2004.

[207] L. Fekete, K. Kůsová, V. Petrák, I. Kratochvílová, AFM topographies of densely packed nanoparticles: a quick way to determine the lateral size distribution by autocorrelation function analysis, J. Nanoparticle Res. 14 (2012) 1062. doi:10.1007/s11051-012-1062-7.

[208] P. Klapetek, I. Ohlidal, D. Franta, A. Montaigne-Ramil, A. Bonanni, D. Stifter, H. Sitter, Atomic force microscopy characterization of ZnTe epitaxial films, Acta Phys. Slovaca. 53 (2003) 223–230. doi:10.1143/JJAP.42.4706.

[209] R.R.L. De Oliveira, D. a. C. Albuquerque, T.G.S. Cruz, F.M.Y. and F.L. Leite, Measurement of the Nanoscale Roughness by Atomic Force Microscopy: Basic Principles and Applications, At. Force Microsc. - Imaging, Meas. Manip. Surfaces At. Scale. (2012) 256. doi:10.5772/37583.

APPENDIX A: Atomic force microscopy

Atomic force microscopy (AFM) is a technique that allows the observation and measurement of surface properties of materials in atomic scale [194]. During an AFM measurement a very flexible cantilever with a sharp probe mechanically scans the material surface. The force being developed between the probe and the sample causes deflection to the cantilever which for each sample-tip position can be detected through the motion of an initially fixed laser spot on a photodiode (that translates the motion of the laser spot to voltage/amperes signal), and then returns to its original deflection through a feedback circuit that mechanically moves the piezoelectric transducer up and down in the z direction. The recording of the precise motion (up and down) of the piezoelectric transducer for each sample-tip position is what gives the material topography [195].

A 1 AFM instrument

A photograph of our research unit's AFM system is shown in Figure A.1. The main parts of the AFM instrument are the AFM microscope, the electronic box and the computer with the two supporting screens. By itself, the AFM microscope comprises of the manually moving XY stepper motors, the automatic moving Z motors, the piezoelectric scanner, the sample holder, the force sensor, the feedback mechanism and the optical microscope. The significance of the existence as well as the working operation of these components is explained below. The AFM microscope is placed on a vibration isolation base to minimize any noise coming from the surrounding environment on the measurements. A protective enclosure is also available to be placed upon the AFM microscope to reduce acoustic noise.

The electronic box is placed between the AFM microscope and the computer (see Figure A.1). Their functions include the direct communication of AFM microscope with the computer thought signals that are generated and accepted from the electronic box. The AFM user control the AFM signals by setting parameters on scanning software installed on the computer. The later allows to a user to control AFM imaging process. Also, the software provides the opportunity to a user to analyze obtainable AFM images.

Figure A.1 Photograph of the AFM instrument installed at RUNMS.

Figure A.2 shows some of the visible parts of the AFM microscope. The XY sample motors are used to perform manually coarse movement of the sample under the AFM tip, while the specific placement of the sample under the AFM tip is usually performed with the help of an optical microscope. The tip-sample approach is performed by the Z motor that initially moves the tip onto the surface (or inversely when is applicable) with high velocity and slows down when the tip is very near to the surface, to avoid any crashing of the tip. Piezoelectric transducer, force sensor and feedback mechanism are the three basic equipment of the AFM and deserve further description. Their synergistic operation is as follows: the force sensor senses the forces that act between the tip and the sample, while the feedback mechanism drives the signals from the force sensor back to the piezoelectric scanner to maintain a fixed force between the tip and the sample during scanning procedure. The ability of AFM to control small bends of the cantilever through a feedback loop is what gives high resolution to the AFM images [196].

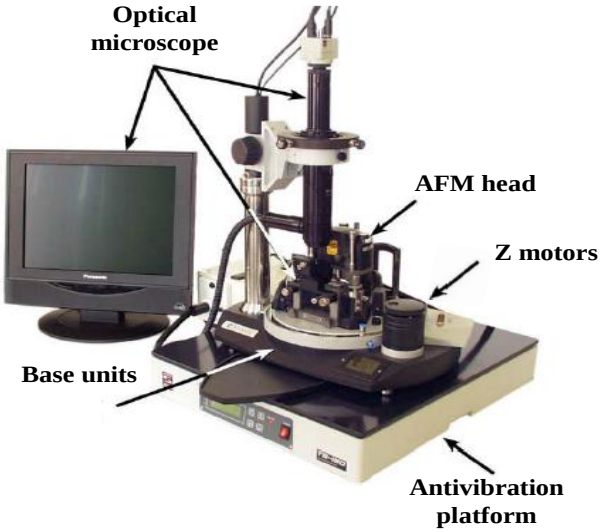

Figure A.2 Photograph of some of the main parts of the AFM microscope.

Piezoelectric scanners are electromechanical components that convert electrical potential to mechanical motion. This means that any change to the accepted signal voltage produces mechanical expansion/contraction to piezo material in a way such its geometry is changed. For AFM, piezoelectric scanners are usually made from ceramic material having tube geometry to allow precise sample movement at x-y-z directions. The characteristic of the tube scanners is their low and precise expansion coefficient of 0.1 nm/V. This means that an application of a value of 3 V to the piezoelectric scanner can expand or shrink them 0.3 nm depending of the cantilever bending that can be up or down. Subsequently, this nanometer resolution is what makes these materials important for AFM instruments.

The forces acting between the tip and the sample are measured using the force sensor component. A common force sensor in AFM consists of a cantilever with an integrated tip and a photodiode. A laser is directed onto the back side of the cantilever, and the reflected laser beam is detected from a four quadrant photodiode as is shown in Figure A.3. The distance between the cantilever and the photodiode is large so very small flexions of the cantilever during scanning can be measured through the change of the position of the laser spot. Then, the photodiode converts the laser intensity to current/voltage, and the output voltage is translated to mechanical motion with piezo material through the feedback loop mechanism. In AFM, the optical lever force sensor needs alignment. The alignment process consists of directing the laser beam to be reflected with the highest intensity from the back side of the cantilever and then to place

the laser beam in the center of the four quadrant photodiode by manually moving only the photodiode component.

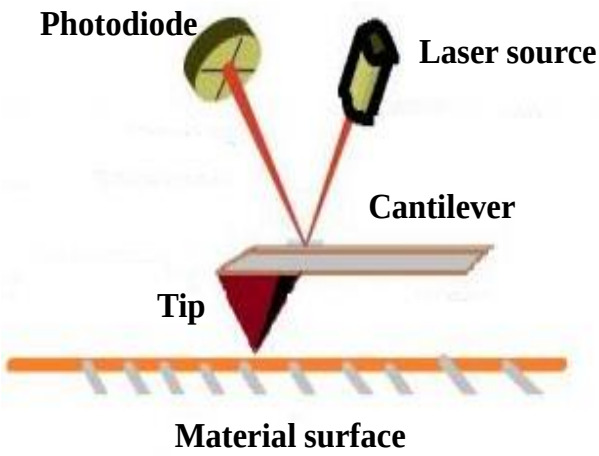

Figure A.3 Optical lever force sensor setup.

A feedback mechanism controls the signal between the force sensor and the piezoelectric scanner and forwards the signal from the force sensor to the piezoelectric scanner to maintain a fixed distance between the tip and the sample and consequently constant force between each other. For example if the tip meets a hollow on the surface topography, the feedback mechanism acts as to move the piezoelectric scanner up so to maintain an initial force between the tip and the sample constant. Conversely, if the tip meets a particle on the surface, the piezoelectric scanner is routed as to move down to maintain a set force.

AFM tips are usually constructed using micromechanical processes and are made from silicon. The process includes the integration of the probe on a cantilever beam and then on a chip. The probe curvature plays an important role to the quality of the AFM image as an AFM image is a convolution of the AFM probe shape and the sample topography [197]. Although AFM probes are considered to be sharp their shape usually changes during scanning process something that introduces image artefacts. Such examples are illustrated in Figure A.4. Scanning a step feature with a blunt probe the details from its side are missing and at the same time makes the feature looks bigger in the x-y dimensions. Scanning a pit feature with blunt probe information for its depth cannot be reachable. The results of using a sharp probe are also illustrated in Figure A.4 where one can conclude that better features can be imaging the sharper is the probe.

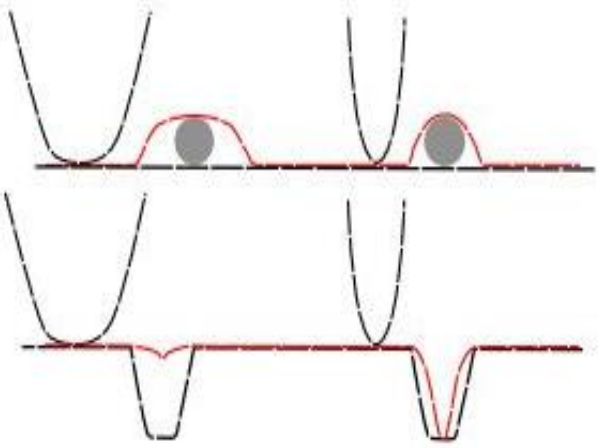

Figure A.4 Results on AFM image by scanning a blunt/sharp probe above a step feature (top) and on a pit feature (down). Image adopted from http://www.pra-ma.com/images/artifacs/conv_small.jpg.

A 2 AFM modes of experiments

A large number of experiments can be performed using an AFM. Beyond the measurement of the topography of a material, an AFM can be used to measure other physical properties of materials for example their electrical, magnetic and mechanical proprties. Some representative puplications are given [198–201].

The idea behind these experimental modes is to use a tip that is always in contact with the probed surface (contact mode AFM) , or is oscillated upon the surface in a way that is non in contact with the surface (noncontact mode AFM) or partially in contact with the surface during oscillations (semicontact mode AFM) [194].

For contact mode and oscillation mode both topographical and nontopographical information can be measured. Starting with contact mode, the first information that can be measured is the topography of a material. The working principle behind such measurement is that the force acting between the probe and the surface remains always constant by keeping the cantillever deflection (DFL signal) at a constant value trhought the feedback loop and the controlled motion of the piezolectric material. The collection of the motions (up and down) of the piezoelectric material for every step of the probe during scanning gives us a map of height measurements (topography) that is later translated using light coloring to a more easy visually image. An example of AFM height measuremt on a standard material with step feautes is shown in Figure A.5.

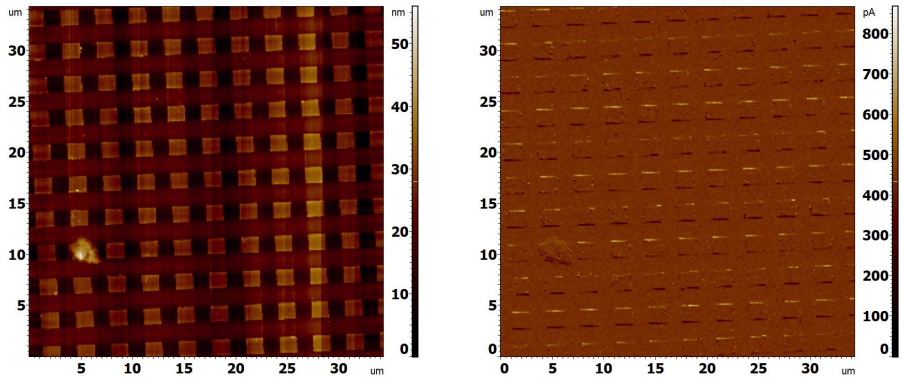

Figure A.5 (a) AFM height image on a standard material. (b) Deflection image for the same material. The height and DFL signals were acquired at the same time.

During contact mode the veritcal bending of the cantilever (i.e., the deflection signal) can also be recorded as an image. In an ideal situtation this signal must not show any light contrasts as the deflection in contact mode is always coped to be kept constant throught feedback loop. Nevertheless, as the response of the feedback loop electronic system cannot cope instantaneous usually the DFL signal is observed to have light contracts. An example of imaging the DFL signal during measuring the topography of a standard material is shown in the righ side of Figure A.5. For a system with optimum feedback loop these ligh contrasts correspond well with the high slope regions in topography image. In other case this signal (also called as an error signal) could be used to show errors in the topography image.

In contact mode also the lateral force can be measured. This kind of measurement is a result of the recording of the lateral deflection of the cantilever during scanning. Normally someone would expect that the lateral deflection of the cantilever is coming from the frictional differences of the different phases on a surface. Nevertheless this is not the case as the lateral deflection of the cantilever may also be a result of the topographic/height variations of the surface. Usually this kind of signal is better to be measured from flat surfaces in order avoid contributions from topography and get only the frictional differences of materials on recording AFM image [199].

In oscillating mode the cantilever either is oscillated very close to the surface (noncontact mode) or is touching the surface periodically by oscillating upon the surface with a higher amplitude (semicontact mode). In both cases the oscillation of the cantilever is driven by an additional oscilation signal (usually applied from the oscillation of a piezoelectric material placed behind the cantilever). The working

operation of the semicontact mode is somewhat different from the contact mode. The scanning procedure starts by oscillating the cantilever far from the surface at its resonant frequency (i.e., the frequency where the amplitude of oscillation is maximum and the oscillation signal follows the applied signal so to have a zero phase degree). The procedure continues by landing the cantilever on the surface till oscillation is dampting due to probe-sample interactions. The damping of oscillation that leads to a change in amplitude and phase signals is set as the set point for semicontact mode. Next, as in contact mode, the set point (usually measured in volts) is send thru the feedback loop to the piezoelectric material to keep any oscillation deflection of the cantilever at a constant set value. For our AFM system only the semicontact mode is available, thus next partagrtaphs explain some functions of semicontact mode.

The primary operation of the semicontact mode is to record the topography of a material. The advantages of using this technique is the lower forces and the nonlateral forces act on the surface during scanning. Its disadvantage compared with contact mode AFM is that the resulting height image has lower resolution. This is because the tip is not always in contact with the surface and the deflection signal that is used to build the topography is coming by summing oscillation signals [202,203].

The signal that is used to build the topograpy in semicontact mode is the amplitude modulation. During oscillation of the probe the phase shift and frequency modulation can be recoreded as well. A plot of the phase shift (phase imaging) is a good signal to see mechanical variations of the surface that may include adhesion, viscolelastic and compositional differences. Usually the preselected phase of the cantilever shifted when is scanned on a softer/harder area compared to the initial. As phase signal is affected from the topography of the probed material is better to be acquired on a well flat surface [204,205]. Frequency modulation is also available for imaging and is a common signal acquisistion on noncontact mode under high vacuum conditions [204].

A 3 AFM imaging procedure

The AFM image acquisition can be performed using the AFM software. In this section we describe the general procedure to acquire AFM images. The basic steps for measuring AFM images are as follows:

a) Preparation of sample: Usually there is a no need for any sample preparation as the sample is not needed to be electrically conductive (to be coated with metallic coating) or to have any special size. Nevertheless, sample should be cleaned with dried air so any dust particle or other form of contamination that may affect imaging to be removed.

b) Placement of sample on AFM sample holder.

c) Placement of tip on AFM tip holder.

d) Optical alignment: The alignment process consists of directing the laser beam to be reflected from the back side of the cantilever (the operator looks for the highest refection intensity), and then to place the laser beam in the center of the four quadrant photodiode.

e) Resonant frequency: This step is necessary if the mode in use is the semicontact mode where the tip is oscillated upon the surface during scanning. During this step the cantilever is oscillated far from the surface looking the resonant frequency where the cantilever has the highest amplitude.

f) Sample - probe approach: The approach step is completed automatically by the controlled motion of the Z motors.

g) Setting feedback gain: Feedback gain controls the instantaneous response of the feedback mechanism and synchronize force sensor with the piezoelectric actuator; when feedback mechanism is off the cantilever bending are what build up the topography as the image signal is not coming from the height adjustment of the piezoelectric material but rather from the instantaneous deflection of the cantilever (by means of the DFL signal). For low feedback gain the cantilever does not follow the topography. For high feedback gain the cantilever is oscillated upon the surface. For an optimum feedback gain the cantilever follows the topography and the height image corresponds to the topography of the material. Feedback gain can be adjusted automatically by the software.

h) Start AFM image scan procedure.

i) Tip withdrawal when the imaging is finished.

The above imaging steps are a general procedure that any AFM user must follow to acquire images.

A 4 AFM image analysis

Beyond measuring, the AFM software can also be used for analysis of AFM images. Generally AFM analysis can be divided into three distinct steps that are processing, displaying and analysis of AFM image. The processing steps must be done with caution so the displayed AFM images be qualitative and show real surface characteristic, and, moreover, analysis steps to give quantitative results for materials.

Processing steps are performed on AFM image so to change it and make its surface characteristics easily measurable and observable. Examples of processing steps include flattening, filtering, and any other command that corrects artifacts/errors on AFM image. Displaying steps are performed so to make the surface features more visible and understandable. Examples of displaying steps include the two dimensional (2D) and three dimensional (3D) views. Analysis gives quantitative information from AFM images and some examples are the line profile analysis, particle analysis and roughness calculation. Next paragraphs will present some of the common processing, displaying and analysis functions.

A 1. 1 Processing steps

Flattening command is usually the first processing step applied on AFM image. The reason is because almost all AFM images have a tilted background (i.e., are usually observed to have bright and dark regions) that affects the observation of real height data. This background tilt is usually occurred from the sample itself (for example not being deposited on a well flat substrate) or from the tilted placement of the sample on the AFM stage. In addition tilting may be occurred from what is called scanner bow which comes from the instrument scanner type and produces a curvature to the AFM image. A good example to understand the effect of background tilting is to think for a 30 μm x 30 μm AFM scan with surface heights of about 10 nm. If the substrate is tilted at 1 degree during scanning, the height differences from one side to the other will be observed to be about 530 nm which is enough to mask the surface height features. Thus the subtraction of background tilting is necessary to be performed for any AFM image.

Flattening process can be performed using fitting lines (polynomial fitting equations). This routine is followed by, 1), fitting of a polynomial equation on each scan line, and,

2), subtraction of the polynomial shape from each scan line. The result is a well flatten scan line with the minimum height of all the scan lines - when are all presented together in an image - to zero value. An example of zero and second order polynomial on 10 μm x 10 μm AFM scan is shown in Figure A.6.

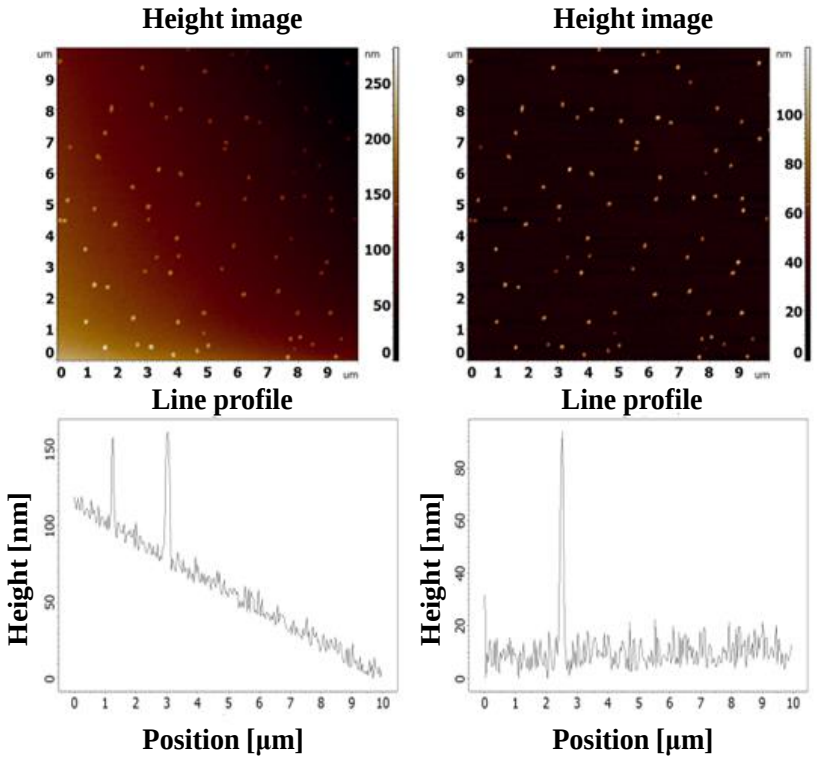

Figure A.6 Example of zero and second order polynomial fitting on 10 μm x 10 μm AFM scan on silver nanoparticles. Top: AFM height images. Bottom: Line profiles of AFM images. The zero polynomial fitting does not lead to levelling process while the second order polynomial subtracts both scanner bow and background tilt effects.

Moreover, flattering of AFM image can be performed using the two dimensional fitting procedure. During this procedure the best fitting surface is subtracted from the AFM image and moves the entire image so to be displayed in the same plane and the minimum point has a zero value. The latter gives the same result as the polynomial fitting equations but only requires that the scanner bow curvature does not existed in the image. Another useful processing command is the three points levelling. This function is more often used to flatten materials that contain step features. An example of a three points levelling on a film/substrate system is shown in Figure A.7. The three crosses that are used for subtracting only the tilting of the substrate give a well indication of the thickness of the film. From such measurement thickness of the material even being at

nanometer regime can be measured. In addition to this Figure A.8 shows an isolated crop image of the same step feature for better observation in the 3D view.

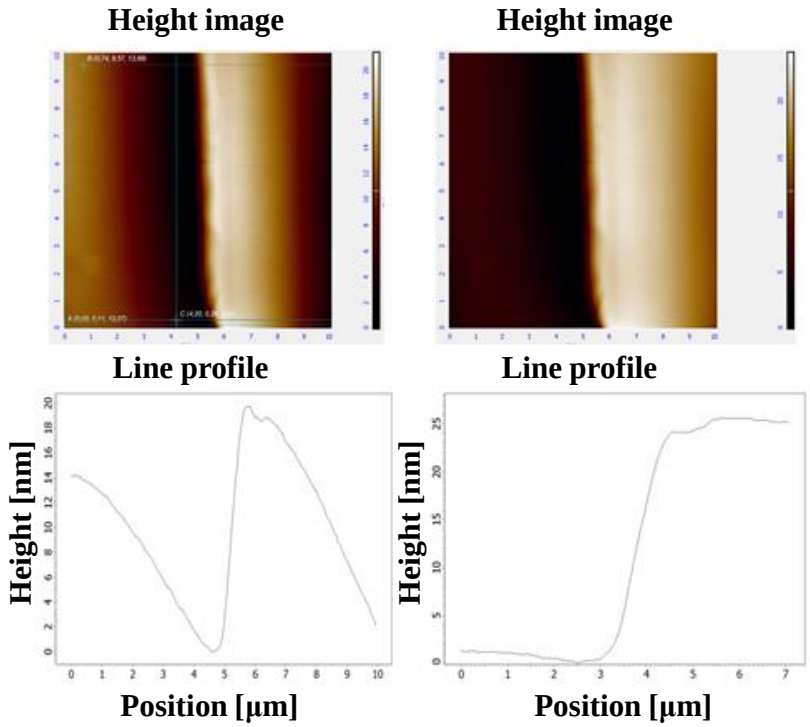

Figure A.7 Example of three points levelling procedure on an already well flatten AFM image.

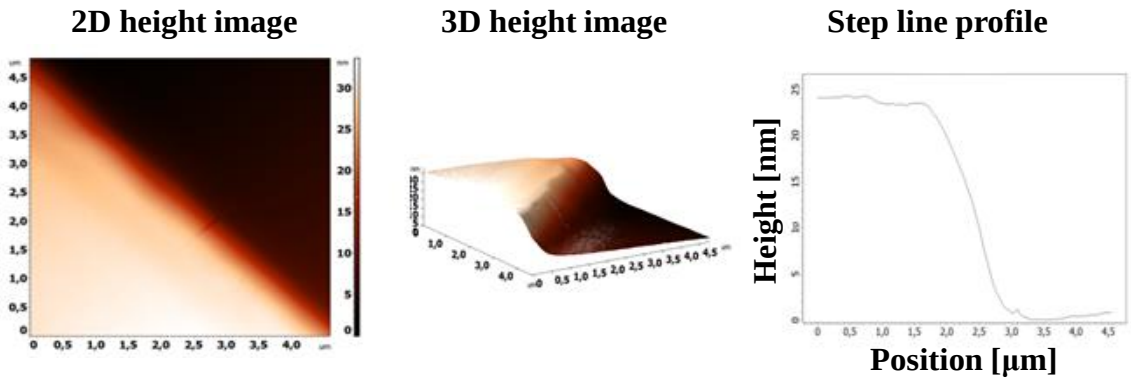

Figure A.8 From left to right, 2D view, 3D view and line profile of step feature.

Another significant processing tool is the exclusion of areas from fit. This function works well on AFM images presenting isolated height features on an already flat substrate the flattening of which can be performed by applying a 2nd order polynomial; such result on a sample containing Ag nanoparticles on silicon substrate is shown in Figure A.9. As can be seen, close to the areas where Ag nanoparticles exist the substrate observed artificially lower. This is because the polynomial fitting equation on the areas

that include nanoparticles fits nanoparticle height as well instead of only the substrate material. This leads to the subtraction of these height features and lowering the substrate. In this case the AFM image observed to have shadows close to the area with nanoparticles. This artefact can be easily encountered using exclusion of areas from fit function. This procedure allows to the user to draw squares at the areas where levelling is undesired to perform. A result of exclusion of areas from fit is shown in Figure 36 as well.

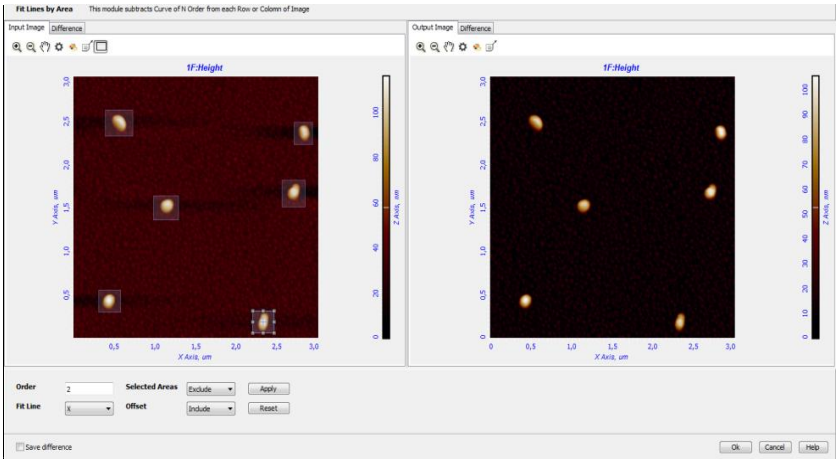

Figure A.9 Analysis window capture. Left: Example of polynomial levelling on AFM image with nanoparticles. Right: The same image with the levelling occurs only on areas where no squared draws.

A 1. 2 Displaying steps

Sometimes it is desirable to observe fine details on AFM height image that may be covered by very low or high features of the image. This can be easily done by adjusting the coloured bar scale of respective AFM image. The coloured bar scale represents all the heights that presented in the image. To reject the low or high features of AFM image the user must adjusts the coloured bar scale, so the image displaying only the height features that are desirable to observe. By doing this adjustment is like stretching the coloured bar scale and only the features that are desirable to observe are displaying coloured; the rejected features are observed with white bright colour. Such example can be seen in Figure A.10. Moreover, stretching of coloured bar scale can be also performed by stretching histogram plot accompanying with every AFM image. A histogram is a plot that shows height data - or any other data accumulated in the z scale - over frequency. Usually the majority of data are stretched in the center of the

histogram while minority of data are presented on the left and right part of the histogram. The software allows to the user to cut the minority of data and make the majority of data to be easily observed on the AFM image. This procedure results to the same effect as discussed above (i.e., coloured bar scale adjustment) and can be seen in Figure A.10 as well.

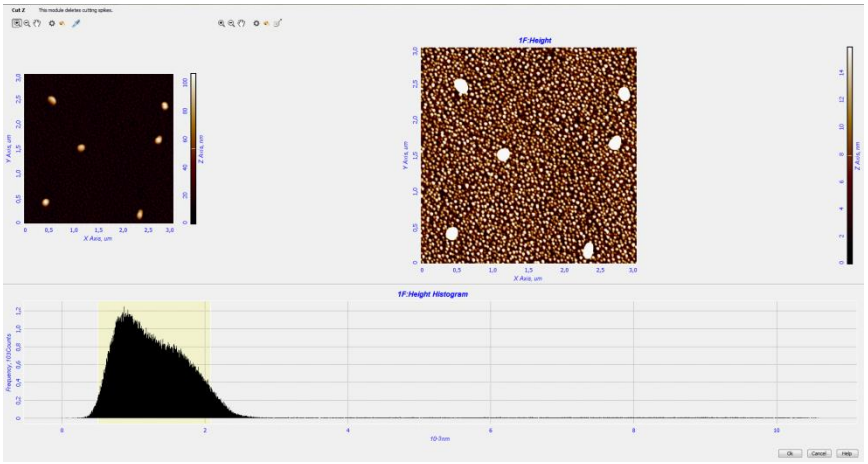

Figure A.10 Example of coloured bar scale and histogram adjustment on AFM height image. The image captured from analysis window.

Usually AFM images are presented in a 2 dimensional (2-D) view. Nevertheless, viewers that are not accustomed to see AFM data found it difficult to understand what they see. This can be easily solved by viewing AFM height data in a three dimensional (3-D) view. The 3-D rendering of AFM data is a simple way to show height differences so to be understandable by any viewer.

A 1. 3 Analysis steps

AFM features can be measured on a line profile. Length, width and height dimensions of surface features can be measured by applying horizontal, vertical and at any other angle line profiles. Example of a horizontal line profile measurement is seen in Figure A.11. Something that is important to be considered is that only the AFM height data are estimated with accuracy, as side edges of features suffer from convolution of the tip-sample shape and are usually observed larger than the real (see Figure A.4). Moreover, as the position of the line profile is dependent on the user eye may lead to significant error in the interpretation of the results. Also, the procedure can be characterized as time consuming for measuring the dimensions of large number of features on the surface. For

materials with large number of features (e.g., nanoparticles or granular materials), particle and/or grain analysis can be performed using statistical segmentation processes as will be discussed in following paragraphs.

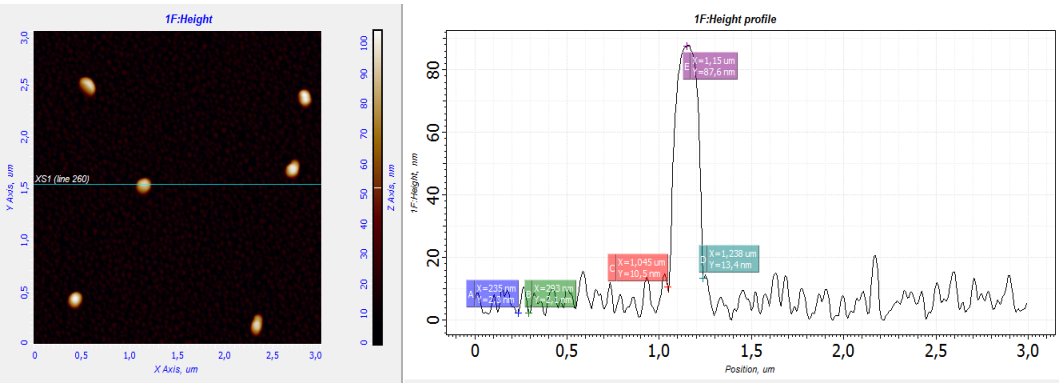

Line profile	X, width (µm)	Y, height(nm)
A	**0.235**	**2.3**
B	**0.293**	**2.1**
C	**1,05**	**10.5**
D	**1,24**	**13.4**
E	**1,15**	**87.6**

Figure A.11 Application of a line profile to measure the characteristic dimensions of surface features. From the accumulated plot on right site, height and width features of materials are measured. The exact dimensions of features are presented.

Particle and grain analysis are two common types of automated segmentation routines for statistical counting of characteristics of materials. Particle analysis is usually used for measuring isolated particles placed on a well flat substrate. This process is carried out by using threshold analysis command in which the user fix a value above of which all features are characterized as particles. The number of features as well as their width, length, height, volume and more are displayed on table for further statistical analysis. Grain analysis command is used for measuring characteristics from granular materials for which their grains have almost the same height and are separated by grain boundary defects. More information about segmentation analysis can be found from cited references [206–208].

A significant parameter that is used to characterize surface features is roughness [209]. There are various statistical formulas that can be used to measure the roughness of a material. The most common are: R_a (arithmetic roughness) and R_{rms} (root mean squared

roughness). For R_a and R_{rms} values, the higher the roughness value the greater the variation of heights on the surface of material.

APPENDIX A **Dissemination of results**

The results of this thesis have been presented in a range of conferences. Furthermore, many parts of this thesis have been published, or are under consideration for publication, in a series of peer reviewed scientific journals a summary of which is presented below.

B 1 Published/submitted scientific work

1. **M. Constantinou**, M. Pervolaraki, L. Koutsokeras, C. Prouskas, P. Patsalas, P. C. Kelires, J. Giapintzakis, G. Constantinides 'Enhancing the nanoscratch resistance of pulsed laser deposited DLC films through molybdenum-doping' Surface and Coatings Technology, 330, 185-195, 2017.
2. **M. Constantinou**, M. Pervolaraki, P. Nikolaou, C. Prouskas, P. Patsalas, P. C. Kelires, J. Giapintzakis, G. Constantinides 'Microstructure and nanomechanical properties of pulsed excimer laser deposited DLC:Ag films: enhanced nanotribological response' Surface and Coatings Technology, 309, 320-330, 2017.
3. M. Rikkou-Kalourkoti, E. N. Kitiri, E. Leontidis, C. S. Patrickios, **M. Constantinou**, G. Constantinides, X. Zhang, C. M. Papadakis and J. P. Gong, 'Double-networks based on amphiphilic cross-linked star block copolymer first co-networks and randomly cross-linked hydrophilic second networks', Macromolecules, 49(5), 1731-1742, 2016.
4. E. Xenofontos, A. Feidiou, **M. Constantinou**, G. Constantinides, I. Vyrides, 'Copper biomachining mechanisms using the newly isolated Acidithiobacillus ferrooxidans strain B1', Corrosion Science, 100, 642-650, 2015.
5. P. Nikolaou, C. Mina, **M. Constantinou**, L.E. Koutsokeras, G. Constantinides, E. Lidorikis, A. Avgeropoulos, P.C. Kelires, and P. Patsalas, 'Functionally-graded PDMS/Ag nanocomposites with tailored broadband optical absorption' Thin Solid Films, 581, 14-19, 2015.
6. **M. Constantinou**, P. Nikolaou, L. E.Koutsokeras, A. Avgeropoulos, D. Moschovas, C. Varotsis, P. Patsalas, P. Kelires, G. Constantinides, Metal (Ag/Ti)-Containing Hydrogenated Amorphous Carbon Nanocomposite Films with Enhanced

Nanoscratch Resistance: Hybrid PECVD/PVD System and Microstructural Characteristics, Nanomaterials, 8(4) 209, 2018.

7. Konstantinos Kapnisis, **Marios Constantinou**, Maria Kyrkou, Petros Nikolaou, Andreas Anayiotos, Georgios Constantinides, Nanotribological response of a-C:H coated metallic biomaterials: the cases of stainless steel, titanium, and niobium, Journal of Applied Biomaterials and Functional Materials, 2018, (accepted).
8. G. N. Haidemenopoulos, **M. Constantinou**, H. Kamoutsi, D. Krizan, I. Bellas, L. Koutsokeras, G. Constantinides, Probing the Evolution of Retained Austenite in TRIP Steel During Strain-Induced Transformation: a Multi-Technique Investigation, submitted to Journal of the Minerals, Metals and Materials Society, 2018, (accepted).

B 2 Participation in national and international conferences

1. **M. Constantinou**, M. Pervolaraki, L Koutsokeras, C. Prouskas, P.C. Kelires, P. Patsalas, J. Giapintzakis, G. Constantinides, 'Nano-mechanical characteristics of pulsed laser deposited diamond-like carbon molybdenum alloy systems', Advanced nanomechanical techniques for academic and industrial research, 13-14 December 2017, The University of Warwick, UK. (podium – **invited talk**)
2. Konstantinos Kapnisis, **Marios Constantinou**, Maria Kyrkou, Petros Nikolaou, Andreas Anayiotos and Georgios Constantinides. Tribomechanics of Bare and a-C:H Coated Metallic Biomaterials. Summer Biomechanics, Bioengineering and Biotransport Conference, 21-24 June 2017, Tucson, AZ, USA. (podium)
3. K. Kapnisis, **M. Constantinou**, M. Kyrkou, P. Nikolaou, A. Anayiotos, G. Constantinides, Tribomechanical response of bare and hydrogenated amorphous carbon coated metallic biomaterials, 10th International conference on materials science and engineering, Brasov, Romania, 9-11 March 2017. (podium)
4. **M. Constantinou**, M. Pervolaraki, P. Nikolaou, C. Prouskas, P.C. Kelires, P. Patsalas, J. Giapintzakis, G. Constantinides, 'Nanomechanical characteristics of pulsed-laser deposited DLC films with metallic (Ag, Mo) nanoinclusions', XXXII Panhellenic Conference on Solid State Physics and Materials Science, Ioannina, Greece, 18-21 September 2016. (podium) **Best Oral Presentation award.**
5. P. Nikolaou, **M. Constantinou**, D. Bellas, P. Patsalas, P. Kelires, E. Lidorikis, G. Constantinides, 'Hydrogenated amorphous carbon with embedded plasmonic NPs of

silver/gold: nanocomposite films for selective and broadband optical absorption', XXXII Panhellenic Conference on Solid State Physics and Materials Science, Ioannina, Greece, 18-21 September 2016. (podium)

6. **M. Constantinou**, P. Nikolaou, P.C. Kelires, P. Patsalas, G. Constantinides, 'PECVD/PVD hybrid deposition technology for developing Ag- and Ti-reinforced hydrogenated amorphous carbon nanocomposite coatings' XXXII Panhellenic Conference on Solid State Physics and Materials Science, Ioannina, Greece, 18-21 September 2016. (poster)
7. **M. Constantinou**, M. Pervolaraki, L. Koutsokeras, P. C. Kelires, P. Patsalas, J. Giapintzakis, G. Constantinides, Nanomechanical and nanotribological response of amorphous carbon-silver nanocomposite films, E-MRS, Lille, France, 2-6 May 2016. (podium)
8. S. Pozov, P. Nikolaou, **M. Constantinou**, G. Constantinides, Surface pattering of PDMS through argon ion bombardment and/or amorphous carbon deposition, E-MRS, Lille, France, 2-6 May 2016. (poster)
9. P. Nikolaou, R. Soteriou, **M. Constantinou**, P. Kelires, G. Constantinides, P. Patsalas, Direct deposition and in-situ nitridation of Ti and Zr nanoparticles, E-MRS, Lille, France, 2-6 May 2016. (poster)
10. P. Nikolaou, **M. Constantinou**, K. Pikkou, P. Patsalas, P. Kelires, G. Constantinides, Hydrogenated amorphous carbon-silver/gold nanocomposite films for solar harvesting applications, E-MRS, Lille, France, 2-6 May 2016. (podium)
11. **M. Constantinou**, M. Pervolaraki, L. Koutsokeras, P.C. Kelires, P. Patsalas, J. Giapintzakis, G. Constantinides, 'Amorphous carbon films for protective coatings and solid lubricant applications', XXXI Panhellenic Conference on Solid State Physics and Materials Science,Thessaloniki, Greece, 20-23 September 2015. (podium)
12. G.N. Haidemenopoulos, I. Bellas, H. Kamoutsi, D. Krizan, **M. Constantinou**, G. Constantinides, 'Magnetic force microscopy: probing the strain-induced microstructural evolution in TRIP steel', Workshop on Magnetic Materials, University of Cyprus, Nicosia, Cyprus, 18 June 2015. (talk)
13. **M. Constantinou**, G. Constantinides, DLC coatings for biomedical applications, Training school COST Action NAMABIO MP1005, 14-17 October, Frederick University, Nicosia, Cyprus.

14. **M. Constantinou**, M. Pervolaraki, L. Koutsokeras, P. Kelires, I. Giapintzakis, G. Constantinides, ‘Nanomechanical Response of Amorphous Carbon Films: Effect of Thermal Processing’, XXIX Panhellenic Conference on Solid State Physics and Materials Science, Athens, Greece, 22-25 September 2013. (talk)
15. P. Nikolaou, **M. Constantinou**, G. Constantinides, P. Patsalas, L. Koutsokeras, ‘Optical and Mechanical Properties of Silicone-based Nanocomposites’, XXIX Panhellenic Conference on Solid State Physics and Materials Science, Athens, Greece, 22-25 September 2013. (poster)
16. M. Karyou, D. Photiou, **M. Constantinou**, L. Koutsokeras, G. Constantinides, ‘Mechanics of Biological Nanocomposites: The Case of Nacre in Mediterranean Shells’, XXIX Panhellenic Conference on Solid State Physics and Materials Science, Athens, Greece, 22-25 September 2013. (poster)
17. M. Pervolaraki, L. Koutsokeras, G. I. Athanasopoulos, F. Kossivas, **M. Constantinou**, G. Constantinides, A. Kyprianou, M. Gioti, S. Logothetidis, J. Kioseoglou, Ph. Komninou, P. Patsalas, and J. Giapintzakis, ‘Silver Nanoinclusions in Diamond-Like Carbon Coatings for Solar Thermal Energy Applications’, XIV International Conference on Intergranular and Interphase Boundaries in Materials, Halkidiki, Greece, 23-28 June 2013. (talk)
18. Pervolaraki M., Koutsokeras L., Athanasopoulos G.I., Kossivas F., **Constantinou M.**, Constantinides G., Kyprianou A., Gioti M., S. Logothetidis, Kioseoglou J., Komninou Ph., Patsalas P., Giapintzakis J., 'Diamond-Like Carbon Silver Nanocomposite Films for Solar Harvesting Applications', E-MRS Spring Meeting, Strasbourg, France, 27-31 May 2013. (talk)
19. Photiou D., Panagiotopoulos N.T., **Constantinou M.**, Evangelakis G.A., Constantinides G., ‘Nanomechanics of binary and ternary Ti-Nb-Hf films for biomedical applications’, 12th MML European Nanomechanical User Group Meeting, University of Malta, Malta, 24-25 October, 2012. (poster)
20. Photiou D., Panagiotopoulos N.T., **Constantinou M.**, Evangelakis G.A., Constantinides G., ‘Nanomechanics of binary and ternary Ti-Nb-Hf films for biomedical applications’, 9thInternational Conference on Nanosciences and Nanotechnologies – NN12, Thessaloniki, Greece, 3-6 July, 2012. (poster)